SYNTHESIS AND CHARACTERISATION OF THE GEOMETRIC FERROELECTRIC LATAO4

Grant William Howieson

A Thesis Submitted for the Degree of PhD
at the
University of St Andrews

2022

Identifiers to use to cite or link to this thesis:

DOI: https://doi.org/10.17630/sta/369
http://hdl.handle.net/10023/27273

Synthesis and Characterisation of the Geometric Ferroelectric $LaTaO_4$

Grant William Howieson

University of
St Andrews

This thesis is submitted in partial fulfilment for the degree of
Doctor of Philosophy (PhD)
at the University of St Andrews

January 2022

Candidate's declaration

I, Grant William Howieson, do hereby certify that this thesis, submitted for the degree of PhD, which is approximately 40,000 words in length, has been written by me, and that it is the record of work carried out by me, or principally by myself in collaboration with others as acknowledged, and that it has not been submitted in any previous application for any degree.

I was admitted as a research student at the University of St Andrews in August 2017.

I received funding from an organisation or institution and have acknowledged the funder(s) in the full text of my thesis.

Date 10/01/2022 Signature of candidate

Supervisor's declaration

I hereby certify that the candidate has fulfilled the conditions of the Resolution and Regulations appropriate for the degree of PhD in the University of St Andrews and that the candidate is qualified to submit this thesis in application for that degree. I confirm that any appendices included in the thesis contain only material permitted by the 'Assessment of Postgraduate Research Students' policy.

Date 10/01/2022 Signature of supervisor

Permission for publication

In submitting this thesis to the University of St Andrews we understand that we are giving permission for it to be made available for use in accordance with the regulations of the University Library for the time being in force, subject to any copyright vested in the work not being affected thereby. We also understand, unless exempt by an award of an embargo as requested below, that the title and the abstract will be published, and that a copy of the work may be made and supplied to any bona fide library or research worker, that this thesis will be electronically accessible for personal or research use and that the library has the right to migrate this thesis into new electronic forms as required to ensure continued access to the thesis.

I, Grant William Howieson, have obtained, or am in the process of obtaining, third-party copyright permissions that are required or have requested the appropriate embargo below.

The following is an agreed request by candidate and supervisor regarding the publication of this thesis:

Printed copy

Embargo on all of print copy for a period of 1 year on the following ground(s):

- Publication would preclude future publication

Supporting statement for printed embargo request

There is a paper that is expected to be produced from the work within this thesis and publication of the thesis would preclude the publication of this paper.

Electronic copy

Embargo on all of electronic copy for a period of 1 year on the following ground(s):

- Publication would preclude future publication

Supporting statement for electronic embargo request

There is a further article expected to be produced from the work within this thesis and publication of the thesis would preclude this.

Title and Abstract

- I require an embargo on the abstract only.

Date 10/01/2022 Signature of candidate

Date 10/01/2022 Signature of supervisor

Underpinning Research Data or Digital Outputs

Candidate's declaration

I, Grant William Howieson, understand that by declaring that I have original research data or digital outputs, I should make every effort in meeting the University's and research funders' requirements on the deposit and sharing of research data or research digital outputs.

Date 10/01/2022 Signature of candidate

Permission for publication of underpinning research data or digital outputs

We understand that for any original research data or digital outputs which are deposited, we are giving permission for them to be made available for use in accordance with the requirements of the University and research funders, for the time being in force.

We also understand that the title and the description will be published, and that the underpinning research data or digital outputs will be electronically accessible for use in accordance with the license specified at the point of deposit, unless exempt by award of an embargo as requested below.

The following is an agreed request by candidate and supervisor regarding the publication of underpinning research data or digital outputs:

Embargo on all of electronic files for a period of 1 year on the following ground(s):

- Publication would preclude future publication

Supporting statement for embargo request

Some data presented in this thesis is yet to be published.

Date 10/01/2022 Signature of candidate

Date 10/01/2022 Signature of supervisor

Abstract

$LaTaO_4$ is one of very few reported $n = 2$ Carpy-Galy oxides. It is isostructural to the $BaMF_4$ fluorides which were subject of much prior study due to their ferroelectric and multiferroic properties. Previous studies of $LaTaO_4$ have been consistent in their conclusion that it can adopt either a low temperature non-polar monoclinic, or high temperature polar orthorhombic phase, with the monoclinic – orthorhombic transition temperature ($T_{m\text{-}o}$) being dependent on the preparation method. Recent studies, however, have reported an unidentified dielectric anomaly in the orthorhombic phase which alludes to an additional subtle structural transition above $T_{m\text{-}o}$.

Powder neutron (PND) and electron diffraction studies have revealed that the previously unidentified dielectric anomaly denotes a transition between an incommensurately modulated and unmodulated orthorhombic ($Cmc2_1$) structure at ~503 K. The phase transition sequence is re-investigated in light of this new modulated phase, with resonant ultrasound (RUS) and Raman spectroscopy being utilised to elucidate the dynamics of transition and show the incommensurate – commensurate transition to be unusually 1st order, but nearly continuous (tri-critical).

Refinement of PND data in the $Cmc2_1(\alpha 00)0s0$ superspace group, indicates a modulation wavevector $q = (0.456\ 0\ 0)$ at 483 K. The modulation arises from a variation in La^{3+} positions and octahedral tilts which propagate along the polar *a*-axis and is speculated to arise as a mechanism to improve overall bonding environment of La^{3+}. Electron microscopy reveals that the modulation arises from partially ordered sub-units, which are 2.5× and 3× expansions of the original orthorhombic cell. A model has been constructed which combines the local structural origin with the observed macroscopic modulation, where sub-units partially order with an average periodicity of ~11*a* (~0.456 *a**).

Previous studies report a relationship between the stability of each phase of $LaTaO_4$ and A-cation size. To explore the possibility that the modulation arises purely by an A-cation size effect, the series $La_{1-x}Ln_xTaO_4$ is synthesized, where Ln = Ce^{3+}, Pr^{3+} and Nd^{3+} ($0 \leq x \leq 0.3$). Doping with these isovalent cations shows a general trend of stabilisation of the low temperature phases with decreasing average A-cation radii; the effect is amplified in Ce^{3+}-doped samples and preliminary analysis suggests that this is due to a mix of oxidation states and the associated inter- and de-intercalation of interstitial oxygens during thermal cycling.

Acknowledgements

I would like to thank my supervisor Dr. Finlay Morrison for his help, support, and advice throughout the duration of my PhD – as well as his seemingly inexhaustible patience. I would also like to express my thanks to the late Professor James F. Scott FRS, who offered an incredible insight into the world of ferroelectrics and filled the lab with stories, anecdotes and discussions, some of which even involved research.

The Morrison group has always been an inviting work environment and I would like to express my gratitude to Jonathan, Jason, Rebecca and Jiyu for welcoming me into the group, getting me started and continuing to provide valuable advice on my research. Those members who joined the group during my studies, Kerry and Hang, I would like to thank them for the fantastic company they provided and wish them the very best in completing the remainder of their PhD.

I would like to thank those who have helped with various parts of this work: Prof. Wuzong Zhou and Dr. Shitao Wu, for the collection and analysis of electron microscopy data; Dr. Alexandra Gibbs for her guidance in the collection of neutron diffraction data and the additional data which she kindly agreed to collect – without it, this work, and subsequent publications, would not be possible; Prof. Michael Carpenter for the collection and analysis of RUS data, as well as his expert input on strain analysis and Landau theory; Dr. Karuna Mishra and Prof. Ram Katiyar, for the collection and analysis of Raman spectroscopy data; and to Federico Grillo for the painstaking collection and analysis of XPS data.

Finally, I would like to thank all of the members of the Chemistry community in St Andrews who I became good friends with over the last 4 years, who are too numerous to list. The pubs in St Andrews will certainly miss us.

Funding

This work was supported by the Engineering and Physical Sciences Research Council doctoral training programme and grant No. EP/P024637/1, and the School of Chemistry at the University of St Andrews.

Research data underpinning this thesis are available at:
https://doi.org/10.17630/a7540ced-d4a3-4c89-a93f-6e21dc2b4c01

Published Papers

Material from this thesis has previously been published:

Howieson, G. W. *et al.* Incommensurate-Commensurate Transition in the Geometric Ferroelectric $LaTaO_4$. *Adv. Funct. Mater.* 2004667 (2020).

Howieson, G. W. et al. Structural Phase Transitions in the Geometric Ferroelectric $LaTaO_4$. Phys. Rev. B 103, 1–12 (2021).

Table of Contents

Chapter 1: Introduction

1.1 Functional Materials

Functional materials are, as the name suggests, materials which exhibit some physical phenomena which can be utilised to fill some active role in device applications. These materials exhibit physical phenomena which can be applied to many technological applications - whether that be semiconductors which brought about massive advances in computing, magnetic materials which have been widely used for decades as memory storage devices, or polar dielectrics which are a staple of capacitor and sensor technology. Each of these applications rely on the tailored electronic properties of carefully designed materials and as we progress further into the silicon age our need for better-performing, more efficient, cheaper, and cleaner functional materials will continue to grow.

1.2 Dielectrics

In general, dielectrics are materials which exhibit a high level of electrical insulation, and an electrical polarisation of the material can be induced by the application of an external field. The overall macroscopic polarisation of the material is given by:

$$p = \alpha E \qquad 1.1$$

Where the dipole moment (p) is a function of the overall polarisability of the material (α) and the applied electric field (E). However, at the microscopic level there are different mechanisms which contribute to the overall macroscopic polarisability (α). These mechanisms and their time dependency are shown in **figures 1.1 and 1.2**, respectively.

Each of these polarisation mechanisms contribute to the overall polarisability (α) of a material in a summative way. Electronic polarisation (α_e) occurs due to the asymmetric charge distribution of the electron cloud around an atomic nucleus which is induced by the application of an electric field. Ionic polarisation (α_i) is induced in a similar way, where an ionic material experiences a shift of ions away from their barycentre of charge to form an induced dipole. Dipolar polarisation (α_d) arises when permanent dipoles are present in the structure, and these are naturally disordered – application of an external electric field causes some increased degree of alignment of these dipoles with the field. The final mechanism, space charge polarisation (α_s) is a consequence of the relatively long-range transport of mobile charge carriers being impeded by some barrier present in a material. In dielectric ceramics (such as that shown in **figure 1.1**) this impedance may be due to grain boundaries and as such ceramic microstructure greatly affects the space charge contribution to the overall polarisability. Each of these mechanisms have frequency (time) dependency (**figure 1.2**) and the dielectric spectroscopy in this thesis is within the range of 25 Hz to 2MHz, which allows any space charge and dipole contributions to be measured in addition to the ionic ones.

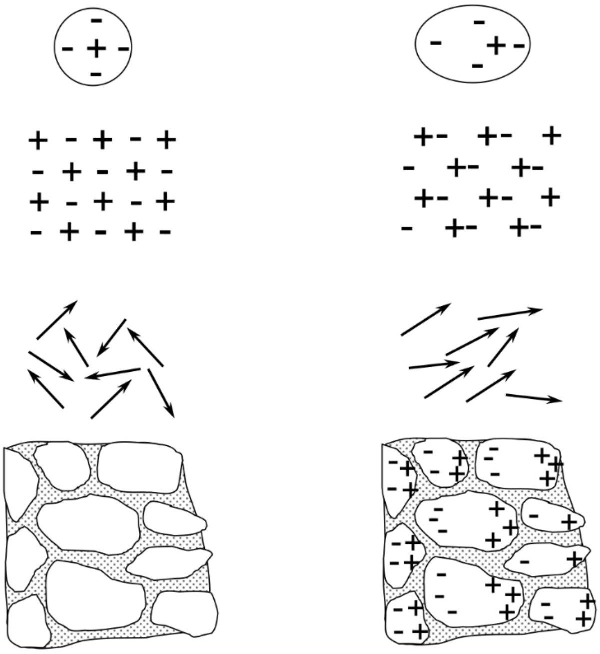

Figure 1.1: Illustrations of the electrical mechanisms which give rise to dipole moments in dielectric materials (after Ref [1]).

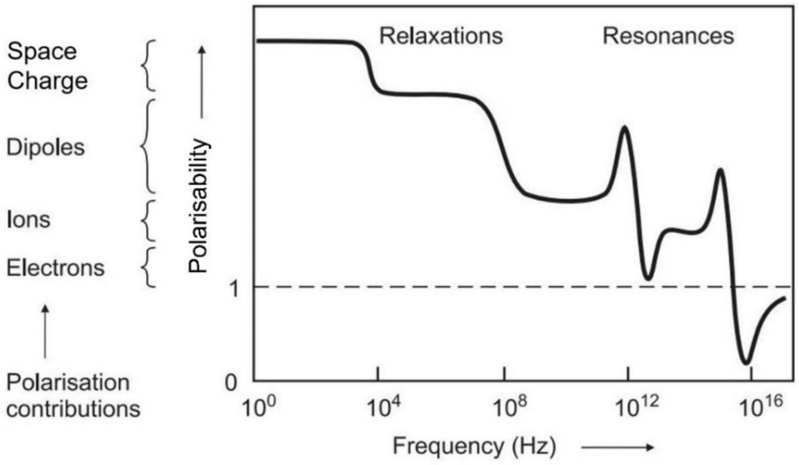

Figure 1.2: Diagram of the time dependency of each mechanism which contributes to the overall polarisation.

The most common use for dielectric materials is in capacitors, electrical energy is stored by the separation of charge - this is an ideal application for materials with notably high total polarisability. The most basic form of capacitor is a parallel plate capacitor, where metal plates of area, *A*, are separated in a vacuum by distance, *d*; when a field is applied between the plates, a charge (*Q*) forms on each plate with polarity relative to the field direction (**figure 1.3**). This yields:

$$Q = C_0 V \qquad 1.2$$

where C_0 is the vacuum capacitance, *Q* is charge and *V* is the voltage.

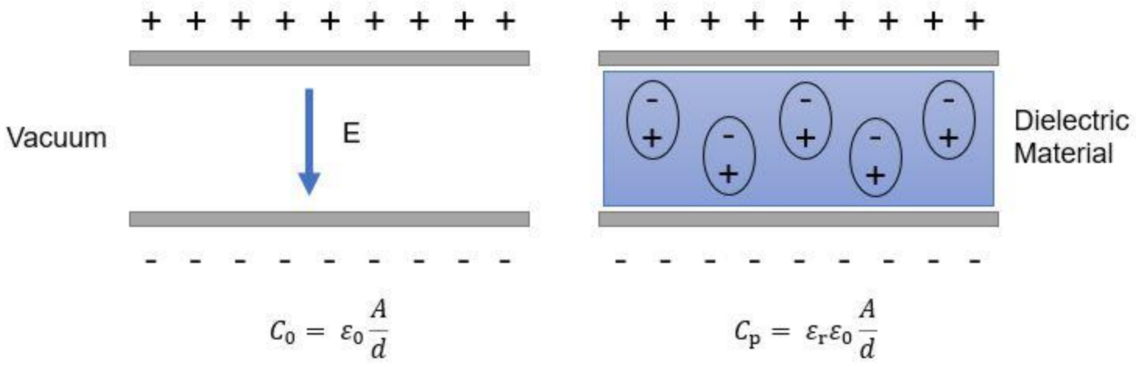

Figure 1.3: Diagrams and associated equations for parallel plate capacitors; one with a vacuum between each plate and one with a dielectric material.

The field applied (*E*), is given by:

$$E = \frac{V}{d} \qquad 1.3$$

where the field (*E*) is shown to be a function of the voltage applied to the plates (*V*) and the distance they are separated by (*d*).

The relationship between the charge density (*σ*, *i.e.,* charge per unit area) which accumulates on the plates and the applied field (*E*) is given by:

$$\sigma = \varepsilon E \qquad 1.4$$

ε represents a value which is called permittivity, which essentially describes the polarisability of the medium between the plates. In the case of the simple parallel plates separated by a vacuum this value is defined as ε_0, the permittivity of free space, and is a fundamental physical constant with value 8.854×10^{-14} F cm^{-1}. The charge density, *σ*, can also simply be expressed as the total charge, *Q*, divided by the electrode area, *A*:

$$\sigma = \frac{Q}{A} \qquad 1.5$$

where *Q* is the charge on the plates and *A* is the electrode (plate) area.

Equations 1.3, 1.4 and 1.5 can now be substituted into equation 1.2 to better calculate the capacitance of the 'empty' parallel plate capacitor (ε becomes ε_0 in this case):

$$C_0 = \frac{A\sigma}{Ed} = \varepsilon_0 \frac{A}{d} \qquad 1.6$$

This relates the capacitance of our 'empty' parallel plates to their geometry and the permittivity of free space, ε_0. However, the capacitance can be changed by the insertion of a dielectric medium between the plates, where the effect on the capacitance is given in terms of the relative permittivity:

$$C_p = \varepsilon_r \varepsilon_0 \frac{A}{d} \qquad 1.7$$

C_p denotes the new capacitance, and which is a direct result of additional polarisability (permittivity) of the material between the plates. The relative permittivity (ε_r) is, unsurprisingly, a ratio of the capacitance of a dielectric medium (C_p) to that of a vacuum (C_0):

$$\varepsilon_r = \frac{C_p}{C_0} = 1 + \chi_e \qquad 1.8$$

X_e is electric susceptibility; it is a dimensionless constant which is intrinsic to a material and is a measure of how readily a dielectric will polarise under an applied field. The relative permittivity of a material, ε_r, is also known as the dielectric constant (*k*).

The relative permittivity, ε_r, assumes an ideal case where no energy is lost when charge is displaced under an applied electric field, but in reality, there is some loss due to internal mechanisms such as inertia and friction. These can both be accounted for by the complex permittivity, ε*, which includes both the relative permittivity and the energy dissipation:

$$\varepsilon^* = \varepsilon' - i\varepsilon'' \qquad 1.9$$

where $i = \sqrt{-1}$. For good electrical insulators, the real part of the complex equation (ε’) is effectively the relative permittivity of the material and can be considered a measure of the energy which is stored in the material per cycle of applied alternating electric field. The energy lost per cycle is represented by the imaginary part (ε’’). This can be visualised by the plot in **figure 1.4**.

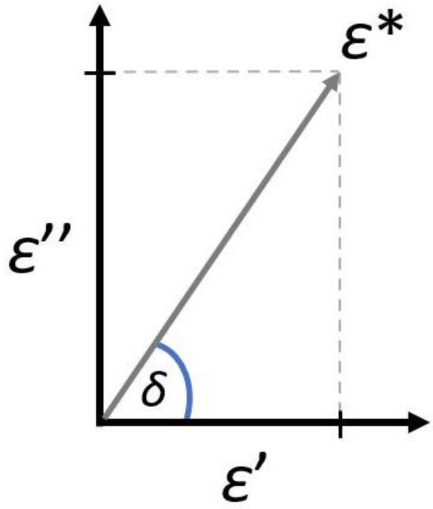

Figure 1.4: Complex permittivity and tan δ. The real part of the complex plane denotes the relative permittivity and represents the energy stored in the material. The imaginary part is the energy lost per cycle.

The real and imaginary parts of the complex plane form an angle, δ. The tangent of this angle yields the ratio of the absolute dielectric loss and relative permittivity:

$$\tan\delta = \frac{\varepsilon''}{\varepsilon'} \qquad 1.10$$

Observation of the dielectric properties of a material can be an incredibly valuable tool in its characterisation. As the polarisability of a material is intrinsically linked to its composition and structure, dielectric spectroscopy can be used to monitor structural changes in a sample as a function of temperature – changes in atomic configuration may enhance or reduce the polarisability and hence the observed relative permittivity (and dielectric loss).[1]

1.3 Polar dielectrics

The materials to be discussed in this thesis all pertain to the class of materials which are classed as polar dielectrics, with their functionality being a consequence their chemical composition and crystal structure. The dielectric properties outlined here are common throughout the other classes of materials discussed in this chapter and their inter-relationship can represented by **figure 1.5,** where it is shown that the properties of the parent class of materials is also found in that of each subsequent sub-class.

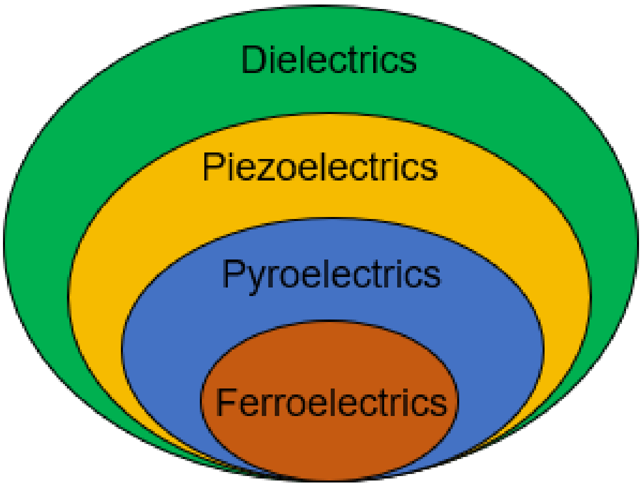

Figure 1.5: Venn diagram of dielectric material hierarchy. Polar dielectric properties are common in all materials encompassed by this diagram. More generally, the phenomena exhibited by each class of material is also found in each subsequent sub-class.

1.4 Piezoelectrics

Piezoelectrics are an incredibly useful type of functional material which can generate an electric charge through the application of an applied stress by the direct piezoelectric effect. This phenomenon arises as a result of ionic displacement within the crystal structure and as such any non-centrosymmetric space groups may exhibit this property. As a further subset of this, all polar space groups except point group 432 can exhibit piezoelectricity (20 out of the 32 crystal classes).

The linear coupling of stress and charge makes these materials useful as sensors and actuators. The relationship between applied stress and the resulting charge generated can be expressed by:

$$d = \frac{D}{\sigma} \qquad 1.11$$

where d is the piezoelectric constant (coulombs/Newton), D is the charge density and σ is the is the applied stress. This describes the ‘direct’ piezoelectric effect but there exists a ‘converse’ piezoelectric effect, where the application of an external field generates a strain of the crystal, S. This is expressed by:

$$S = dE \qquad 1.12$$

where E is the applied field and d is expressed in meters/Volts.

1.5 Pyroelectrics

Of the 20 polar crystal classes which show piezoelectricity, half of these may maintain a dipole moment in an unstrained state. This means these materials are different from the previous types of dielectrics, in that they do not require external stimuli to induce a polarisation and as such these materials are said to have a ‘spontaneous’ polarisation.

One consequence of this structural property is pyroelectricity, where uniformly heating the crystal will change the magnitude of the dipole moment, causing an observable change in the polarisation. The change in polarisation as a function of temperature is given by:

$$\Delta P = \pi \Delta T \qquad 1.14$$

where ΔP is the change in polarization, ΔT is the change in temperature and π is the pyroelectric coefficient – the sign of this coefficient is given in respect to the piezoelectric axis and the units are C m^{-2} K^{-1}.[2] It is noted that any piezoelectric crystal may develop a charge when non-uniformly heated due to stresses induced by thermal expansion.[3]

1.6 Ferroelectrics

A ferroelectric crystal exhibits a spontaneous polarisation which may be reversed by the application of an external field – the nomenclature for such materials being borrowed from their magnetic counterparts. As this requires a permanent spontaneous dipole to be present, this may only occur in a subset of pyroelectric materials. The most iconic feature of a ferroelectric material is the hysteresis loop that is observed when measuring polarisation as a function of an applied electric field (**figure 1.6**).

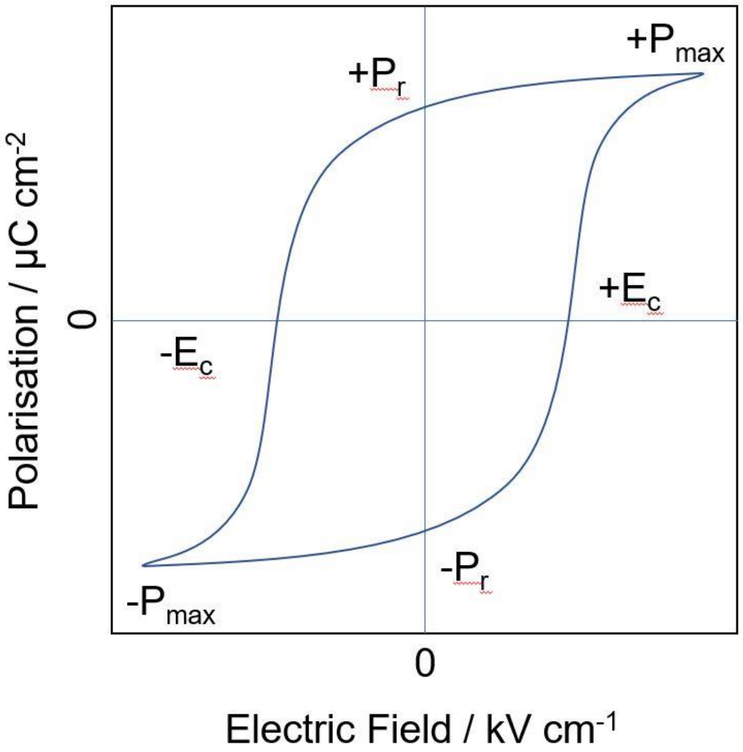

Figure 1.6: Example of a ferroelectric hysteresis loop produced from polarisation vs. field measurements.

Figure 1.6 shows that for a ferroelectric which has a spontaneous polarisation aligned in a certain direction, increasing the electric field above the coercive field ($\pm E_c$) in the opposing direction, will induce a spontaneous polarisation that aligns with this field, hence switching the polarity. On removal of the electric field the newly oriented polarity will be retained and assume a value known as the remnant polarisation ($\pm P_r$). This process is completely reversible and applying an opposing field will switch the direction of the polarisation as long as the field is large enough to overcome the energy barrier between the two configurations. A ferroelectric material will have two equally low energy structural configurations which produce a spontaneous dipole moment along opposing directions in the polar axis (positive or negative polarisation) – these two low energy configurations must also have a suitably small barrier separating them to allow ferroelectric switching to occur.

Materials which are ferroelectric in one state may not always retain this property as they undergo polymorphic phase transitions. This is another case where ferroelectrics borrow nomenclature from ferromagnetism, as the temperature at which the material undergoes a transition to a paraelectric state is known as the Curie temperature (T_C). For example: on heating, tetragonal perovskites such as $PbTiO_3$ will undergo a transition to a cubic structure at T_C, which is inherently non-polar. The spontaneous polarisation (P_s) of the material therefore disappears on heating to T_C (**figure 1.7**).

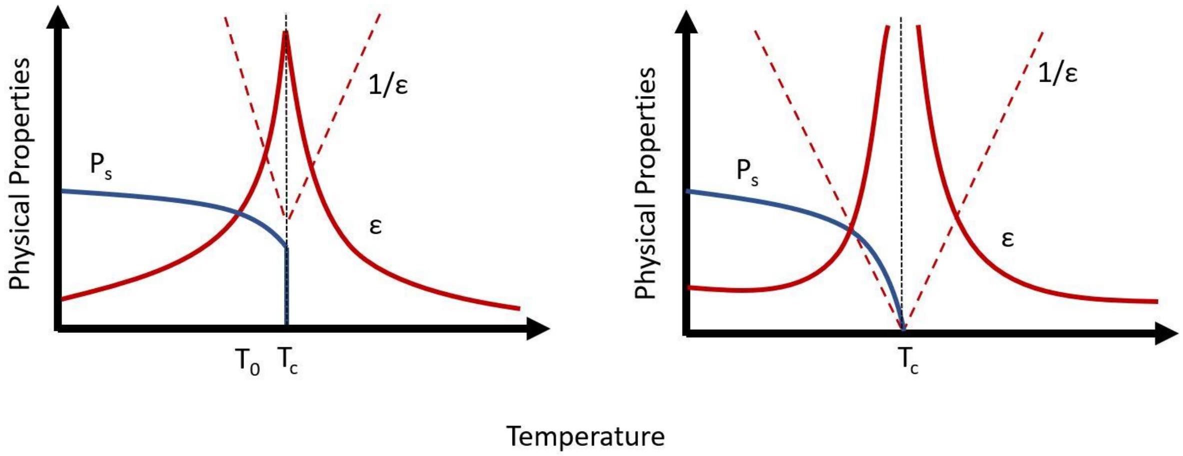

Figure 1.7: Behaviour of polarisation (Ps), permittivity (ε) and inverse permittivity (1/ε) as a function of temperature for a 1st order phase transition (left) and a 2nd order phase transition (right).

As shown in **figure 1.7,** the permittivity is also affected as a phase transition is approached. Most materials show very little variation in their permittivity as a function of temperature but with ferroelectric materials, thermal disruption of oscillations associated with dipole formation and their interaction causes a change their polarisability, leading to a very large increase in permittivity at the transition. Above the transition, the permittivity obeys the Curie-Weiss relationship:

$$\varepsilon = \frac{\theta}{T-T_0} \qquad 1.15$$

where θ is the Curie constant. A plotting of reciprocal permittivity as a function of T therefore gives a straight line (as in **figure 1.7**), with gradient $1/\theta$ and with the x-axis intercept T_0. In the case of a 1^{st} order transition $T_C < T_0$ and for a 2^{nd} order transition, $T_0 = T_C$.

1.7 Mechanisms of Ferroelectricity

As materials transition from their paraelectric phase to the ferroelectric phase, the spontaneous polarisation can arise in many ways. The structural mechanisms which are observed at the ferroelectric transition allow these materials to be divided into many different classes. One distinction that can be made is between displacive and order-disorder ferroelectric transitions. Displacive transitions occur when dipoles are generated as the structure enters the ferroelectric phase – the separation of the positive and negative barycentre's create an overall spontaneous polarisation. Order-disorder transitions on the other hand, occur in structures where dipoles exist in the paraelectric phase, and these dipoles are randomly oriented resulting in zero net polarisation. In the ferroelectric phase, however, these dipoles will cooperatively align to give rise to a spontaneous polarisation.

The means of structural rearrangement which occurs at ferroelectric transitions can be characterised to yield further sub-classes of ferroelectric transitions. The specific distortions which occur during these polymorphic phase transitions can be described by the symmetry modes of the irreducible representation of the undistorted structure. The distortion modes are represented by Miller-Love notation which describes the irreducible representation as well as the propagation wavevectors in terms of the 1st Brillouin zone. With respect to these structural distortions, transitions can be divided into two further classes: proper and improper.

1.8 Proper Ferroelectrics

A proper ferroelectric transition is one which has a simple, zone-centre distortion mode (Γ-mode), which does not generate any expansion of the original paraelectric unit cell, *i.e.* both the paraelectric and ferroelectric unit cells contain the same number of formula units. A classic example of a proper ferroelectric is $BaTiO_3$, a material which assumes the typical perovskite structure. The perovskites and related materials have been well studied on account of their incredibly compositional diversity – this is especially true in the context of ferroelectrics. The cubic structure above T_C is centrosymmetric and inherently non-polar but undergoes a transition to the ferroelectric tetragonal phase at T_C = ~130 °C. A spontaneous polarisation arises through displacement of the Ti^{4+} cation to one of two energetically favourable positions, and can be considered as a 1st order displacive proper ferroelectric (similar to what is shown in **figure 1.8**).

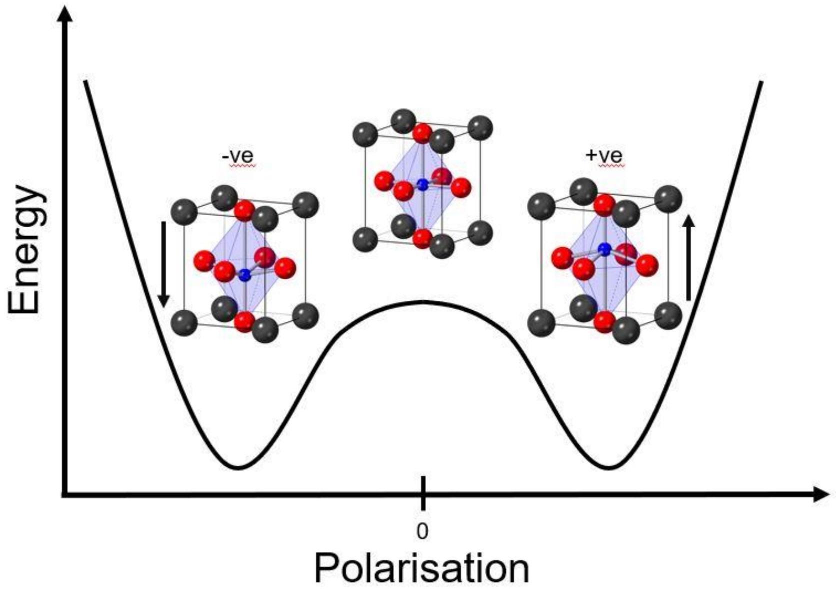

Figure 1.8: An energy vs. polarisation plot which shows a 'double potential well' where two low-energy states are shown at either side of a small energy barrier. This demonstrates the energetically favourable polarised configurations of a tetragonal perovskite (ABO_3), with A and B cations being shown as black and blue spheres respectively. Red spheres denote the oxygen anions which form an octahedra around the B-site.

The mechanism shown in this diagram is the simplest example of ferroelectricity by a displacive transition – the cation shifts from the barycentre of the structure to produce a dipole moment. The cation within the centre of the octahedra may shift towards an edge, face or vertex in the octahedron, and this distortion is attributed to the second order Jahn-Teller effect.[4] This is a zone-centre distortion of the parent cubic structure and as such retains the same number of formula units in its ferroelectric phase.

1.9 Improper Ferroelectrics

The proper ferroelectric transition outlined above occurs by a zone-centred structural distortion which is the primary driving force of the spontaneous polarisation. However, improper ferroelectric transitions occur by zone-boundary distortion modes, meaning that there is an expansion of the original parent cell, and more formula units are observed in the ferroelectric unit cell. Moreover, it is found that the generation of a spontaneous polarisation is not the main driving force of the transition. Improper ferroelectrics are materials whose polarization is induced as a side effect of non-polar distortion modes (usually driven by geometric effects)[5], and these can be sub-categorized into two forms: geometric (GIFs) and hybrid (HIFs) improper ferroelectrics.

GIFs are materials whose spontaneous polarisation occurs as a consequence of electrostatic and size effects (ionic size) rather than the traditional changes in chemical bonding (SOJT) which occur at the ferroelectric phase transition. This type of transition was initially theorised to occur in $YMnO_3$ by Van Aken *et al.*[6] and demonstrated experimentally by Gibbs *et al.* using high resolution powder neutron diffraction.[7] It was shown that the displacements which occur between the paraelectric $P6_3/mmc$ phase and the ferroelectric $P6_3$ phase are primarily driven by a cell-tripling K_3 mode – although this is coupled to a polar (zone centre) Γ_2^- mode.[7]

HIFs are systems that experience separate non-polar modes, with distinct symmetries, which combine to induce a spontaneous polarisation – although these two modes may not condense at the same temperature. This term was first coined by Benedek and Fennie in 2011, to describe how the cooperation of two non-polar octahedral distortion modes induce ferroelectricity (as well as other magnetic properties) in the $Ca_3Mn_2O_7$ Ruddlesden-Popper layered perovskite.[8] As an example, this is achieved by distorting the parent $I4/mmm$ structure with combination of two zone boundary modes: a X_2^+ octahedral rotation mode and a X_3^- tilting mode. These two modes are non-polar but transform the cell into the $A2_1am$ polar space group. – no zone centre distortion mode is required as is found in proper ferroelectrics.[8]

1.10 Topological or Geometric Ferroelectricity

In previous examples of proper ferroelectricity, a simple zone-centre distortion is observed which is induced by an electronic effect (SOJT) that shifts a cation from the negative barycentre of an oxygen octahedra to produce a dipole. Another mechanism which has recently been proposed is 'topological ferroelectricity' where geometric effects - similar to those outlined in improper ferroelectrics - give rise to structural topologies which induce a form of proper ferroelectricity. In regard to the parent phase, the distortion to the ferroelectric structure occurs by zone centre Γ modes and the original number of formula units is retained - thereby adhering to the more simplistic definition of a proper ferroelectric. An example of this is found in the layered perovskite $La_2Ti_2O_7$: the oxygen octahedra adopt an anti-ferrodistortive tilting system at the ferroelectric transition. This manner of tilting is found in conventional perovskites and does not induce any polarisation due to its 3D connectivity. However, due to the layering in $La_2Ti_2O_7$, this tilting system does in fact give rise to a net spontaneous polarisation.[9] Other related materials, such as the widely studied $BaMF_4$ (M = Mn, Fe, Co, Ni, Zn, and Mg) series of layered perovskite fluorides, exhibit a similar mechanism.[10] The complexity of the distortion seems more akin to that observed in the improper ferroelectrics but given the zone-centre nature of the ferroelectric transition, these materials are in fact proper ferroelectrics.

1.11 Layered Perovskites

Layered perovskites have many similarities to their ‘normal’ perovskite counterparts, but their main difference is (as the name suggests) the layering of their structures. This layering occurs from discontinuities (or cleavages) of their usual three-dimensional structure in at least one axis. The nature of the layering is varied, and sub-classes of layered perovskites have been identified, some of which are shown in **figure 1.9**. The structures consist of the same basic building blocks you would find in a conventional perovskite, where A-sites sit within (mostly) square channels, formed by BO_6 octahedra. These materials can layer in various different ways which allows a host of additional A sites to occur with different and unusual geometries and coordination compared to that of ‘normal’ perovskites.

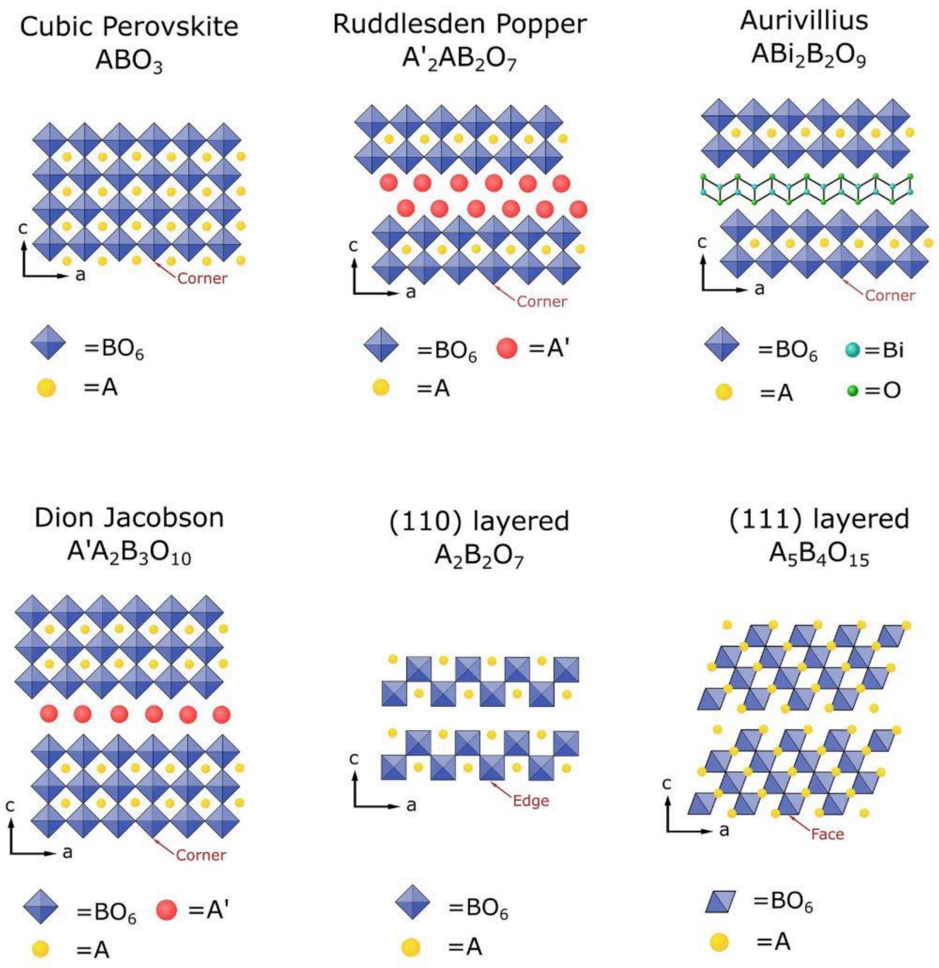

Figure 1.9: Selection of structural models detailing the fashion in which some layered perovskites vary from their three-dimensional counterpart. Often in the Ruddlesden-Popper and Dion Jacobson phases the A and A' cations are the same atom. Reproduced from Ref. 11 with permission from Elsevier.

As mentioned previously, ferroelectricity is observed in the families of layered perovskites shown in **figure 1.9** and in many of these materials this is due to a simple zone-centre shift of the A- and/or B-cation, making them proper ferroelectrics. However, this is not always the case. As with the earlier example of improper ferroelectricity in Ruddlesden-Popper phase $Ca_3Mn_2O_7$, many of these materials exhibit ferroelectricity originating from a combination of non-polar distortions such as the tilting of octahedra. These materials are observed to exhibit improper ferroelectricity by a 'hybrid improper' mechanism, where the polar order parameter is coupled to two other non-polar structural parameters of different symmetry - in what is referred to as 'trilinear coupling'.[12]

There are many examples where these mechanisms of improper ferroelectricity were observed structurally but switching was not observed experimentally until much later (if at all). For example, the Dion-Jacobson phases $CsBiNb_2O_7$ and $RbBiNb_2O_7$ are the most widely studied members of this family. They are confirmed to exist in the polar space group $P2_1am$[13] but ferroelectric switching had not been observed until relatively recently by Chen *et al.*.[14] The ferroelectricity in these materials arise from a displacement of the A and B cations with an accompanying tilt of the octahedra – the displacement of B-cations is similar to that found in proper ferroelectrics but the net polarization is zero due to the presence of mirror symmetry. However, this is not the case for the A-cations as they are displaced parallel to the mirror plane, and this results in a polarization along the *a*-axis. A similar mechanism is also widely observed for the Aurivillius phases.[15a] The displacement of the A atom itself is polar but it is coupled to two nonpolar octahedral rotation modes making this a hybrid improper ferroelectric. Recent work has also shown that for the Dion-Jacobson phases, tuning between proper and improper ferroelectricity is possible, simply through choice of cation.[15b-c]

The layering in these structures also give rise to some unusual structural behaviour when compared to their conventional '3D' counterparts, such as uniaxial negative thermal expansion (NTE). It has been reported that the NTE in rigid inorganic lattices is primarily due to octahedral rotation modes, whose amplitude increases with increasing temperature and causes contraction of a particular axis. Although these rigid unit modes (RUMs) are found in the conventional perovskite structures, these do not show any significant NTE, whereas it is prevalent in their layered counterparts ($LaTaO_4$ or Ca_2GeO_4, for example). It has been suggested that anisotropic elastic compliance and RUMs benefit from the extra degrees of freedom that is afforded by the truncated structure.[16]

1.12 Carpy-Galy Phases

The family of layered perovskites of general formula $A_nB_nX_{3n+2}$ have been of great interest to the ferroelectrics community for a number of decades but only recently has the Carpy-Galy nomenclature been proposed[17] after the authors who first synthesized them and characterised their structure.[18,19] These publications pertain to the material $Ca_2Nb_2O_7$, an n = 4 Carpy-Galy phase which has been investigated in the past for its functional (piezoelectric) properties.[20]

The value of n in the general formula can be taken to represent the depth of the octahedral layers, *i.e.* an n = 4 Carpy-Galy phase will have layers 4 octahedra deep. As the value of n increases, the structure asymptotically approaches that of a normal 3D perovskite, ABO_3, at $n = \infty$. The stoichiometry is often expressed in terms of anion excess ABX_y where $y = 3+2/n$, *i.e.* the n = 4 Carpy-Galy phase is written as $CaNbO_{3.5}$.[21] Anion excess is largest in the n = 2 phase (ABO_4) and decreases with increasing n.[21] The relationship between the value of n and the layering in the structure is illustrated in **figure 1.10.**

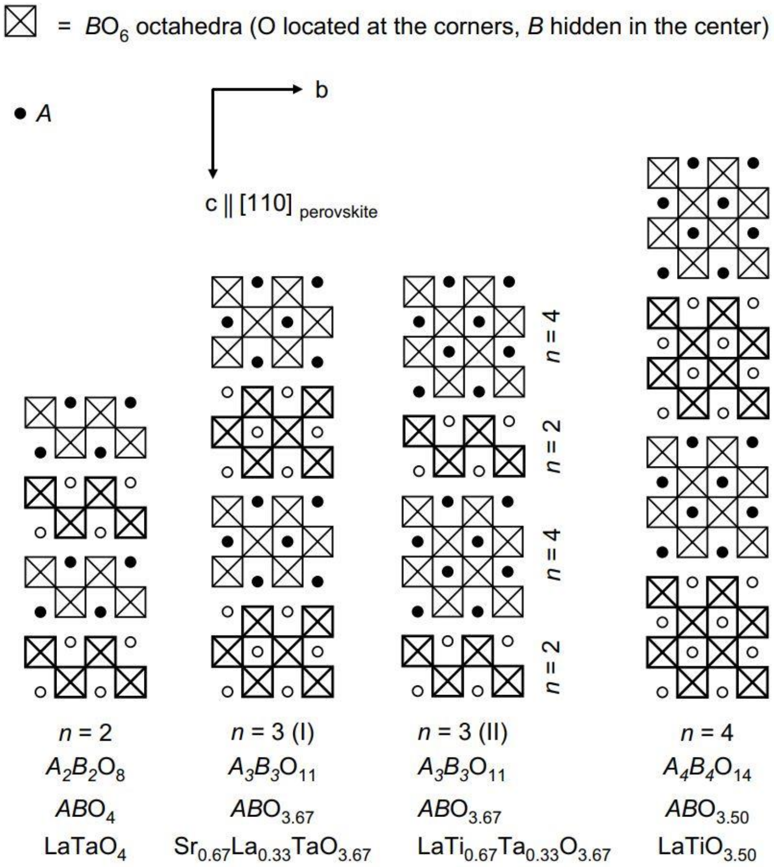

Figure 1.10: Structural diagrams for n = 2 to 4 Carpy-Galy structures, with example compounds given for each. Reproduced from Ref. 22 with permission from Elsevier.

These materials are also commonly referred to as the [110]-phases due to the perovskite layering perpendicular to the {110} plane, with respect to the cubic perovskite structure. The excess anions introduce cleavages in this plane which disrupt the usual 3D octahedral connectivity and create a structure made of octahedral sheets, separated by inter-layer cation environments. This makes this family of materials particularly two-dimensional. Structures of $n > 2$ phases give rise to two separate A-cation environments; an inter-layer A1 site – which has an unusual coordination geometry – and an A2 site within the layers (a typical perovskite A-cation environment); in contrast $n = 2$ phases only contain the inter-layer A-site.

1.13 $n = 2$ Carpy-Galy Fluorides

Of the Carpy-Galy phases there have been none studied more extensively than the family of $n = 2$ fluorides, $BaMF_4$ (M = Mn, Fe, Co, Ni, Zn, and Mg). This is primarily due to the interesting properties which they exhibit, both structurally and functionally - most of these compounds (M = Co, Ni, Zn, and Mg) have been shown experimentally to be ferroelectric, with polarisation switching demonstrated under an applied field.[10] The studies on $BaMF_4$ mostly report this structure in the non-standard $A2_1am$ space group, but to avoid confusion all descriptions will be given in the standard $Cmc2_1$ setting in the following. Each of these materials occupy the polar $Cmc2_1$ space group from room temperature up to their melting point, which affords them the ability to be ferroelectric over a large temperature range. **Figure 1.11** shows the switching mechanism for $BaMnF_4$ – the Ba cations shift along the polar *c*-axis and this is accompanied by a cooperative tilting of the octahedra. The ferroelectric transition occurs by a zone centre Γ_2^- mode which means that these types of materials are proper ferroelectric, but with this resulting from the topology of the layered structure rather than an electronic (SOJT) effect; they can therefore be classed as topological (or geometric) ferroelectrics.

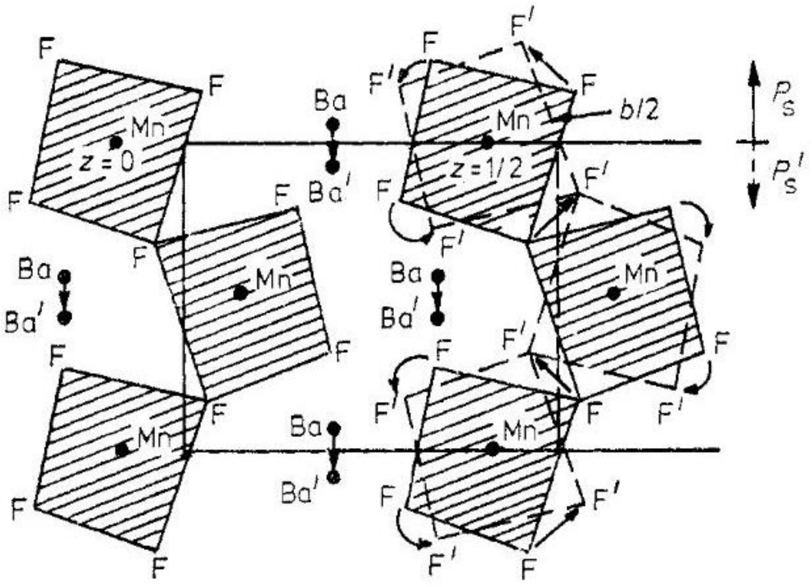

Figure 1.11: Diagram of BaMnF4 viewed along the *a*-axis. The structural distortions involved in the switching of the polarisation are the shift of Ba cations along the polar c axis and an accompanying tilt of MnF_4 octahedra. Reproduced from Ref. 23 with permission from IOP Publishing, Ltd.

One reason that these materials have been studied so widely is that they exhibit multiferroic properties and one of the first and most notable observations of this was in the case of $BaMnF_4$. Fox and Scott hypothesised that a linear magnetoelectric effect existed in $BaMnF_4$ which was induced by spin canting in the ferroelectric phase, with the dipole and magnetic moments being inherently linked. The relationship between these two properties was demonstrated experimentally and in cases where the spin canting was eliminated by doping with cobalt, the ferromagnetism (and hence the magnetoelectric properties) disappeared.[24,25] Ferroelectric switching in this material has, however, never been observed experimentally.[26] Ederer and Spaldin later used first principal calculations to detail the mechanism for magnetoelectricity in $BaNiF_4$. They show that the polar structural distortion is coupled to the magnetic ordering; the magnetic moment of the structure aligns with the electric polarization and subsequently the direction of the magnetic moment is switchable by an applied electric field.[27]

$BaMnF_4$ is of particular interest when studying $LaTaO_4$ because of both the interest it gained in the context of ferroelectric applications and the unusual structural characteristics it exhibits. Untangling the exact configuration of the unit cell and the structural transitions in $BaMnF_4$ was a process which took many years. The low temperature structural behaviour (which are not exhibited by other members of the $BaMF_4$ family) are attributed to the large Mn^{2+} cation which occupies the B-site.[23] The most interesting of these features is the observation of a series of modulated structures below 250 K.[28] The transition between a commensurate and incommensurate structure was first indicated by an observed peak in permittivity, reported by Samara and Richards.[29]

At temperatures below the incommensurate – commensurate transition ($T_{IC\text{-}C}$) $BaMnF_4$ is found to have a modulation vector of q = (0.5, 0.5, ~0.4), which denotes a cell doubling in both *a* and *b* axes, and an expansion of the original cell by approximately 2.5 in the *c*-axis.[28] This observation of an incommensurate modulation along the polar axis was then elaborated upon by subsequent neutron studies which revealed that this was the first step in a 'devils staircase', where the modulation vector would change in a step-wise fashion with varying *T*.[26,30–33] Interestingly, it was also concluded by Scott and Tilley, that the observation of an incommensurate phase in $BaMnF_4$ had a detrimental effect on the magnetic structure of the material and hence greatly affected the magnetoelectric properties.[34]

1.14 *n* = 4 Carpy-Galy Oxides

There are very few Carpy-Galy oxides which are isostructural to the analogous *n* = 2 fluoride series but there has been some interest in the *n* = 4 oxides. $La_2Ti_2O_7$ and $Sr_2Nb_2O_7$ are two known ferroelectric materials which also assume the polar $Cmc2_1$ space group and present interesting properties. Firstly, $La_2Ti_2O_7$ presents a very high T_C (1770 K) in comparison to standard perovskites and is one of the highest Curie temperatures reported.[9] Interestingly, $La_2Ti_2O_7$ also exhibits a modulated phase between 989 and 1080 K, but unlike $BaMnF_4$, this is an intermediate phase which lies between a low temperature monoclinic phase and a high temperature orthorhombic phase. The incommensuration in $La_2Ti_2O_7$ is generated by a variation in octahedral tilting along the *a*-axis – the tilting between each octahedral layer is out of phase by ½, which generates a modulated structure where units of both the low temperature monoclinic and high temperature orthorhombic structure can be identified to coexist (**figure 1.12**).[35]

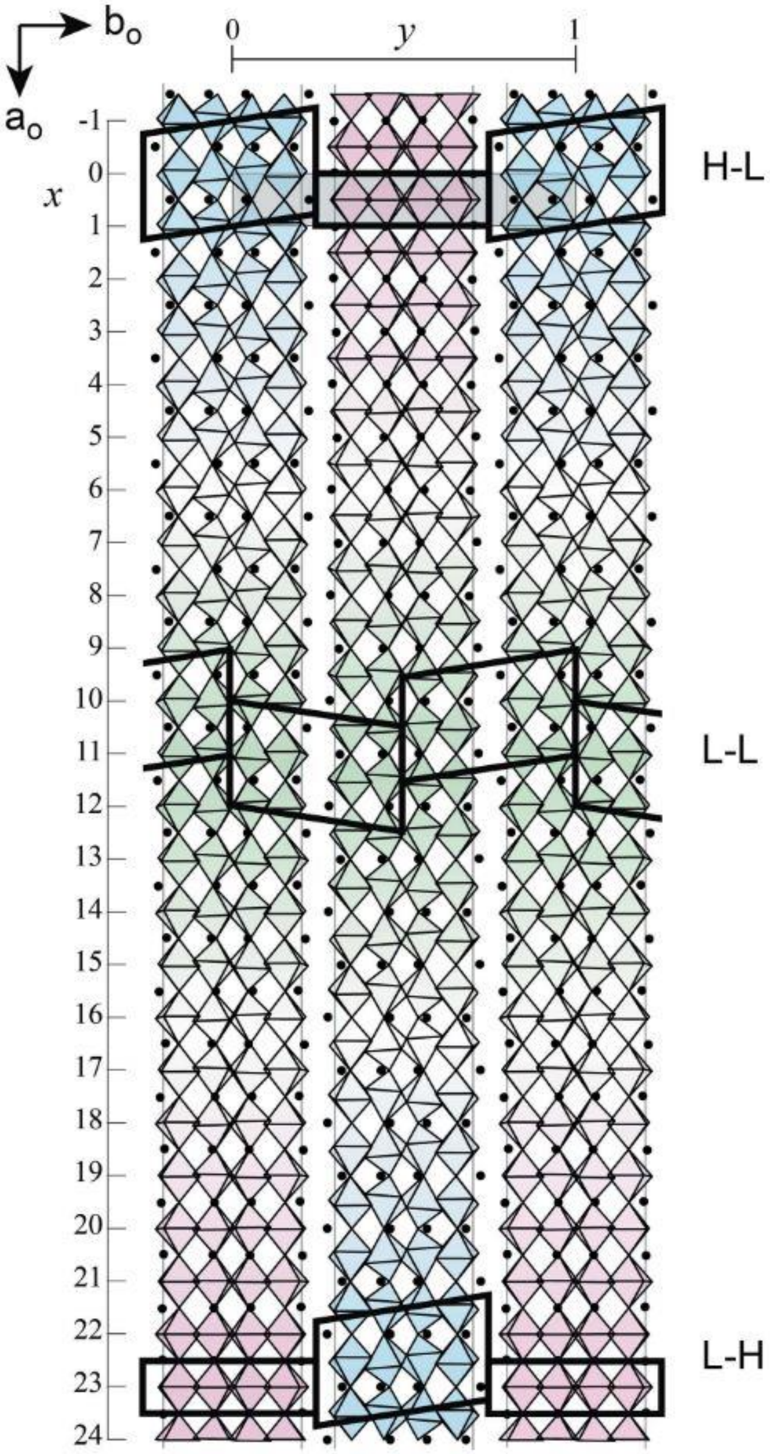

Figure 1.12: Projection of the intermediate incommensurate phase of $La_2Ti_2O_7$, which is constructed of combinations of the low and high temperature units (outlined). The letter H denotes the presence of a high temperature orthorhombic unit and L marks the presence of a low temperature monoclinic unit. H-L, L-L, and L-H denote the combination of units. Reproduced from Ref. 35 with permission from IUCr journals.

Ferroelectric $Sr_2Nb_2O_7$ is very similar in many ways to $La_2Ti_2O_7$, as it maintains a comparatively high T_C of 1615 K[36] and exhibits a modulated orthorhombic structure below 488 K. The first observed evidence of this modulation was reported by Yamamoto *et al.* in 1980 in an electron diffraction study which suggested an approximate cell doubling along the *a*-axis.[37] It is important to note that in both $Sr_2Nb_2O_7$ and $La_2Ti_2O_7$, the modulation runs orthogonal to the polar *c* axis, in contrast to $BaMnF_4$ where the modulation runs along the polar axis. The modulation in $Sr_2Nb_2O_7$ was more fully elucidated by Daniels *et al.*[38] and is much simpler than that observed in $La_2Ti_2O_7$. The modulation is described by a mechanism which acts to alleviate the unusually short bond lengths found in the basic (unmodulated) structure. This is achieved by modulating the position of the Sr^{2+} cations in a sinusoidal manner – the A-cations located between the octahedral layers being more affected than those occupying the internal perovskite-like sites.

1.15 Lanthanum Tantalate

Lanthanum tantalate, $LaTaO_4$, is a particularly interesting example of a Carpy-Galy phase as it is one of very few $n = 2$ oxides, but which also includes $PrTaO_4$ and $CeTaO_4$. Other materials of the ABO_4 stoichiometry typically adopt the scheelite structure at room temperature.[39] $LaTaO_4$ is generally isostructural to the $BaMF_4$ (M = Mn, Fe, Co, Ni, Zn, and Mg) family of materials but has been shown to possess some structural similarities to the $n = 4$ oxides – these are elucidated over the course of this thesis. Although $LaTaO_4$ has not been studied as extensively as some other layered perovskites, several studies have reported on the structural characterisation of this material. Under ambient conditions $LaTaO_4$ will usually occupy the monoclinic $P2_1/c$ phase but upon heating to *ca*. 440 K undergoes a first order phase transition to the polar orthorhombic $Cmc2_1$ structure (each structure is shown in **figure 1.13**, relative to the undistorted parent *Cmcm* structure).

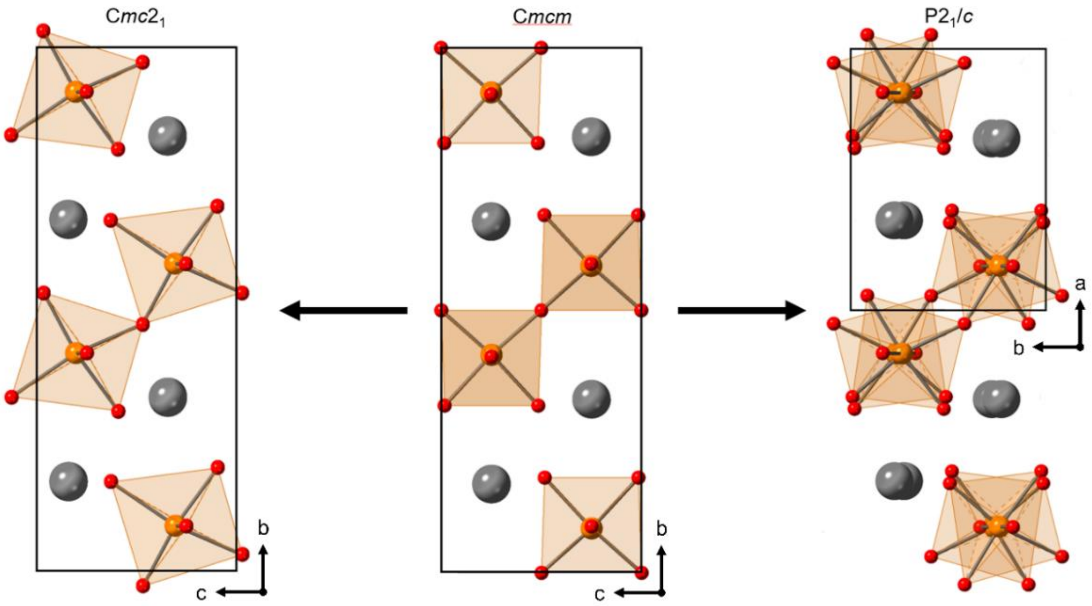

Figure 1.13: Untilted parent *Cmcm* phase of $LaTaO_4$ with polar orthorhombic *Cmc*2_1 and centrosymmetric monoclinic *P*2_1/*c* phases – both of which are subgroups of *Cmcm* but unrelated to each other by a simple distortion mode.

The first in depth structural characterization of $LaTaO_4$ was presented by Cava and Roth in a neutron diffraction study, which described the orthorhombic phase to be isostructural to room temperature $BaMnF_4$ at 573 K.[39] As with other n = 2 Carpy-Galy phases it then assumes a monoclinic structure at lower temperatures. The shift between the two polymorphs shows no great deal of reconfiguration of the octahedral layers, other than an onset of antiferrodistortive tilting on transitioning to the monoclinic phase. In this study, authors note the similarities between $LaTaO_4$ and $BaMnF_4$, and even mention the incommensurate-commensurate transition in the fluoride (but the possibility of a modulation in $LaTaO_4$ was not addressed).[39] As discussed previously, the observation of a polar (and potentially ferroelectric) structure can come many years before ferroelectric switching is observed experimentally (if at all)[13,14] and this seems to be the case for $LaTaO_4$. As $LaTaO_4$ is isostructural to the $BaMF_4$ (M = Mn, Fe, Co, Ni, Zn, and Mg) family of materials it would be expected that the mechanism for switching spontaneous polarisation is identical and structurally plausible. First principles calculations estimate the spontaneous polarization of $LaTaO_4$ to be ~36 $\mu C/cm^2$ – which is comparable to $BaTiO_3$.[40]

The $Cmc2_1$ and $P2_1/c$ structures are sub-groups of the parent 'untilted' *Cmcm* phase, but unrelated to each other by a simple distortion mode. The *Cmcm* phase has never been observed experimentally, as samples will melt before this transition temperature is reached. The phase transition sequence previously established for $LaTaO_4$ is as follows (on cooling from left to right):

$$Cmcm\ \text{(orthorhombic)} \overset{T > \text{M.P.}}{\longleftrightarrow} Cmc2_1\ \text{(orthorhombic)} \overset{440\ K}{\longleftrightarrow} P2_1/c\ \text{(monoclinic)}$$

The transition from the parent structure to the ferroelectric phase proceeds by a combination of two zone centre gamma modes (Γ_1^+ and Γ_2^-) which shift the A-cations and distort the BO_6 octahedra.[40] As the ferroelectricity is induced by the truncated nature of the structure (in a similar way to $La_2Ti_2O_7$) this material is classed as a topological (geometric) ferroelectric.

The polymorph which $LaTaO_4$ occupies at ambient conditions has been a common point of discussion in previous investigations. The earliest structural characterisation by Cava and Roth synthesised single crystal $LaTaO_4$ from a melt, which consistently shattered upon cooling. This was attributed to the fact that $LaTaO_4$ would undergo a phase transition from orthorhombic to monoclinic as it is brought to room temperature.[39] Other studies have also found that samples of $LaTaO_4$ will tend to adopt the monoclinic space group under ambient conditions.[41,42] Attempts to produce single phase samples of each polymorph by Vullum *et al.* found that the application of pressure to samples by pressing them into pellets before annealing favoured the monoclinic structure due to the lower molar volume of this phase compared to the orthorhombic one.[43]

Similarly, Cordrey *et al.* reported that other processing methods could greatly influence the stability of each polymorph. In this study, ceramic samples were prepared by high energy ball milling, which directed the stabilisation of the $Cmc2_1$ phase under ambient conditions. A single phase sample was never achieved but the vast majority of the phase volume was orthorhombic. Samples which were prepared this way could only be stabilised in the monoclinic polymorph by Nd-doping, where the smaller A-cations sterically induced the $P2_1/c$ phase.[44] This seems to build on the findings of Vullum *et al.*[43], where doping with smaller A-cations favours the monoclinic phase by means of chemical pressure. It is found that substituting Nd^{3+} into 10% of the A-sites caused the monoclinic-orthorhombic phase transition to increase in temperature by ~130 K (when compared to other monoclinic samples).[44]

Other doped $LaTaO_4$ compounds have also been produced and show that small compositional changes can greatly influence the stability of each phase. In the work by Vullum *et al.*, the authors produced the series $LaNb_{1-x}Ta_xO_4$ (x = 0.2, 0.4, 0.6, 0.8 and 1) and showed that a 20% substitution of Nb for Ta resulted in 140 K decrease in the monoclinic to orthorhombic transition temperature. This study also highlighted the difficulty that is faced when producing single phase $LaTaO_4$, as samples with higher Ta content usually yielded a monoclinic / orthorhombic phase mixture, a problem also encountered by other studies.[44]

A first principles study of $LaTaO_4$ revealed many interesting aspects of this material. The energy barrier which separates the parent *Cmcm* and ferroelectric $Cmc2_1$ phase is relatively small and the barrier which separates the $Cmc2_1$ and $P2_1/c$ phase is similarly low. This lead the authors of this study to conclude that the ferroelectric phase is only metastable[40] and this is consistent with some experimental observations made in previous studies, such as the stabilisation of the $Cmc2_1$ phase at room temperature by high energy ball milling.[44]

Dielectric spectroscopy has been used in at least two studies of $LaTaO_4$[42,44] and produced very similar results. Both showed a large dielectric anomaly with a thermal hysteresis of ~200 K at the monoclinic-orthorhombic transition. The dielectric data obtained by Cordrey *et al.* on both undoped and 10% Nd-doped $LaTaO_4$ is shown in **figure 1.14**. In both cases, a somewhat smaller dielectric anomaly with no thermal hysteresis is also observed. In orthorhombic samples, this dielectric anomaly is rather broad with a maximum at approximately 473 K. In the monoclinic samples this peak exists at ~50 K above the orthorhombic – monoclinic transition. All structural studies of $LaTaO_4$ prior to the publications by Cordrey *et al.* and Abreu *et al.* show no evidence of a second phase transition above the monoclinic – orthorhombic transition at ~440 K and no evidence of any intermediate phases occupied by $LaTaO_4$ in this temperature range.

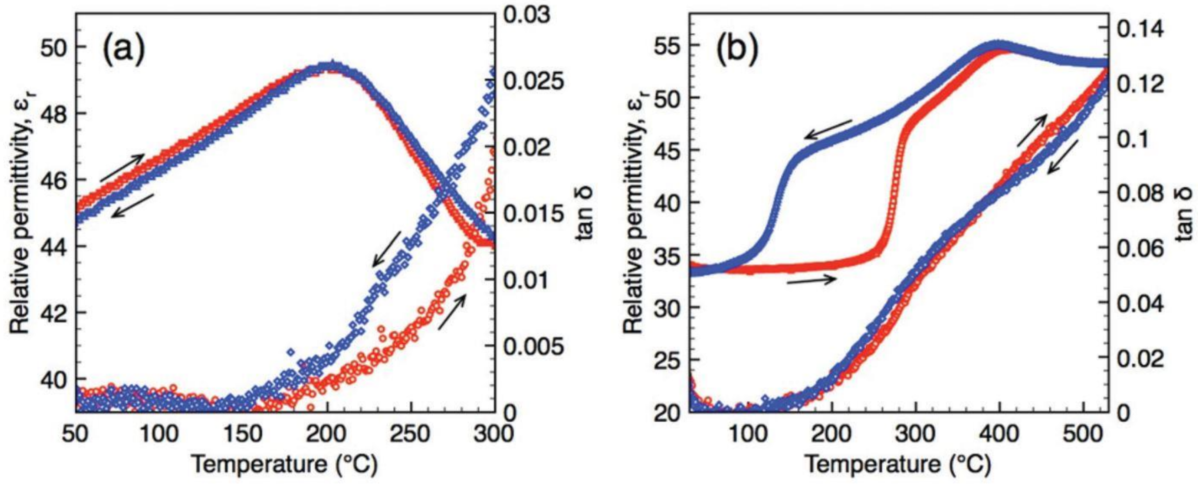

Figure 1.14: Dielectric spectroscopy data for (a) o-LaTaO4 and (b) m-La0.9Nd0.1TaO4 from Cordrey et al.45 (a) Orthorhombic LaTaO4 shows a broad, unidentified dielectric anomaly at ~200 °C. (b) monoclinic La0.9Nd0.1TaO4 shows a peak in permittivity with large thermal hysteresis between 100 °C and 300 °C indicative of the transition between monoclinic P21/c and orthorhombic Cmc21 phases. An unidentified broad dielectric anomaly at ~400 °C, similar to that in o-LaTaO4, is also observed.

In the study by Abreu *et al.* Raman spectroscopy was used to investigate the origin of this unidentified dielectric peak at high temperature. The authors assigned this dielectric peak to a transition to the *Cmcm* phase, arguing that the number of Raman peaks present above the anomaly is consistent with the untilted parent phase.[42] However, this conclusion is incorrect as even the earliest studies on $LaTaO_4$ show that the $Cmc2_1$ structure is maintained to at least 573 K[39], and the more recent study by Cordrey *et al*. shows that this structure persists up to at least 773 K.[44] Although no direct evidence is presented, Cordrey *et al*. also speculated that the dielectric anomaly may denote an incommensurate – commensurate phase transition. This seems like the most likely explanation as modulated structures are commonly observed in the *n* = 2 and *n* = 4 Carpy-Galy phases and would account for the observation of the $Cmc2_1$ structure at either side of the dielectric anomaly – the satellite reflections generated from a modulated structure may be too subtle to observe in previous data sets.

The neutron diffraction study presented by Cordrey *et al.* did show some clear changes in the thermal expansion of $LaTaO_4$ which coincides with the unidentified dielectric anomaly, which suggests that subtle structural changes occur in this region. **Figure 1.15** shows the lattice parameters of $LaTaO_4$ as a function of temperature as determined by Cordrey *et al.*[44]

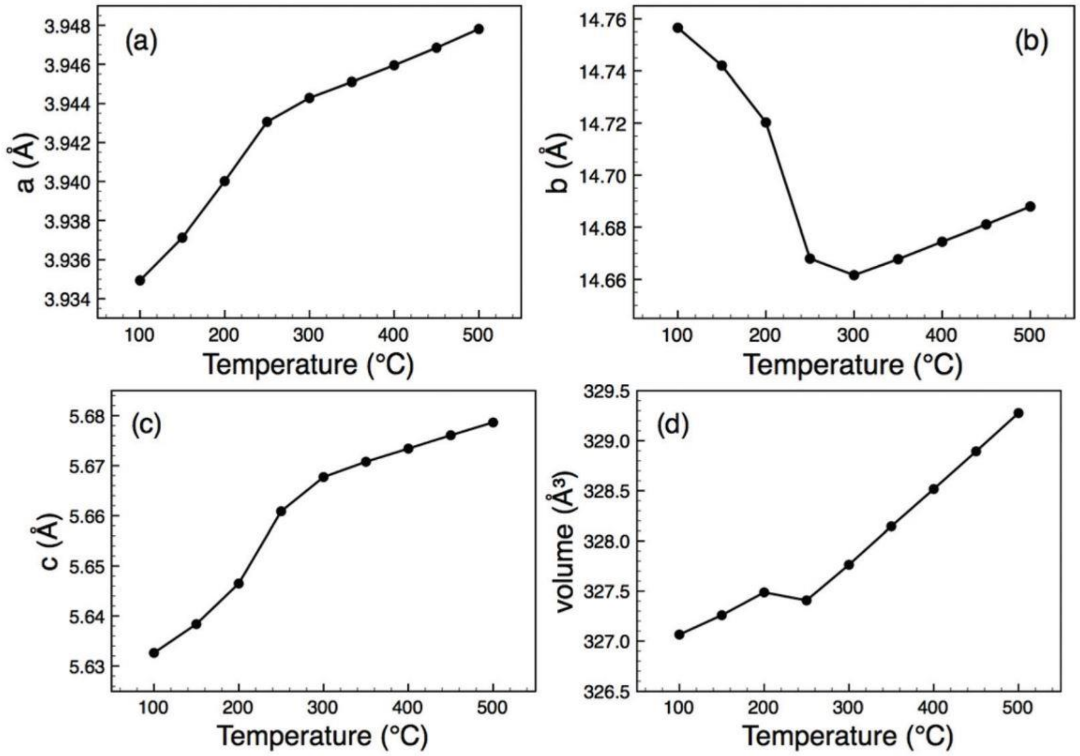

Figure 1.15: Lattice parameter data for $LaTaO_4$ plotted as a function of temperature, taken from the neutron diffraction study by Cordrey et al..[44] The inflections in the *a*, *c* and volume parameters, and the shift from negative (NTE) to positive (PTE) thermal expansion in the *b* axis, coincide with the observed high temperature peak in relative permittivity.

The data in **figure 1.15** shows a somewhat unusual trend in the lattice parameters. The *a* and *c* parameters show a typical positive thermal expansion (PTE) and the *b* parameter contracts with increasing *T* (negative thermal expansion, NTE). It is observed that the NTE in the *b* axis exists up to ~573 K – which is approximately the temperature at which the second dielectric peak is observed – and beyond this the *b* parameter reverts to normal PTE. A study by Ablitt *et al.* utilises a combination of structural data and DFT calculations to explore the origin of NTE of $LaTaO_4$ and a selection of other layered perovskites. The authors surmise that this behaviour arises as a consequence of the layered structures, and that there exists a coupling between the cell axes and the internal structural degrees of freedom – specifically the octahedral rotations.[16] This may describe the origin of NTE in $LaTaO_4$ but it does not clarify why the *b* axis suddenly reverts back to PTE at ~573 K. Furthermore, the connection between the dielectric anomaly and the onset of PTE in the *b*-axis has never been explored in any previous study.

1.16 Thesis Overview

In this thesis the structural properties of $LaTaO_4$ are re-examined and a previously unidentified incommensurately modulated (IC) phase is found to exist between the monoclinic $P2_1/c$ and orthorhombic $Cmc2_1$ phase. This study describes the synthesis of monoclinic and orthorhombic polymorphs of $LaTaO_4$, the identification and elucidation of the incommensurate structure, and revision of the phase transition sequence.

The second chapter provides background information regarding the techniques used to create and characterise the materials. General methods of sample preparation are described and structural characterisation methods such as powder x-ray diffraction (PXRD) and powder neutron diffraction (PND) are explained. Most importantly, the concept of 3D+*n* crystallography is introduced as a means of fully describing the complex structure of the modulated phase – with the periodicity of the structure not being confined to a simple unit cell, a mathematical approach to describing the variation in atomic configurations between cells arranged along the modulated axis is presented.

Chapter 3 presents data which initially identifies the presence of the modulated structure, and the phase transition sequence is then explored and updated in light of this. Dielectric spectroscopy and PXRD data show evidence of subtle structural changes which occur at 480 - 500 K and this is revealed by means of PND to be an incommensurate commensurate transition. A combination of PND, Raman and Resonant Ultrasound Spectroscopy (RUS) are used to probe the dynamics of the phase transition sequence, identifying the transition between the monoclinic and IC orthorhombic phase to be necessarily first order, and the transition between the modulated and unmodulated orthorhombic phases to be also first order but almost continuous (tri-critical).

Chapter 4 pertains to the full structural characterisation of the modulated phase. The PND data discussed in Chapter 3 is used to refine a 3D+1 model of the IC orthorhombic phase where a macroscopic modulation vector, *q*, and a superspace group of $Cmc2_1(\alpha00)0s0$ is determined. Electron microscopy data is presented which shows that the local origin of the incommensuration is a partial ordering of subunits which are 3× and 2.5× expansions of the original $Cmc2_1$ cell. Both sets of data are combined to produce a structural model which accounts for the partially ordered local structure and the ‘average’ macroscopic ~11× expansion.

Previous studies of $LaTaO_4$ have used A-site doping to stabilise the monoclinic phase at room temperature which results in a shift of all the phase transition temperatures. Chapter 5 explores the series $La_{1-x}Ln_xTaO_4$ (Ln = La^{3+}, Ce^{3+}, Pr^{3+}, Nd^{3+}) to investigate the effect that A-cation doping has on the stability of the modulated phase. Dielectric spectroscopy is utilised to map the phase transition sequence of each composition ($0 \leq x \leq 0.3$) to show that the shift in transition temperature is due to the chemical pressure induced by the size mismatch between the A-cation and A-site environment.

1.17 References

1. Moulson, A. J. & Herbert, J. M. *Electroceramics: Materials, Properties, Applications*. (St. Edmundsbury Press, 1990).

2. Ferroelectric Materials for Energy Applications. Germany: Wiley, (2019).

3. Jaffe, B., Cook, W. R. & Jaffe, H. *Piezoelectric Ceramics*. (Academic Press, 1971).

4. Ok, K. M. *et al.* Distortions in Octahedrally Coordinated d_0 Transition Metal Oxides: A Continuous Symmetry Measures Approach. *Chem. Mater.* **18**, 3176–3183 (2006).

5. Levanyuk, A. P. & Sannikov, D. G. Improper Ferroelectrics. **17**, 561–589 (1974).

6. Van Aken, B. B., Palstra, T. T. M., Filippetti, A. & Spaldin, N. A. The Origin of Ferroelectricity in Magnetoelectric $YMnO_3$. *Nat. Mater.* **3**, 164–170 (2004).

7. Gibbs, A. S., Knight, K. S. & Lightfoot, P. High-temperature Phase Transitions of Hexagonal $YMnO_3$. *Phys. Rev. B - Condens. Matter Mater. Phys.* **83**, 1–9 (2011).

8. Benedek, N. A. & Fennie, C. J. Hybrid Improper Ferroelectricity: A Mechanism for Controllable Polarization-Magnetization Coupling. *Phys. Rev. Lett.* **106**, 3–6 (2011).

9. López-Pérez, J. & Íñiguez, J. Ab Initio Study of Proper Topological Ferroelectricity in Layered Perovskite $La_2Ti_2O_7$. *Phys. Rev. B - Condens. Matter Mater. Phys.* **84**, 1–13 (2011).

10. Ederer, C. & Spaldin, N. A. Origin of Ferroelectricity in the Multiferroic Barium Fluorides $BaMF_4$: A First Principles Study. *Phys. Rev. B - Condens. Matter Mater. Phys.* **74**, (2006).

11. Hu, Y. *et al.* Layered Perovskite Oxides and their Derivative Nanosheets Adopting Different Modification Strategies Towards Better Photocatalytic Performance of Water Splitting. *Renew. Sustain. Energy Rev.* **119**, 109527 (2020).

12. Benedek, N. A., Rondinelli, J. M., Djani, H., Ghosez, P. & Lightfoot, P. Understanding Ferroelectricity in Layered Perovskites: New Ideas and Insights from Theory and Experiments. *Dalt. Trans.* **44**, 10543–10558 (2015).

13. Snedden, A., Knight, K. S. & Lightfoot, P. Structural Distortions in the Layered Perovskites $CsANb_2O_7$ (A=Nd, Bi). *J. Solid State Chem.* **173**, 309–313 (2003).

14. Chen, C. *et al.* Ferroelectricity in Dion-Jacobson $ABiNb_2O_7$ (A = Rb, Cs) Compounds. *J. Mater. Chem. C* **3**, 19–22 (2015).

15a. Champarnaud-Mesjard, J.-C., Frit, B. & Watanabe, A. Crystal Structure of $Bi_2W_2O_9$, the n=2 Member of the Homologous Series $(Bi_2O_2)BVInO_{3n+1}$ of Cation-Deficient Aurivillius phases. *J. Mater. Chem.* **9**, 1319–1322 (1999).

15b. Zhu, T., Gibbs, A. S., Benedek, N. A. & Hayward, M. A. Complex Structural Phase Transitions of the Hybrid Improper Polar Dion-Jacobson Oxides $RbNdM_2O_7$ and $CsNdM_2O_7$ (M = Nb, Ta). Chem. Mater. 32, 4340–4346 (2020).

15c. Zhu, T. et al. Theory and Neutrons Combine to Reveal a Family of Layered Perovskites without Inversion Symmetry. Chem. Mater. 29, 9489–9497 (2017).

16. Ablitt, C., Craddock, S., Senn, M. S., Mostofi, A. A. & Bristowe, N. C. The Origin of Uniaxial Negative Thermal Expansion in Layered Perovskites. *npj Comput. Mater.* **3**, 44 (2017).

17. Núñez Valdez, M. & Spaldin, N. A. Origin and Evolution of Ferroelectricity in the Layered Rare-Earth-Titanate, $R_2Ti_2O_7$, Carpy-Galy phases. *Polyhedron* **171**, 181–192 (2019).

18. Carpy, A., Amestoy, P. & Galy, J. Contribution à l'étude du Pyroniobate de Calcium $Ca_2Nb_2O_7$. *CR Acad. Sci. Paris C* **275**, 833 (1972).

19. Carpy, A., P. Amestoy, and J. Galy. 'Système $Ca_2Nb_2O_7$-$NaNbO_3$: Synthèse et Étude Radiocristallographique de Membres de la Série $A_nB_nX_{3n+2}$ (n ¼ 4, 5, 6).' CR Acad. Sci. Paris C 277 (1973).

20. BALLMAN, A. A. Growth of Piezoelectric and Ferroelectric Materials by the Czochralski Technique. *J. Am. Ceram. Soc.* **48**, 112–113 (1965).

21. Lichtenberg, F., Herrnberger, A., Wiedenmann, K. & Mannhart, J. Synthesis of Perovskite-Related Layered $A_nB_nO3_{n+2}$ = ABO_X Type Niobates and Titanates and Study of their Structural, Electric and Magnetic Properties. *Prog. Solid State Chem.* **29**, 1–70 (2001).

22. Lichtenberg, F., Herrnberger, A. & Wiedenmann, K. Synthesis, Structural, Magnetic and Transport Properties of Layered Perovskite-Related Titanates, Niobates and Tantalates of the Type $A_nB_nO_{3n+2}$, $A'A_{k-1}B_kO_{3k+1}$ and $A_mB_{m-1}O_{3m}$. *Prog. Solid State Chem.* **36**, 253–387 (2008).

23. Scott, J. F. Phase Transitions in $BaMnF_4$. *Reports Prog. Phys.* **42**, 1055–1084 (1979).

24. Fox, D. L. & Scott, J. F. Ferroelectrically Induced Ferromagnetism. *J. Phys. C Solid State Phys.* **10**, 19–22 (1977).

25. Fox, D. L., Tilley, D. R., Scott, J. F. & Guggenheim, H. J. Magnetoelectric phenomena in $BaMnF_4$ and $BaMn_{0.99}Co_{0.01}F_4$. *Phys. Rev. B* **21**, 2926–2936 (1980).

26. Scott, J. F. & Blinc, R. Multiferroic Magnetoelectric Fluorides: Why are there so Many Magnetic Ferroelectrics? *J. Phys. Condens. Matter* **23**, 1–17 (2011).

27. Ederer, C. & Spaldin, N. A. Electric-field-switchable magnets: The Case of $BaNiF_4$. *Phys. Rev. B - Condens. Matter Mater. Phys.* **74**, 1–4 (2006).

28. Cox, D. E., Shapiro, S. M., Cowley, R. A., Eibschütz, M. & Guggenheim, H. J. Magnetic and Structural Phase Transitions in $BaMnF_4$. *Phys. Rev. B* **19**, 5754–5772 (1979).

29. Samara, G. A. & Richards, P. M. Low-Temperature Dielectric Properties and Phase Transition in $BaMnF_4$. *Phys. Rev. B* **14**, 5073–5079 (1976).

30. St-Gregoire, P. *et al.* On the Incommensurate Phase in $BaMnF_4$: A Neutron Scattering Study. Effect of the pressure. *Ferroelectrics* **53**, 307–310 (1984).

31. Hidaka, M., Scott, J. F. & Storey, J. S. Energy dispersive X-ray Diffraction Study of Structural Phase Transitions in $BaMnF_4$. *Phys. B+C* **123**, 291–299 (1984).

32. Scott, J. F., Habbal, F. & Hidaka, M. Phase Transitions in $BaMnF_4$: Specific Heat. *Phys. Rev. B* **25**, 1805–1812 (1982).

33. Hidaka, M., Nakayama, T., Scott, J. F. & Storey, J. S. Piezoelectric Resonance Study of Structural Anomalies in $BaMnF_4$. *Phys. B+C* **133**, 1–9 (1985).

34. Scott, J. F. & Tilley, D. R. Magneto-electric Anomalies in $BaMnF_4$. *Ferroelectrics* **161**, 235–243 (1994).

35. Ishizawa, N., Ninomiya, K. & Wang, J. Structural Evolution of $La_2Ti_2O_7$ at Elevated Temperatures. *Acta Crystallogr. Sect. B Struct. Sci. Cryst. Eng. Mater.* **75**, 257–272 (2019).

36. Ohi, K. & Kojima, S. Successive Phase Transitions and Their Soft Modes in Ferroelectric $Sr_2Nb_2O_7$. *Jpn. J. Appl. Phys.* **24**, 817–819 (1985).

37. Yamamoto, N., Yagi, K., Honjo, G., Kimura, M. & Kawamura, T. New Phases of $Sr_2Ta_2O_7$and $Sr_2Nb_2O_7$found by Electron Microscopy and Diffraction. *Journal of the Physical Society of Japan* **48**, 185–191 (1980).

38. Daniels, P. *et al.* The incommensurate Modulation of the Structure of $Sr_2Nb_2O_7$. *Acta Crystallogr. Sect. B Struct. Sci.* **58**, 970–976 (2002).

39. Cava, R. J. & Roth, R. S. The Structure Analysis of $LaTaO_4$ at 300 °C by Neutron Powder Profile Analysis. *J. Solid State Chem.* **36**, 139–147 (1981).

40. Liu, X. Q., Li, G. J. & Chen, X. M. Topological Ferroelectricity in Layered Perovskite $LaTaO_4$: A First Principles Study. *Solid State Commun.* **247**, 31–35 (2016).

41. Siqueira, K. P. F. & Dias, A. Effect of the Processing Prameters on the Crystalline Structure of Lanthanide Orthotantalates. *Mater. Res.* **17**, 167–173 (2014).

42. Abreu, Y. G., Siqueira, K. P. F., Matinaga, F. M., Moreira, R. L. & Dias, A. High-Temperature Antiferroelectric and Ferroelectric Phase Transitions in Phase Pure $LaTaO_4$. *Ceram. Int.* **43**, 1543–1551 (2017).

43. Vullum, F., Nitsche, F., Selbach, S. M. & Grande, T. Solid Solubility and Phase Transitions in the System $LaNb_{1-x}Ta_xO_4$. *J. Solid State Chem.* **181**, 2580–2585 (2008).

44. Cordrey, K. J. *et al.* Structural and Dielectric Studies of the Phase Behaviour of the Topological Ferroelectric $La_{1-x}Nd_xTaO_4$. *Dalt. Trans.* **44**, 10673–10680 (2015).

2 Chapter 2: Experimental Methods

2.1 Ceramic Synthesis

All materials in this project were produced by solid-state ceramic synthetic methods using metal oxide and nitrate precursor powders. Different desired products required individual preparation methods and specific details will be given in the appropriate results chapters, but the general method is outlined here.

Starting materials were dried at high temperature for 1 hour prior to use (RE_2O_3 at 1273 K and Ta_2O_5 at 873 K) and mixed together in stoichiometric amounts in an agate mortar and pestle or Fritz Pulverisette planetary ball mill. Grinding by mortar and pestle was carried out as an acetone slurry for at least 15 minutes. For ball milling samples were placed in an agate pot with agate balls (5 – 10 mm) as milling media and topped up with ethanol to form a slurry, before being milled at 600 rpm for 1 hour.

After drying the mixed powders were pressed into 10 mm diameter cylindrical pellets by either uniaxial hand pressing or isostatic pressing at 30,000 PSI. Samples were then seated in a platinum lined alumina boat before being placed in a box furnace and sintered at temperatures between 1623 – 1923 K. Samples were placed in the furnace at 1223 K and ramped to the desired reaction temperature at 5 K/min, with a dwell time of 6 hours before returning to 1223 K, and then air quenched. Samples produced by this procedure were high quality, suitably dense ceramics (>70%), **figure 1**, and electrical characterisation could be performed without need for further sintering.

Figure 2.1: Ceramic pellet of $LaTaO_4$ ~10 mm diameter pressed at 30,000 psi and heated to 1923 K for 6 hrs. Theoretical density ≈ 75%.

2.2 Powder X-ray Diffraction (PXRD)

All materials produced in this project were characterised by powder x-ray diffraction. Powder samples were loaded into stainless steel disks (**figure 2.2**) and placed into a PANalytical EMPYREAN Bragg-Brentano diffractometer. This used a Cu radiation source with a primary beam monochromator (Cu Kα_1) and X'celerator RTMS detector. Diffraction patterns were collected at room temperature in the 2θ range of 5 – 90° collected over 1 hour (step size 0.0167° 2θ). Sintered pellets were analysed in the same way by securing them into the disks with Blu-tack™.

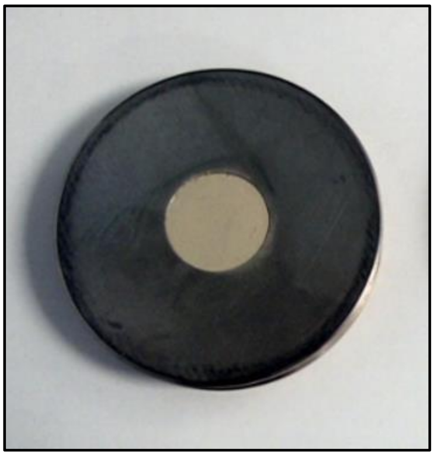

Figure 2.2: Stainless steel PXRD sample holder with powder inside. Central cavity is filled with material until it is flush with the holder surface.

2.3 Variable Temperature X-ray Diffraction (VT-PXRD)

X-ray patterns were collected above room temperature in a similar manner to that outlined above. Powder samples were loaded into an alumina disk before being placed into a PANalytical EMPYREAN Bragg-Brentano diffractometer with a fitted Anton Paar HTK1200N heating stage. This setup used a Mo radiation source with a β-filter (Mo K$\alpha_{1,2}$) and X'celerator RTMS detector. Data was collected over the 2θ range of 5 – 35° for 1 hour, at temperatures ranging from room temperature to 793 K. The heating stage increased sample temperature at a rate of 5 K/min and samples were allowed to equilibrate for 15 min before collecting diffraction data.

2.4 Powder Neutron Diffraction (PND)

More precise structural characterisation of $LaTaO_4$ samples was carried out using powder neutron diffraction at the ISIS neutron spallation source using the high-resolution powder diffractometer (HRPD). This instrument utilises time-of-flight (TOF) neutron diffraction where the time taken for a neutron to travel from the source to the detector can be measured and can be used to calculate its wavelength, as shown in equation 2.1.

$$\lambda = \left(\frac{h}{ml}\right) t \tag{2.1}$$

Where wavelength, λ, and TOF, t, are related by Planck's constant, h, the mass of the neutron, m, and the distance which it travels, l, which is fixed. As with x-ray diffraction the Bragg equation is then employed to calculate the d-spacings:

$$\lambda = 2d\sin\theta = \left(\frac{h}{ml}\right) t \tag{2.2}$$

In contrast with x-ray diffraction, neutron scattering can be more effective in determining structural data for lighter (low atomic number, Z) elements. X-ray diffraction relies on the interaction between x-ray photons and the electron cloud surrounding each atom which therefore scales with the electron density of each atom – i.e. strength of interaction scales linearly with Z. Neutrons, however, interact with the nucleus of the atom and the intensity of said interaction varies with each isotope, with no relationship between scattering length and Z, as there is found with x-ray diffraction. In the study of $LaTaO_4$ this has been particularly useful as it allows the positions of O^{2-} ions to be defined more accurately than what could be done with x-rays alone.

Approximately 10 g of powdered sample was loaded into a cylindrical vanadium cannister and hermetically sealed before being loaded into the beamline. Time-of-flight (TOF) data was collected using 3 detector banks for detector currents between 40 - 120 μA (approx. 1 – 3hr) at temperatures ranging from 323 – 523 K. Sample temperatures were varied at a rate of 5 K/min and allowed to equilibrate at the target temperature for 15 min prior to data collection.

2.5 Rietveld Refinement of PXRD Data

Rietveld refinement of PXRD data was carried out by General Structure Analysis System (GSAS) software package[1,2] using a previously published crystal structure for $LaTaO_4$[3]. This method of profile fitting compares a calculated diffraction pattern to the collected data for a material and refines the sample and instrument parameters in an iterative process in order to minimise the discrepancies between the two – the end result being a structural model which best represents the samples' structure. Although it is easy for humans to visually evaluate the similarity between the two diffraction patterns, the software itself relies on a numerical evaluation of how well the calculated pattern fit the observed data and represents this with a series of agreement indices.

$$R_{\mathrm{p}} = \frac{\sum |y_{\mathrm{obs}} - y_{\mathrm{calc}}|}{\sum y_{\mathrm{obs}}} \qquad 2.3$$

$$wR_p = \left(\frac{\sum_i w(y_{obs} - y_{calc})^2}{\sum_i (y_{obs})^2} \right)^{1/2} \qquad 2.4$$

Where y_{obs} and y_{calc} are the intensities of the observed and calculated data at a value of x (2θ/TOF/d-spacing). These R_p and wR_p values numerically determine how well the calculated pattern fits the observed data, with the 'weighted R-factor' being particularly useful as it ensures that peaks of all levels of intensity are treated equally and the more intense peaks are not prioritised. With each iteration of the refinement, the software (and user) is adjusting the structural model and associated experimental parameters in order to minimise the value of the R-factors (while maintaining realistic values). These quantifications are also a useful tool for comparing how well different structural models in fit a set of collected data.

A 'goodness-of-fit' parameter, χ^2, can also be used to assess how well the calculated pattern fits the data:

$$\chi^2 = \frac{\sum_i w(y_{\mathrm{obs}} - y_{\mathrm{calc}})^2}{N_{\mathrm{obs}} - N_{\mathrm{ref}} + N_{\mathrm{con}}} \qquad 2.5$$

Where N_{obs} is the number of observations, N_{ref} is the number of refined parameters and N_{con} is the number of system constraints. Improving fits will cause χ^2 to decrease towards an ideal value of 1.

The parameters which were refined in all cases in this investigation were: lattice parameters, atomic positions, thermal displacement parameters, sample displacement parameters, and profile coefficients. A 12-term shifted Chebyshev background function was used to account for background coefficients. The refinement of a modulated structure is somewhat more complicated and requires more parameters to be considered; these are outlined generally in section 2.6.5 and detailed further when the incommensurate structure is explored in chapter 4.

2.6 Characterisation of Modulated Structures

2.6.1 Basic Crystal Structures

A typical crystal structure will have long range periodicity, where an arrangement of atoms will repeat infinitely in 3D space to produce a large macroscopic structure. It is described by the geometric properties of the smallest common arrangement of atoms which repeat periodically. The crystal can then be thought of as a brickwork structure - where each 'brick' (unit cell) is a polyhedral shape that contains this common assembly of atoms and all the symmetry elements present in the crystal. The unit cell can be described by a set of 'basis vectors' (*a*, *b*, *c*) – which describe the length of each cell axis – and the angles between them (α, β, γ). Although, when dealing with 3D+*n* structures, the standard unit axis notation is replaced with (a_1, a_2, a_3, …) for practical purposes, as 4 or more dimensions may need to be considered.

The atom positions (x) within the unit cell are given as a set of fractional coordinates, relative to these basis vectors (x_1, x_2, x_3).

$$\mathrm{x} = x_1 a_1 + x_2 a_2 + x_3 a_3 \qquad 2.6$$

Given that each of the unit cells are related to their neighbours by translational symmetry, the entirety of a periodic crystal can be described by these parameters.

2.6.2 Modulated Structures

In some cases, the translational symmetry which relates these unit cells may be lost and the description of the crystalline structure needs to be modified to account for this change in periodicity. In the simplest case we can imagine a 1D lattice (**figure 2.3(a)**), where points in adjacent cells displace equally in opposing directions (**figure 2.3(b)**). The translational symmetry, which made each of these atomic positions equivalent, has now been lost and the description of its position in the lattice by means of the original basis vectors alone is not sufficient.

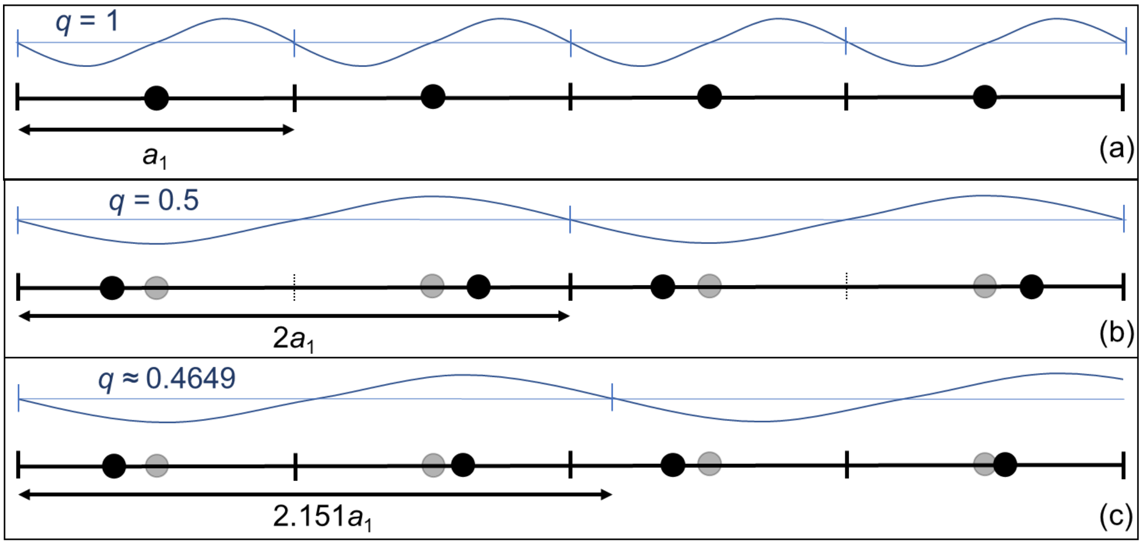

Figure 2.3: 1-Dimensional periodic structures with a repeating distance of: (a) 1 unit cell (b) 2 unit cells (c) 2.151 unit cells. *q* vectors associated with each periodicity are given with respect to reciprocal space. The periodicity of the modulation vector is represented by a sine wave. Solid circles represent the atomic positions in the structure, whereas the transparent circles represent the original atom positions in the unmodulated structure (a).

Of course, the resulting crystal structure could be described by now considering the basis vector of the unit cell to be twice that of the original ($2a_1$) and this could be considered a formation of a 2× supercell – the translational symmetry is still relatively simple and well preserved. However, this description is not always sufficient in explaining structures with more complicated periodicity and expressing the repeating distance using a modulation wavevector may be more appropriate.

The modulation wavevector, q, is a vector which describes the periodicity of the crystal structure. As shown in **figure 2.3**, the wavevector is relative to the reciprocal of the basis vectors (a_1*, a_2*, a_3*) - the unmodulated structure has $q = 1$ and the 2× supercell has $q = 0.5$ ($= 1/2a_1$). These repeating distances in real space are simple integers and are labelled 'commensurately' modulated. Structures that have an irrational repeating distance with respect to the original basis vectors, are said to be incommensurately modulated. As shown in **figure 2.3(c)**, the repeating distance of the atomic displacements is not irrational but also not simply divisible by the original basis vector a_1 - hence a description using a simple supercell is not possible. In this case, with an almost infinite 3D array of unit cells, the arrangement of atoms will eventually repeat and produce an incredibly large supercell – potentially containing millions of atoms. Consideration of such a large cell when characterising a material is not feasible, so it is more appropriate to describe this incommensurate structure considering only the basic unit cell and describe the structural variation between each neighbouring cell in terms of a modulation wave. The term commensurately modulated may be used interchangeably the describe a material which does not have a modulation at all, typically in the context of incommensurate- commensurate transitions, where the modulation wavevector changes from some irrational fraction to 1 (the structure repeats every unit cell), or some other integer in the case of simple supercells.

2.6.3 Diffraction of Modulated Structures

The extra dimensions that are given to a modulated structure are reflected in the diffraction patterns which they produce. As well as the main reflections which are generated by typical periodic crystals, 3D+n structures will produce satellite reflections as a result of their modulation. The position of these satellite peaks in a diffraction pattern is directly related to the q vector. The main Bragg reflections given by the structure maintain the usual indexing notation, but a fourth (or higher) term must also be included to account for the extra dimensionality of these structures. Thus, an *h, k, l* and *m* value must be used for a 3D+1 structure to index each Bragg reflection, *H*, with *m* being the ‘order’ of satellite peak observed:[4]

$$H = ha_1^* + ka_2^* + la_3^* + mq \tag{2.7}$$

In 3D crystals, a single modulation can have up to three non-zero components. Each of these components are a fractional coordinate with respect to the reciprocal basis vectors:

$$q = \sigma_1 a_1^* + \sigma_2 a_2^* + \sigma_3 a_3^* \tag{2.8}$$

It is also possible that a structure has more than one modulation and will hence require more *q* vectors to properly describe it. Each *q* vector required to describe the structure adds an extra ‘dimension’ to the structure - a 3D+1 structure has one modulation wave (or 4 dimensions). **Figure 2.4** shows a diffraction pattern for a 3D+1 crystal, where the modulation has a non-zero component in the a_1* and a_2* axes.

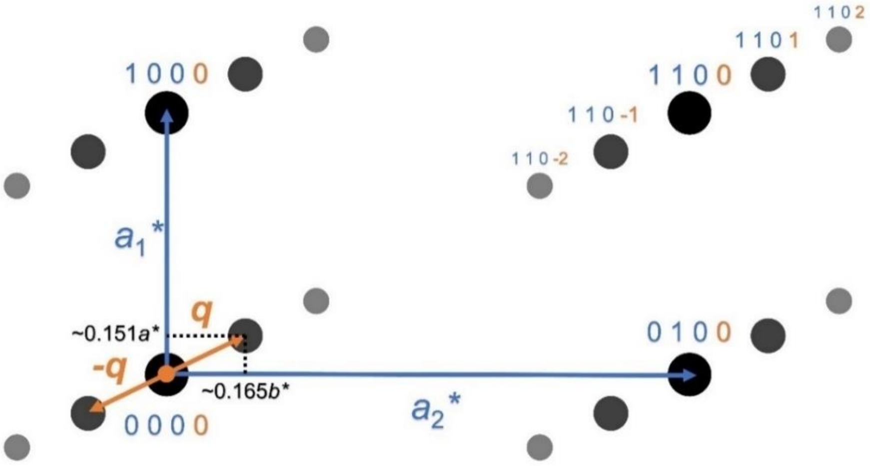

Figure 2.4: Diffraction pattern of a 3D+1 structure. The modulation vector, *q*, has a component in the a_1* and a_2* axes. Main Bragg peaks are 0th order satellite reflections and up to 2nd order satellites are shown.

With diffraction of incommensurate crystals, the satellite reflections would theoretically occupy a dense line of points along the vector *q* due to its irrational components. This, however, is not the case in practice, as the intensity of the satellite reflections are much weaker than the main reflections and decrease in intensity as the satellite order increases. It is found that in most cases Bragg reflections for satellites above 10th order ($m > 10$) are practically undetectable.[4]

Solving a modulated structure from a diffraction pattern is possible without considering satellite reflection and will result in producing a structure which is the average unit cell of the modulated structure. As shown in **figure 2.5**, if a variation in atomic position along the modulated axis is not considered when solving the structure, the atom which is displacing as a function of the modulation will be treated as occupying a single, poorly defined position in the basic unit cell. This will be evident from the refined structure as any atoms which have a modulated position will have unexpectedly large, anisotropic thermal parameters.

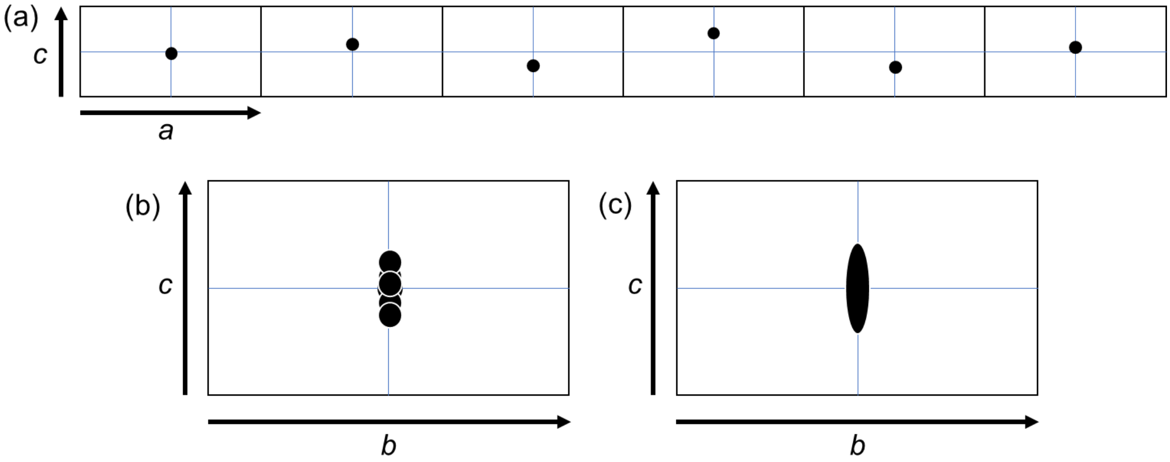

Figure 2.5: Crystal structure with a modulated atomic position along the *a* axis. (a) Viewing the *ac* plane allows the atomic displacement in *c* as the origin of the modulation in *a*. (b) Viewing in the *bc* plane shows the same variation in atomic position along the modulated axis where the resulting electron density is reminiscent of a single, poorly defined atomic position and which can be represented by a large anisotropic thermal parameter (c).

2.6.4 Structural Modulations

Although the periodicity of modulated structures is described by *q*, it does not fully describe how the structure changes as a function of this wavevector. The physical modulation of the crystal structure is described by atomic modulation functions (AMFs). These AMFs are either continuous (harmonic) or discontinuous (sawtooth or crenel functions) and are not limited to expressing the displacement of atomic positions but could also describe the variation of atomic occupancies (the probability that a specific site will be filled by an atom / type of atom) or magnetic moment (direction and magnitude). The displacive modulation described in the examples above are of most interest to this project and hence will be explained more fully.

The AMFs describing the displacement, *D*, of atomic positions as a function of the phase of the wavevector, *q*, are given as a Fourier function:

$$D_N(t) = \sum_{n=1}^{N}(a_n \cos\left(\frac{2\pi}{P}nt\right) + b_n \sin\left(\frac{2\pi}{P}nt\right)) \qquad 2.9$$

Where, a_n and b_n are experimentally determined Fourier coefficients, *n* is the order of the harmonic component and *t* is the phase of the wave over period, *P* (the value of *P* is set as 1 as the phase of the wave is given as $0 < t < 1$). A Fourier function like this will be required to describe the displacement in each physical dimension in the crystal (x_1, x_2, x_3). The atomic positions for a given unit cell are hence given by the positions in the original cell plus the displacement, which is determined by the phase of the modulation wave, *t*, for that unit cell.

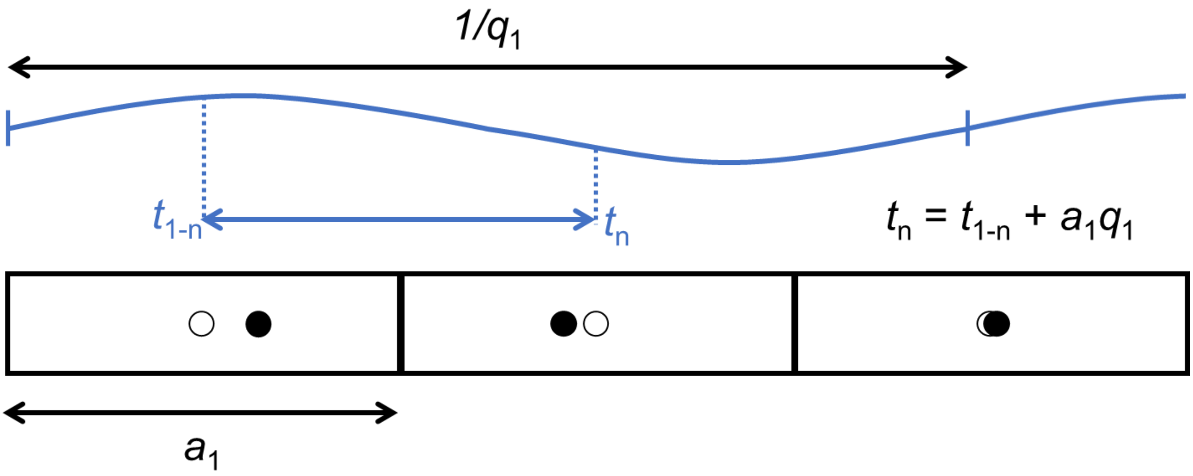

Figure 2.6: 1D modulated structure where $q \approx 0.412a_1^*$. The original atomic positions (open circles) are shown alongside the new positions (filled circles), determined by the AMF.

By definition, for a modulated structure the value of *t* for an atomic displacement will vary between neighbouring cells. The phase of the modulation is a very important component when determining the structure of a given unit cell as it will define the magnitude of the atomic displacement relative to adjacent cells. The phase of the modulation wave for an atom in cell *n* is determined by the phase of the neighbouring cell ($t_{1\text{-}n}$) plus the distance between the original atomic positions in terms of the modulation wave in real space (a_1q_1). The phase of the modulation in a 1D chain (shown in **figure 2.6**) is given by:

$$t_n = t_{n-1} + a_1q_1 \qquad 2.10$$

With the AMF describing the displacement of atoms from their original position in the basic unit cell, the distance between equivalent atoms along the modulated axis is simply given by the basis vector, a_1. The distance between these positions in terms of the modulation vector in real space, $1/q_1$, then determines the phase of the AMF at atomic position n relative to the adjacent atom n-1. Because of the inherent periodicity of the modulation, t_0 (t = 0), can be defined anywhere along the modulated axis, and is not restricted to an atomic position or unit cell edge (as shown in **figure 2.7**).

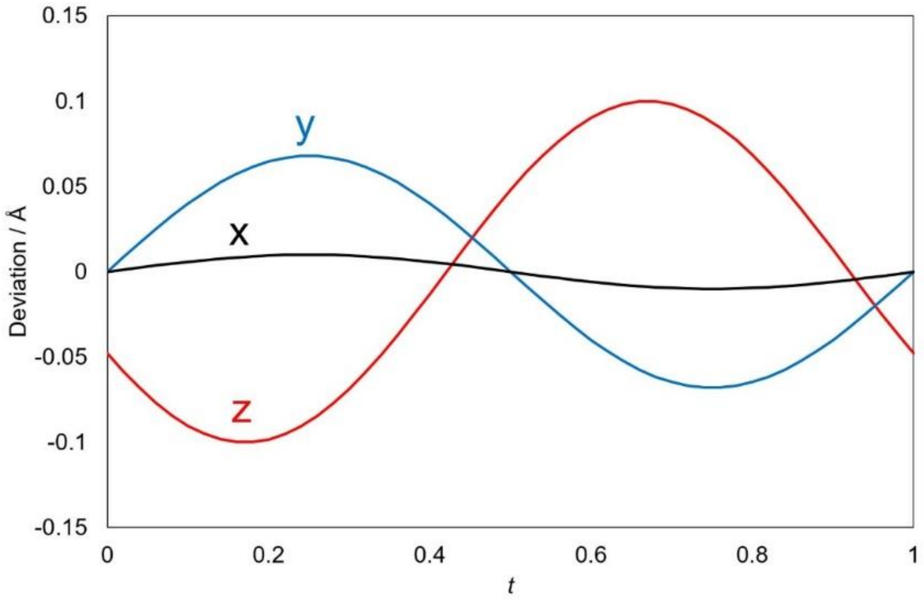

Figure 2.7: Plot of positional deviation of an atom in all three axes as a function of t. The AMF is a simple sinusoidal displacement of the atom from its position in the unmodulated cell.

As the structural variation along the modulation vector is solely reliant on the value of t, structural parameters – such as atomic positions, interatomic distances, and octahedral rotations – are often plotted as a function of t. This allows a clearer understanding of the variation in structure represented by the AMFs and often show patterns which wouldn't necessarily be apparent when looking at the structure in real space.

It is noted that the example given above of simple continuous sinusoidal variation in atomic positions is not the only manner in which modulated structures can arise. Both commensurate and incommensurate systems can be produced from the presence of two separate structural arrangements which can be observed to exist in the same sample.

These structural sub-units may themselves be expansions of a basic cell or be two new symmetrically separate units, but their intergrowth can produce repeating distances which are greater than their individual lattice parameters. These intergrowing phases may be due to simple competing arrangements of atoms in a compound[5] or the mismatch of two (or more) compositionally distinct sublattices.[6]

These sub-units may order coherently to give a commensurate expansion of the basic unit cell[5] or in some cases they may only order partially, which may lead to an observed modulation wavevector which is incommensurate[7,8] *i.e.* the ratio of units present in the crystal is not a simple integer. To elaborate further: the structural units themselves have observable periodicity but the manner in which they are arranged throughout the crystal may not strictly adhere to any particular pattern. There will be a degree of randomness in the way they combine and hence gives a sense of disorder in the system, but this is different from completely chaotic systems where even short range periodicity cannot be identified.

2.6.5 Refinement of 3D+*n* Structures

Rietveld refinement of PND data was carried out by Jana2006 software package[9] – which was utilised due to its ability to consider 3D+*n* structures. Some PND data included satellite peaks associated with a modulated structure that also required the modulation wavevector, q, to be refined as well as the subsequent atomic displacements and thermal displacement parameters associated with the modulation. Only up to 3rd order calculated satellite reflections were considered in the refinements and up to 3rd order harmonic atomic modulation functions (AMFs) were used to describe the structure. Higher order calculated satellite reflections or harmonic waves did not improve the fit by a justifiable amount.

2.7 Electron Microscopy

All selected area electron diffraction (SAED), high resolution transmission electron diffraction (HRTEM) and related analysis were carried out by Dr Shitao Wu and Prof. Wuzong Zu at the University of St. Andrews.

SAED patterns and HRTEM images were recorded using a Gatan 794 CCD camera on a JEOL JEM-2011 electron microscope fitted with a LaB_6 filament operating at an accelerating voltage of 200 kV. For sampling, specimens were ground into powder in acetone with a pestle and mortar. A copper grid coated with a thin holey carbon film was used to support the powder sample.

2.8 Resonant Ultrasound Spectroscopy (RUS)

All resonant ultrasound spectroscopy and related analysis was conducted by Prof. Michael Carpenter at the university of Cambridge.

Polycrystalline pellets of each sample were cut into rectangular parallelepipeds and placed across a pair of corners between the tips of alumina buffer rods inside a horizontal Netzsch furnace. Sample A had dimensions $2.731 \times 1.656 \times 1.215$ mm^3 and a mass 0.0269 g. Sample B had dimensions $2.731 \times 1.965 \times 1.349$ mm^3 and mass 0.0416 g. RUS spectra were collected across a range of 295 – 1141 K with 20 minutes allowed before each reading for sample equilibration. Experimental conditions varied between samples and exact details of each are given in the relevant chapters.

2.9 Raman Spectroscopy

All Raman spectroscopy and related analysis were carried out by Dr Karuna K. Mishra and Prof. Ram S. Katiyar at the University of Puerto Rico.

Raman spectra were measured employing a HORIBA Jobin Yvon micro-Raman spectrometer (model: T64000) equipped with a 50 X long-working distance objective lens. The experiments were carried out in back-scattering geometry (180°) using a 514.5 nm line of an Ar^+ ion laser (Coherent, Innova 70-C). Temperature dependent Raman spectra were recorded from 298 to 583 K in a close temperature interval using a Linkam heating/cooling stage ensuring temperature stability of ± 0.1 K. Signal-to-noise ratio was improvised by adjusting laser power and acquisition time to obtain better Raman spectra. The scattered signals from the sample were analysed using a triple monochromator and detected by a liquid nitrogen cooled CCD detector. The spectrometer resolution for 1800 lines/mm grating was about 1 cm^{-1}. The Raman spectra were analysed using Lorentzian line shapes to obtain the band frequencies, line widths and their intensities.

2.10 Dielectric Spectroscopy

Dense (>70%) cylindrical ceramic samples 0.5 – 1.5 mm thick were prepared for dielectric spectroscopy by polishing the circular faces with fine grit silicon carbide abrasive paper. Silver paste (RS Components) was used to apply electrodes to each of the faces of the pellet using a 0.282 cm^2 circular stencil before being cured at 350 ºC for an hour.

Pellets were placed between two platinum contacts at the end of a custom alumina jig, which allowed the sample to be heated in a Carbolite MTF 10/25/130 tube furnace while capacitance measurements were being made. Measurements of sample capacitance (C_p) and dissipation (D) were taken by a Wayne Kerr 6500B precision impedance analyser as the sample was heated and cooled at a rate of 1 K/min between room temperature and a maximum of 973 K. Data was collected over a frequency range of 25 Hz to 2 MHz with an AC amplitude of 0.1 V.

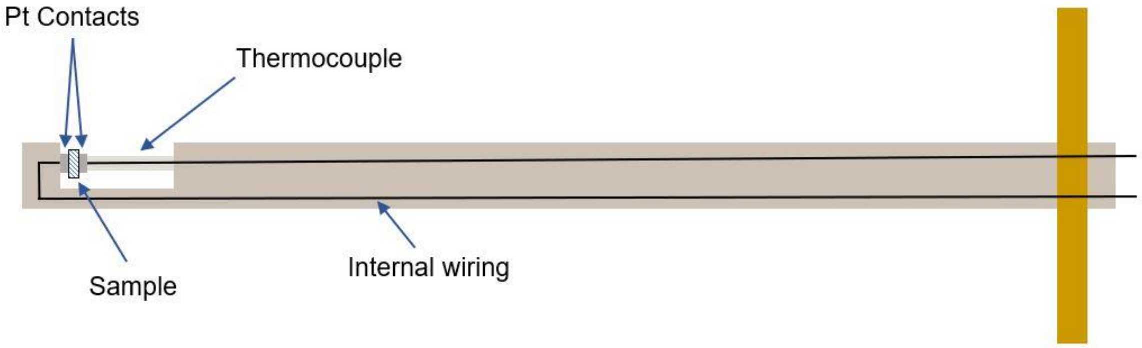

Figure 2.8: Schematic diagram of the jig used to perform dielectric spectroscopy. The jig is inserted into a tube furnace which allows for relative permittivity of the sample to be measured as a function of temperature.

2.11 Bond Valence Sums

Bond valence sums (BVS) are calculations which can be performed, using the observed bond lengths in a crystal (or molecule) to assess the oxidation state or bonding environment of a particular atom. In the context of crystallography, it is common to calculate BVS to establish whether an atom is over- or under-bonded. The overall bond valence of an atom, V, is found using the equation:

$$V = \sum v_i \tag{2.11}$$

Which is a sum of all the individual bond valences, v_i, which are involved in the bonding of that particular atom. These are found from:

$$v_i = \exp\left(\frac{R_0 - R_i}{b}\right) \tag{2.12}$$

where R_i is the observed bond length, R_0 is the ideal bond length and b is a constant (0.37 Å). The ideal bond lengths are tabulated values which have been established by extensive observations and experimentation.[10]

2.12 References

1. Von Dreele, R. B. & Larson, A. C. General Structure Analysis Sytem (GSAS). *Los Alamos Natl. Lab* LAUR, 86–748 (1994).

2. Toby, B. H. EXPGUI , A Graphical User Interface for GSAS. *J. Appl. Crystallogr.* **34**, 210–213 (2001).

3. Cordrey, K. J. *et al.* Structural and Dielectric Studies of the Phase Behaviour of the Topological Ferroelectric $La_{1-x}Nd_xTaO_4$. *Dalt. Trans.* **44**, 10673–10680 (2015).

4. Van Smaalen, S. *Incommensurate Crystallography*. (Oxford University Press, 2007).

5. Bursill, L. A. & Lin, P. J. Incommensurate Superstructures and Phase Transition of Strontium Barium Niobate (SBN). *Acta Crystallogr. Sect. B Struct. Sci.* **43**, 49–56 (1987).

6. Van Smaalen, S., Dinnebier, R., Sofin, M. & Jansen, M. Structures of Incommensurate and Commensurate Composite Crystals Na_xCuO_2 (x = 1.58, 1.6, 1.62). *Acta Crystallogr. Sect. B Struct. Sci.* **63**, 17–25 (2007).

7. Zhou, W., Jefferson, D. A. & Thomas, J. M. Defect Fluorite Structures Containing Bi_2O_3 : The System Bi_2O_3 -Nb_2O_5 . *Proc. R. Soc. London. A. Math. Phys. Sci.* **406**, 173–182 (1986).

8. Zhou, W. Microstructures of Some Bi-W-Nb-O phases. *J. Solid State Chem.* **163**, 479–483 (2002).

9. Petříček, V., Dušek, M. & Palatinus, L. Crystallographic Computing System JANA2006: General features. *Zeitschrift für Krist. - Cryst. Mater.* **229**, (2014).

10. Brown ID. The Chemical Bond in Inorganic Chemistry: The Bond Valence Model (Oxford University Press; 2006).

3 Chapter 3: Structural Phase Transitions in $LaTaO_4$

3.1 Introduction

The following chapter explores the successive phase transitions of $LaTaO_4$ as a function of temperature. As discussed in chapter 1 the basic structural properties of this material have been well established[1–5] but the correct sequence of phase transitions has been so far elusive. The previously accepted sequence of phase transitions from the parent orthorhombic *Cmcm* phase on cooling is as follows:

$$Cmcm \text{ (orthorhombic)} \leftrightarrow Cmc2_1 \text{ (orthorhombic)} \leftrightarrow P2_1/c \text{ (monoclinic)}$$

Dielectric spectroscopy is a particularly useful tool in indicating the temperatures at which structural transitions occur, with two previous studies using this technique to identify the monoclinic – orthorhombic transition ($T_{\text{m-o}} \approx 440$ K).[4,5] Dielectric anomalies are typically indicative of structural transitions and the data presented in these studies also revealed a second anomaly which occurred at a higher temperature but could not be attributed to any known structural transition. Cordrey *et al.* suggested this may indicate a transition to a structure containing short range anti-ferroelectric ordering with an associated incommensurate modulation, similar to $BaMgF_4$.[4,6] Abreu *et al.* presented it as evidence of a transition to the parent *Cmcm* phase.[5]

In this chapter, evidence is presented which identifies an intermediate incommensurate $Cmc2_1$ (orthorhombic) phase that exists between the high temperature basic $Cmc2_1$ structure and the low temperature $P2_1/c$ (monoclinic) phase. The structural details of the incommensurate phase are discussed in depth in chapter 4; here however, various complimentary techniques are used to fully analyse the phase transition sequence in light of this new intermediate incommensurate phase. PND, RUS and Raman data are consistent in indicating a structural transition between the incommensurate and commensurate $Cmc2_1$ phases which coincides with the second dielectric anomaly. The new transition sequence on heating involves a transition between the monoclinic and incommensurate orthorhombic phase ($T_{\text{m-o}}$) then an incommensurate - commensurate transition ($T_{\text{IC-C}}$) between two orthorhombic $Cmc2_1$ phases. The transition to the *Cmcm* phase is not observed in this study.

3.2 Experimental

Polycrystalline ceramic samples of $LaTaO_4$ stable as either orthorhombic or monoclinic phase at room temperature were synthesized using the standard solid-state method outlined in chapter 2. These are hereafter denoted as o-$LaTaO_4$ and m-$LaTaO_4$, respectively, despite the fact that m-$LaTaO_4$ will transform to the orthorhombic phase on heating. Both sample types produced were not single phase but consisted of mixtures of the monoclinic and orthorhombic polymorphs. Pellets loosely pressed uniaxially and annealed at 1350 °C were mostly orthorhombic phase under ambient conditions but with < 6 wt% monoclinic phase. Pellets which were pressed at ~207 MPa and annealed at 1650 °C were mostly monoclinic under ambient conditions but could contain up to 10 wt% orthorhombic phase.

PXRD and PND data were collected as outlined in chapter 2 and analysed using GSAS Rietveld refinement software. Rietveld refinement of the x-ray data was sufficient in describing the lattice parameters of the phases, but the exact volume fractions of the phases present was not well defined – only later when performing Rietveld refinement of the PND data could accurate phase fractions be determined. Consideration of the modulation in the incommensurate orthorhombic phase was not possible using GSAS software and so the refinement of PXRD and PND data using GSAS was carried out only considering the 'basic' unmodulated unit cell.

3.3 Results

3.3.1 Room Temperature PXRD Data

Initial attempts at synthesizing o-$LaTaO_4$ were mostly single phase but inspection of room temperature diffraction patterns showed clear additional peaks which could all be attributed to m-$LaTaO_4$. Heating the reaction mixture at 1350 °C produced the smallest amount of monoclinic phase while also ensuring the reaction went to completion – eliminating any trace of starting materials in the final product without the need for successive heating cycles.[2]

The PXRD data for the o-$LaTaO_4$ sample was fitted to both the orthorhombic $Cmc2_1$ and monoclinic $P2_1/c$ phases in a two-phase Rietveld refinement. The fit of the data is shown in **figure 3.1**. Structural parameters, cell dimensions and atom positions for both phases are in good agreement with previously published models, **table 3.1**, and provide an acceptable fit of wRp = 15.50% - without the need to consider additional phases (such as starting materials) or superstructures. Although the additional peaks produced by the minor phase seem insignificant on visual inspection, refinement of the phase fractions indicate <2% monoclinic phase. It was later discovered that the room temperature orthorhombic phase is incommensurately modulated but no obvious additional satellites generated from a superstructure or additional periodicity can be observed here. This is likely due to the relative insensitivity of x-ray methods compared to electron microscopy and neutron diffraction where the satellite reflections are readily identified.

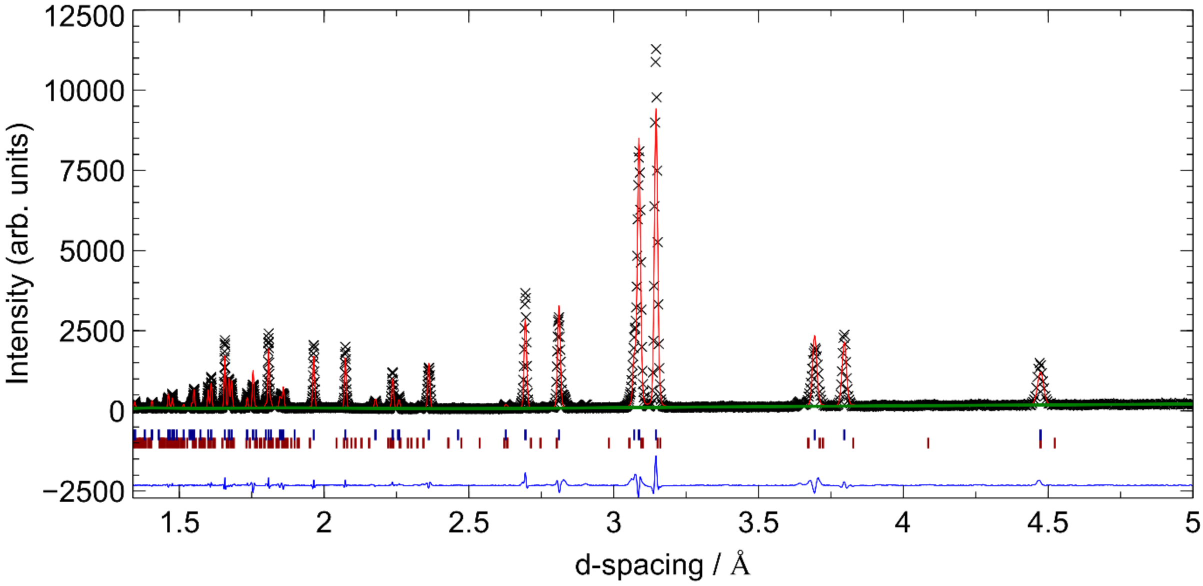

Figure 3.1: Two phase Rietveld refinement of room temperature PXRD data for a sample of o-$LaTaO_4$. Refinement of phase fractions indicates <2 wt% monoclinic phase. Figure key: observed data (black crosses), calculated (red line), background (green line), orthorhombic / monoclinic reflection positions (dark blue - top / dark red - bottom, respectively) and difference plot (blue line).

Table 3.1: Published lattice parameters for $LaTaO_4$. Data published with no specified temperature are assumed to be collected under ambient conditions. Vullum states that their data was collected above $T_{m\text{-}o}$ but no specific temperature was given. Esds included where available.

Author	Phase	T / K	a / Å	b / Å	c / Å	β	Ref.
Cava	$Cmc2_1$	573	3.9457(1)	14.6411(1)	5.6643(7)	90.00	1
Vullum	$Cmc2_1$	$>T_{m\text{-}o}$	3.9404(41)	14.7190(51)	5.6415(82)	90.00	2
	$P2_1/c$	*Room T.*	7.6281(81)	5.5781(02)	7.8203(71)	101.53(80)	
Siqueira	$P2_1/c$	*Room T.*	7.7008	5.5606	8.1220	103.66	3
Cordrey	$Cmc2_1$	373	3.9400	14.7000	5.6000	90.00	4
Abreu	$P2_1/c$	*Room T.*	7.7010	5.5610	8.1220	103.70	5
Howieson	$Cmc2_1$	323	3.9330(1)	14.8051(2)	5.6217(1)	90.00	n/a
	$P2_1/c$	323	7.6329(1)	5.5821(1)	7.8258(1)	101.551(1)	

Increasing annealing temperatures was found to favour the formation of monoclinic $LaTaO_4$ and led to the exploration of harsher synthesis conditions in order to form a sample of m-$LaTaO_4$ stable at room temperature. A previous investigation of $LaTaO_4$ achieved predominantly monoclinic phase at room temperature by doping with 10% Nd^{3+} at the A-site.[4] In another study, Vullum *et al*. noted the tendency for $LaTaO_4$ samples to form the orthorhombic phase when sintered as a loose powder, and to favour the monoclinic phase when sintered as a pressed pellet. Obtaining monoclinic $LaTaO_4$ at room temperature is achievable by applying a pressure of 300 – 400 MPa – application of large pressures favours the monoclinic phase in accordance with the Clausius-Clapeyron equation.[2]

In this study, it was found that applying large isostatic pressure (~207 MPa) to pellets of starting materials prior to reaction at higher temperatures (1650 °C) produced a predominantly monoclinic phase. It is believed that the higher annealing temperature and much larger force applied when pressing pellets, result in internal stresses within the sample of $LaTaO_4$ which act in a similar way to that of the external pressure applied by Vullum *et al.* post-synthesis.[2]

Figure 3.2 shows the Rietveld refinement of the m-LaTaO4 sample. Refinement of the phase volumes show < 2% orthorhombic phase – indicating a somewhat successful method for producing m-LaTaO4 samples which are stable under ambient conditions. Heating for longer periods of time (~14 hr) at similar temperatures did not yield single phase monoclinic LaTaO4 as reported by Siqueira *et al.*[3], and it was found that the isostatic pressure was an essential part of reducing the phase volume of orthorhombic phase.

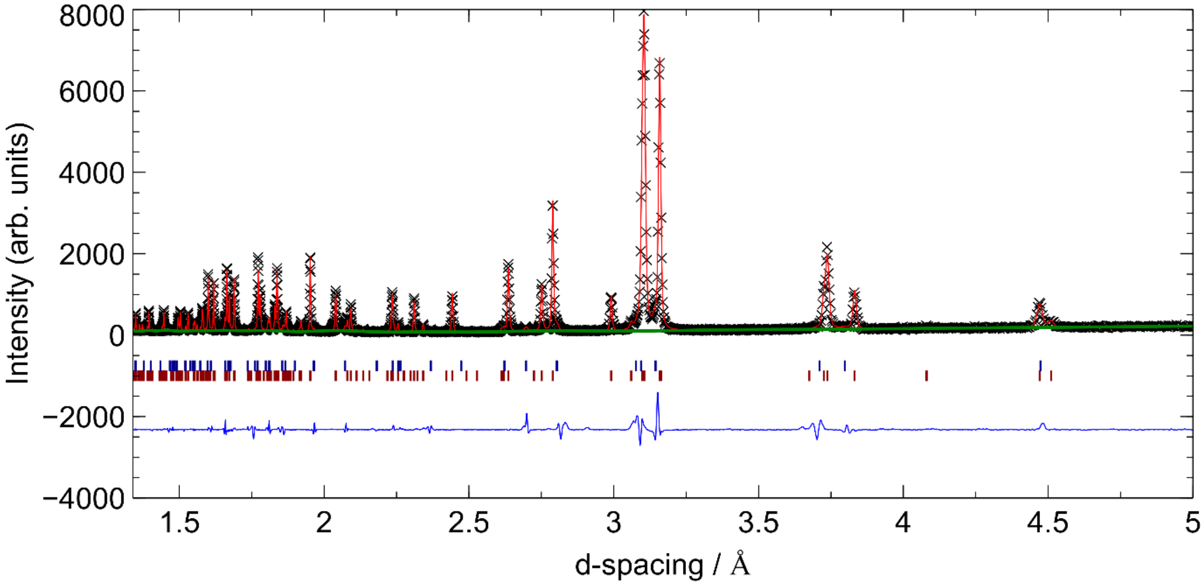

Figure 3.2: Two phase Rietveld refinement of room temperature PXRD data for a sample of m-LaTaO4. Refinement of phase fractions indicates < 5 wt% orthorhombic phase. Figure key: observed data (black crosses), calculated (red line), background (green line), orthorhombic / monoclinic reflection positions (dark blue - top / dark red - bottom, respectively) and difference plot (blue line).

3.3.2 Dielectric Spectroscopy

It has been well established from previous studies that monoclinic $LaTaO_4$ will transform into the orthorhombic phase on heating[1–5], with dielectric spectroscopy being a particularly useful tool in indicating the temperature at which this phase transition occurs. Dielectric spectroscopic data from two of these studies[4,5] have been particularly important in identifying a discrepancy between the proposed transition sequence and the observed behaviour of the material. Previously published structural and dielectric data is consistent for the monoclinic - orthorhombic transition, however, the origin of a second dielectric anomaly occurring at ~480 K had so far only been speculated on[4] or incorrectly attributed to transformation from the $Cmc2_1$ phase to the parent $Cmcm$ phase - with no structural data to support this hypothesis (Abreu *et al.* present Raman data at this transition which they believed supported this conclusion)[5]. Dielectric data is presented below which is consistent with the newly proposed transition sequence, where the dielectric anomaly is attributed to an incommensurate – commensurate transition.

Capacitance and dissipation (tan δ) measurements were carried out between 300 and 550 K in order to identify the temperature of the monoclinic – orthorhombic transition ($T_{\text{m-o}}$) and the newly identified orthorhombic incommensurate – commensurate transition ($T_{\text{IC-C}}$). The o-$LaTaO_4$ sample shows a broad dielectric anomaly at 490 K and 485 K on heating and cooling, respectively (**figure 3.3**) which coincides with the incommensurate – commensurate transition at $T_{\text{IC-C}}$. This transition shows no significant temperature hysteresis and the small effect which is observed is likely extrinsic and caused by 'thermal lag' in the measurement equipment. The dielectric anomaly associated with the monoclinic – orthorhombic transition ($T_{\text{m-o}}$) is obviously missing from this plot, but this feature will appear on further cooling to just below 300 K. **Figure 3.4** shows the relative permittivity of m-$LaTaO_4$ as a function of temperature. As this sample is mostly monoclinic at room temperature, it undergoes a transition to the incommensurate orthorhombic phase at $T_{\text{m-o}} \approx 440$ K on heating. There is a fairly large thermal hysteresis associated with this transition (~140 K), with the sample returning back to the monoclinic phase just below 300 K. The broad dielectric peak at ~500/495 K is similar to o-$LaTaO_4$ and is attributed to $T_{\text{IC-C}}$. There is a prominent feature in the dissipation, tan δ, which coincides with this transition, which is not present for o-$LaTaO_4$. The reason for this is unclear.

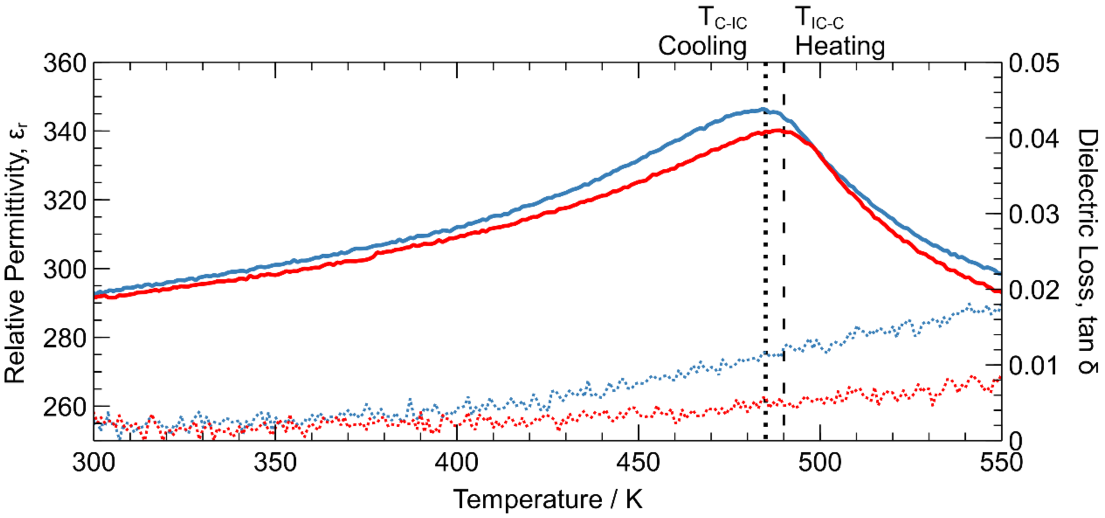

Figure 3.3: Plot of relative permittivity (ε_r) and dielectric loss (tan δ) as a function of temperature for o-LaTaO$_4$. Data was collected on heating (red) and cooling (blue). The broad dielectric peak at ~490 K (heating)/485 K (cooling) is attributed to a transition between a modulated and unmodulated *Cmc*2$_1$ phase (indicated by dashed line for heating and dotted line for cooling). Presented data is at 400 kHz

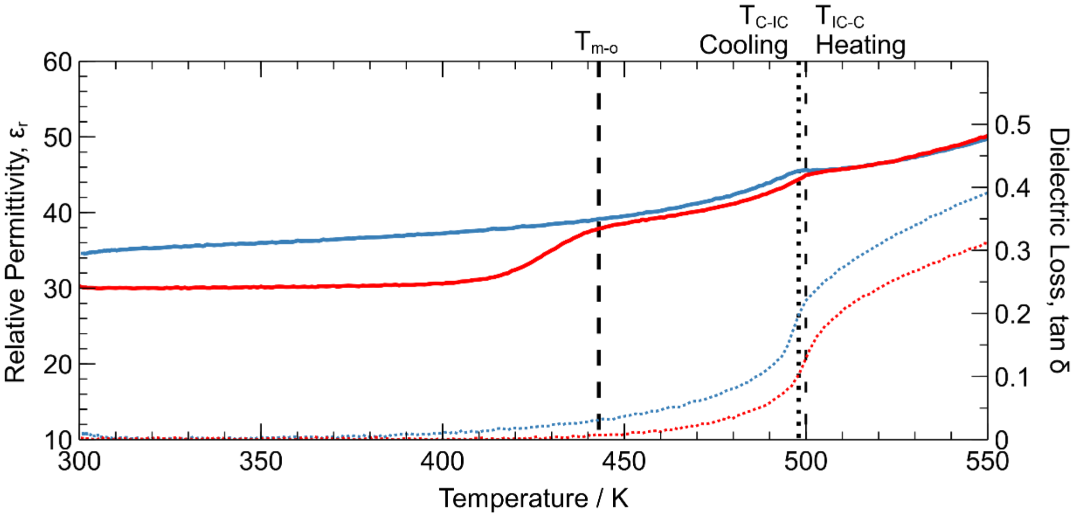

Figure 3.4: Plot of relative permittivity (ε_r) and dielectric loss (tan δ) as a function of temperature for m-LaTaO$_4$. Data was collected on heating (red) and cooling (blue). The peak in permittivity at ~440 K is a transition between the monoclinic phase and the modulated orthorhombic phase on heating (indicated by the dashed line). Presented data is at 400 kHz

Comparison with the dielectric spectroscopy conducted by Abreu *et al.* show that the data for m-$LaTaO_4$ is almost superimposable with that presented here, with $T_{m\text{-}o} \approx 440$ K and $T_{IC\text{-}C} \approx 500$ K.[5] However, it is also noted both that these datasets show a much lower temperature for the dielectric anomalies (and associated phase transitions) when compared to the monoclinic samples stabilised by Nd^{3+} doping in the study by Cordrey *et al*.[4] This is likely to be a direct result of chemical pressure arising from the smaller Nd^{3+} cation occupying the A-site and this is discussed further in chapter 5.

3.3.3 Variable Temperature PXRD Data

Variable temperature (VT) PXRD was collected across the temperature range 303 to 573 K on heating and cooling for a sample of m-$LaTaO_4$ (<2 wt% orthorhombic phase). This allowed the structural changes associated with all phase transitions to be observed. For ease of comparison, the lattice parameters of the monoclinic phase are transformed into that of a pseudo-orthorhombic cell, as detailed in **Appendix B**.

The monoclinic – orthorhombic transition is easily distinguished from visual inspection of the diffraction data, where patterns collected below 453 K on heating are readily fitted by the $P2_1/c$ phase (wRp < 9%). Diffraction data collected at room temperature on cooling are also fitted by this phase and indicates a return to the monoclinic phase with a large thermal hysteresis of ~140 K, consistent with the dielectric data. Diffraction patterns collected in the range of 453 – 573 K on heating and 573 – 333 K on cooling are fitted by the $Cmc2_1$ phase. The ability to fit the diffraction data collected above the transition at 503 K by the $Cmc2_1$ model is contrary to the conclusion of Abreu *et al.*[5], where they use Raman spectroscopy data to suggest this is a transition to the aristotype *Cmcm* phase. Attempts to fit the diffraction data collected above 503 K to the *Cmcm* were unsuccessful and provided a similarly poor fit as that reported by Cordrey *et al.*[4] Although the structure maintains the $Cmc2_1$ symmetry above ~503 K there is a clear step change in lattice parameters which coincides with the broad dielectric anomaly observed in all studies (**figure 3.5**).

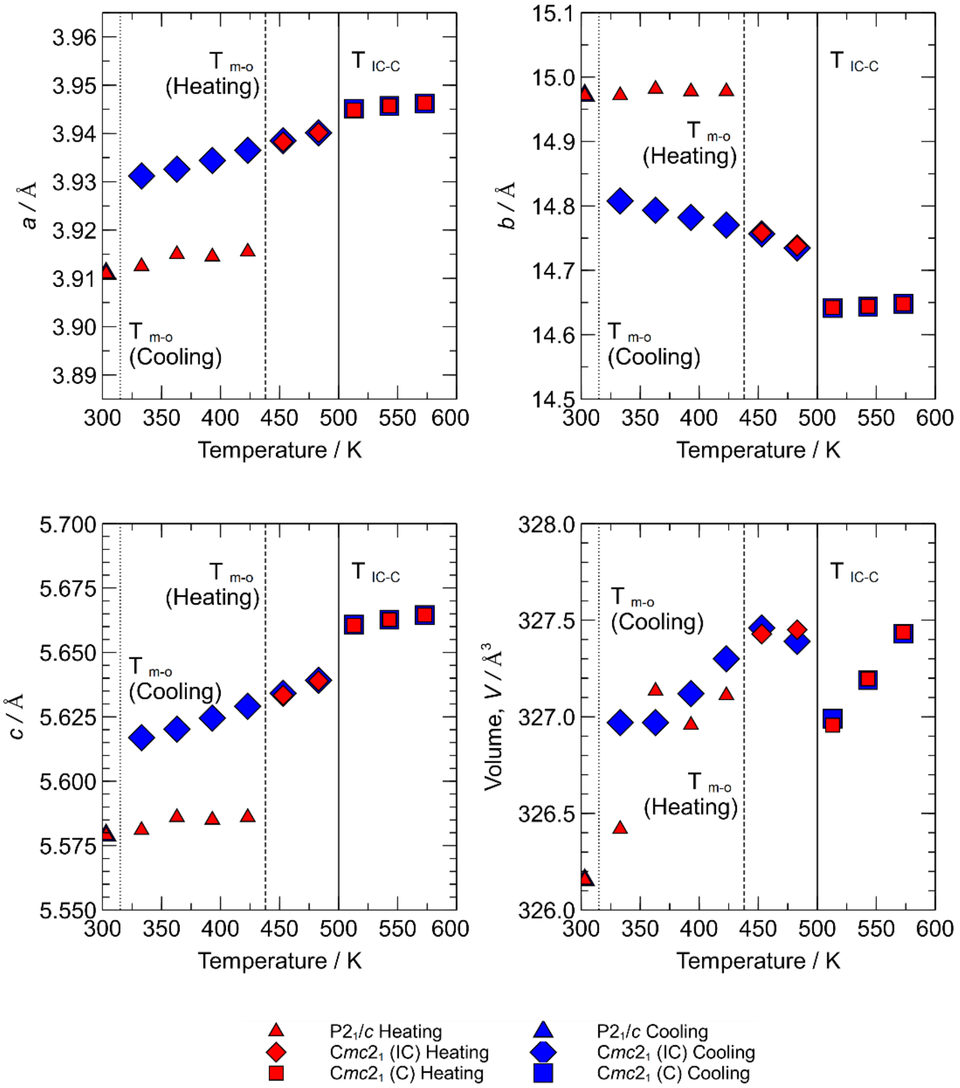

Figure 3.5: Lattice parameters of m-$LaTaO_4$ as a function of temperature. $P2_1/c$ parameters are recalculated to that of a pseudo-orthorhombic setting for comparative purposes. Transitions between the monoclinic and modulated (IC) orthorhombic phase are denoted by $T_{m\text{-}o}$, for heating (dashed line) and cooling (dotted line). The transition between the incommensurate $Cmc2_1$ and commensurate (basic) $Cmc2_1$ structure is denoted by $T_{(IC\text{-}C)}$ (solid line).

To further elucidate the nature of the transition, a second VT-PXRD experiment was conducted over the temperature range of the second dielectric anomaly. Diffraction data were collected at 2 K increments on heating and cooling. All diffraction patterns were fitted in the $Cmc2_1$ space group and plotting each parameter as a function of temperature shows a sharp but continuous change in parameters, suggestive of a 2nd order structural transition (**figure 3.6**).

The *a* and *c* parameters have noticeably similar trends across this transition. This is unsurprising due to the interconnectivity of the octahedra which form 'sheets' in the *a*-*c* plane. Negative thermal expansion is observed in the *b* axis, which shows the largest change in magnitude (~0.1 Å) across the transition. This is not an unusual feature for layered perovskites and is again related to the 2D connectivity of the octahedra.[7]

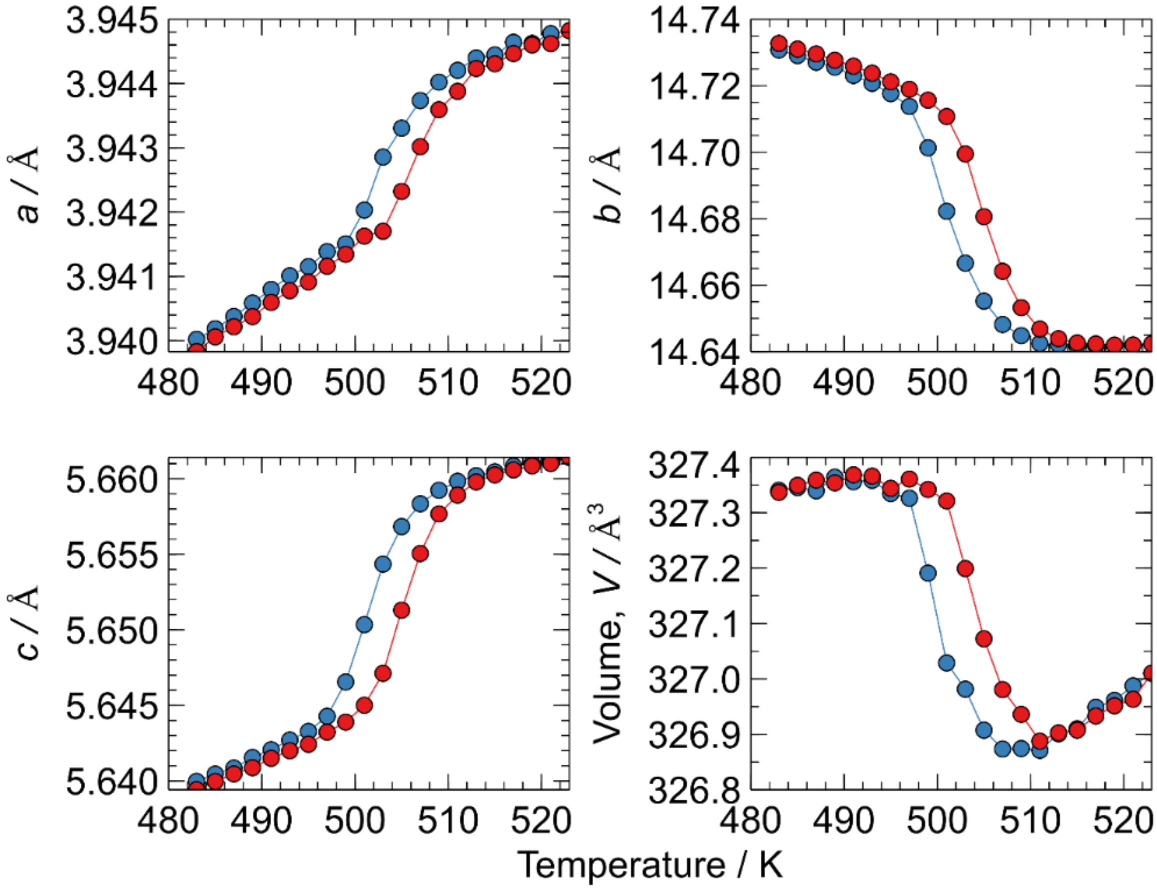

Figure 3.6: Lattice parameters for (an initially) m-$LaTaO_4$ sample as a function of temperature on heating (red) and cooling (blue). A single $Cmc2_1$ phase is used to fit the diffraction data and the seemingly continuous nature of the changing lattice parameters is suggestive of a 2nd order transition.

3.3.4 Neutron Diffraction Experiment

The VT-PXRD data collected was sufficient to allow the transition at 500 K to be identified as a transition between two similar $Cmc2_1$ phases and showed that there is a clear change in lattice parameters across the transition temperature range. The mechanism which drives this change in lattice parameters was still unclear and more accurate structural characterisation would be required. It is already reported that the thermal expansion of Carpy-Galy phases is closely related to the octahedral rotations within the structure[7] and hence neutron diffraction would be an incredibly useful tool in determining the nature of this transition. **Figure 3.7** shows the neutron diffraction pattern for o-$LaTaO_4$ at 323 K (on heating) across two detector banks. A two-phase Rietveld refinement of data collected at 323 K on heating revealed there was ~ 5 wt% monoclinic phase in the sample – slightly higher than that found from x-ray data. Initial fitting of this data was carried out using a basic $Cmc2_1$ structure which accounted for the vast majority of reflections observed with an *wRp* value of 3.96%. Visual inspection of the refined pattern shows some clear additional peaks (at *ca*. 2.45 and 2.5 Å) which could not be accounted for by the basic orthorhombic or monoclinic structures (these are shown in more detail in **figures 3.9 and 3.10**).

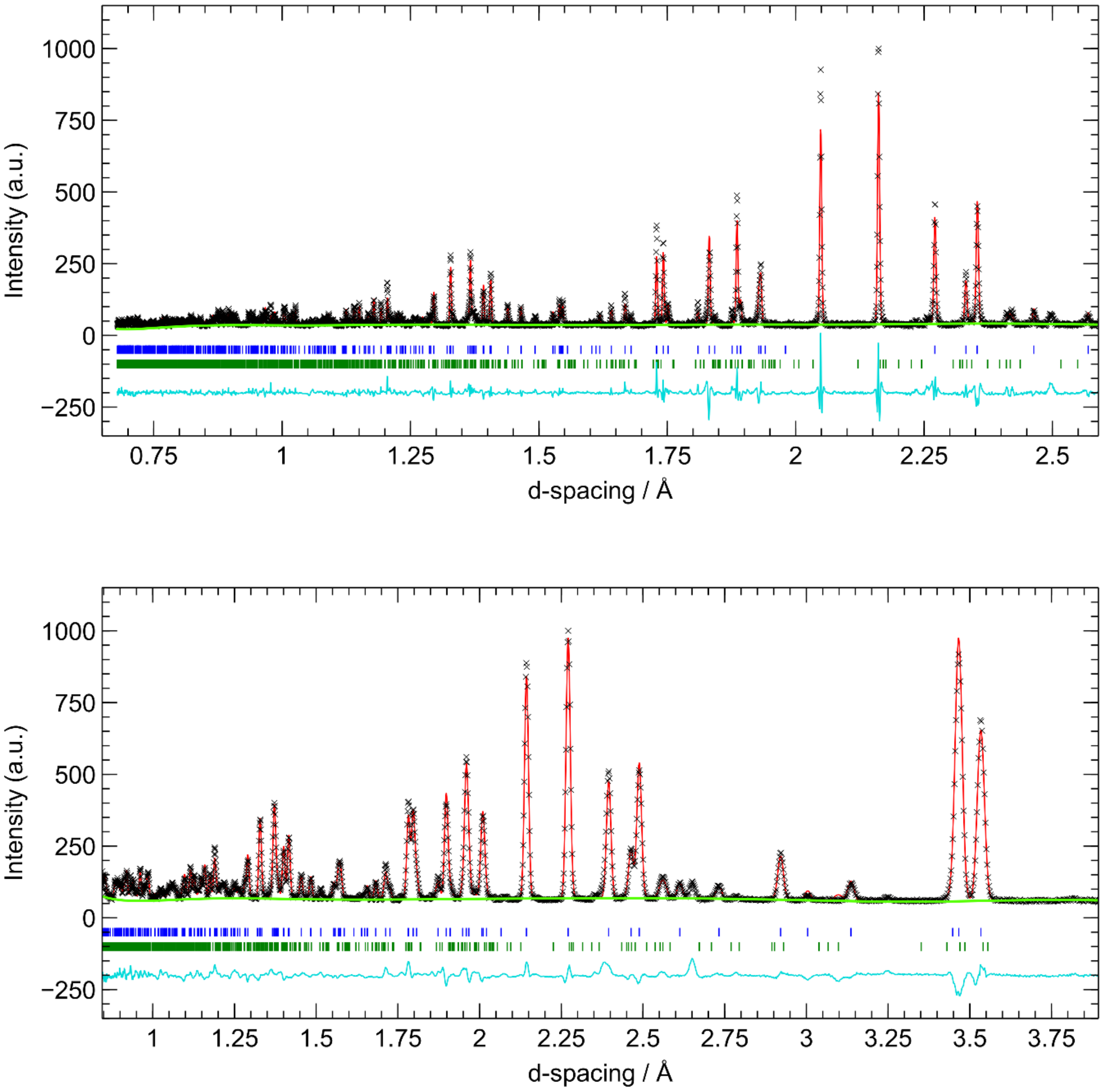

Figure 3.7: HRPD detector bank 1 (top) and bank 2 (bottom) neutron diffraction pattern for o-$LaTaO_4$ at 323K (collected on heating). The data is fitted using basic $Cmc2_1$ and $P2_1/c$ models and shows ~5 wt% monoclinic phase. Figure key: observed data (black crosses), calculated (red line), background (green line), orthorhombic / monoclinic reflection positions (dark blue / dark green, respectively) and difference plot (blue line).

In conjunction with this experiment, electron microscopy was performed on o-$LaTaO_4$ at room temperature which revealed a series of satellite reflections along the *a* axis of the orthorhombic cell (see chapter 4). This strongly suggested that the structure below the observed transition contained some long-range periodicity beyond that of the simple $Cmc2_1$ unit cell. The peaks which are unaccounted for in **figure 3.7** were therefore likely also to be generated from a $Cmc2_1$ superstructure. This is discussed in detail in chapter 4, where the (incommensurately) modulated structure is fully described.

PND data for m-$LaTaO_4$ samples were also collected at 323 K and are shown in **figure 3.8**. In comparison to the o-$LaTaO_4$ sample, PND revealed that the orthorhombic phase present was much smaller (~1 wt%) than estimated from the PXRD data. No additional reflections which could not be accounted for by the basic $P2_1/c$ model were observed, suggesting no modulation/supercell is present in the monoclinic phase.

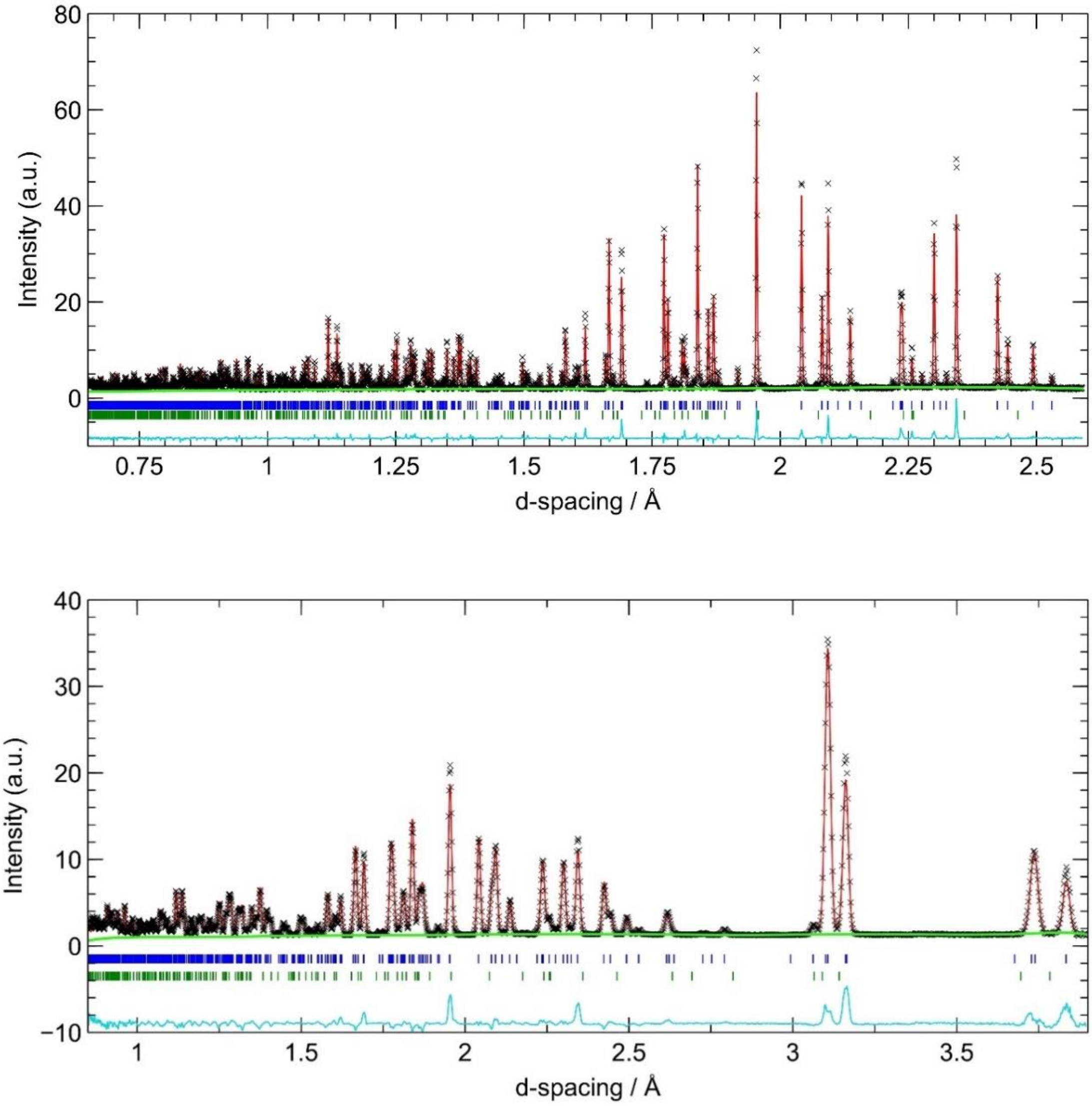

Figure 3.8: HRPD detector bank 1 (top) and bank 2 (bottom) neutron diffraction pattern for m-LaTaO4 at 323K (collected on heating). Observed data is fitted using basic $P2_1/c$ and $Cmc2_1$ models, as satellite reflections are not observed. Figure key: observed data (black crosses), calculated (red line), background (green line), monoclinic / orthorhombic reflection positions (dark blue / dark green, respectively) and difference plot (blue line).

Identification of the satellite reflections in the PND data was not only incredibly useful in deciphering the modulation in the structure, but also allowed the nature of the previously unidentified transition to be revealed. The exact details of the of the modulated phase are not necessary for the purpose of the analysis presented here, but it can be concluded from the neutron data that the observed transition is between a modulated and unmodulated structure – the modulation is later revealed to be incommensurate (Chapter 4) and hence the transition is hereafter labelled an incommensurate – commensurate transition ($T_{\text{IC-C}}$). The phases above and below the transition are then simply labelled $Cmc2_1$ (C) and $Cmc2_1$ (IC), respectively, for the following analysis.

Figure 3.9 shows PND patterns for o-$LaTaO_4$ obtained on heating through the IC-C transition. The diffraction patterns collected above and below the transition (523 and 483 K, respectively) can each be fitted to a $Cmc2_1$ model, but with different cell parameters, with all the main Bragg reflections are accounted for. Diffraction data collected close to the midpoint of the transition contained approximately double the expected number of Bragg reflections. The duplicate peaks present approximately coincided with the reflections found in the data at either side of the transition. These main peaks (indicated by dashed lines) clearly show a transition between two $Cmc2_1$ phases with different cell parameters, with coexistence of both in the intermediate temperature data set obtained at 503 K. In addition, the satellite reflections which are attributed to the modulated structure (~ 2.32-2.33 and ~2.41 Å – discussed in chapter 4) are prevalent before the transition (483 K), only somewhat visible at the midpoint (503 K) and completely disappear after the transition (523 K). The disappearance of the satellite reflections shows the lack of additional periodicity in the high temperature $Cmc2_1$ (C) phase and all reflections generated by this phase can be accounted for by a simple (commensurate) $Cmc2_1$ unit cell. The low temperature data, with superlattice reflections present, is associated with the incommensurate $Cmc2_1$ (IC) phase. The phase coexistence of $Cmc2_1$ (IC) and $Cmc2_1$ (C) structures and abrupt change in peak positions above and below the transition suggest the IC-C transition is 1st order in nature. This is in direct contrast to the conclusion drawn from analysis of the PXRD data, where the change in reflection position - and hence the lattice parameters – appeared to shift continuously.

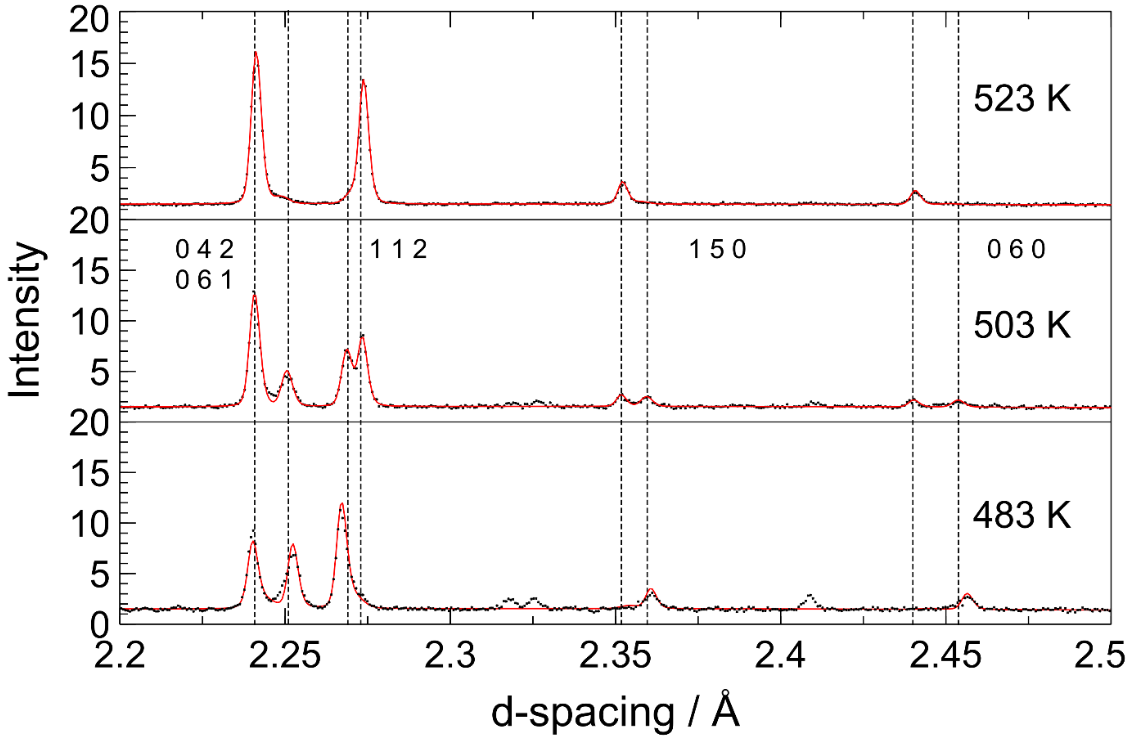

Figure 3.9: HRPD detector bank 1 neutron diffraction pattern at the incommensurate-commensurate transition. The pattern at 523 K is fitted by a commensurate *Cmc*2_1 phase, whereas the pattern below the transition at 483 K is only fully fitted by an incommensurate *Cmc*2_1 structure as described in chapter 4. The pattern at 503 K is at approximately the midpoint of the transition with peaks from both phases present in an approximate 1:1 ratio. Dashed lines are added at peak positions in the 503 K pattern to guide the eye.

The progression of the IC-C transition was closely monitored, with PND data collected every 2 K on cooling across the temperature range at which the transition occurred (established from PXRD data). A contour plot, **figure 3.10**, shows a more detailed view of the position and intensity of the reflections shown in **figure 3.9** as a function of temperature. This ‘heat map’ shows the position of each diffraction peak from 523 to 483 K in 2 K increments, with the intensity of each peak being illustrated by a colour scale. This further illustrates the 1st order nature of the IC-C transition as there is a clear discontinuity in the peak positions as temperature decreases. The presence of peaks from both phases at temperatures close to the midpoint of the IC-C transition demonstrate phase coexistence in this temperature range consistent with a 1st order phase transition.

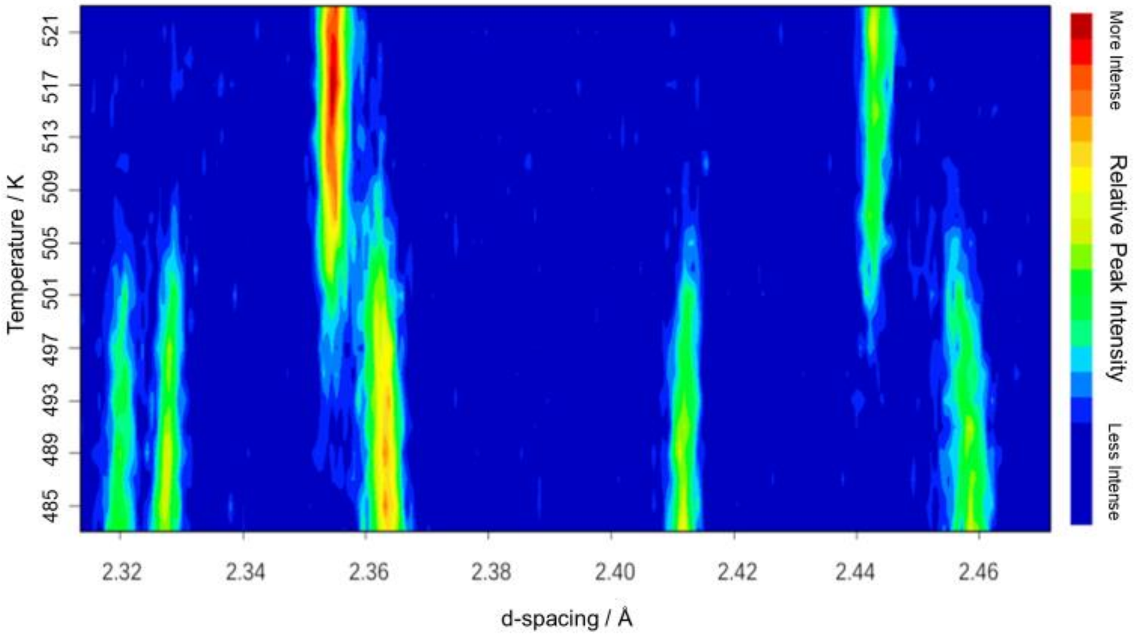

Figure 3.10: Contour plot of bank 1 PND data in the range ~ 2.31 to 2.47 Å collected on cooling through the C to IC transition. The data show a discontinuity of the position of the main peaks at ~2.35-2.36 and 2.44-2,46 Å together with a region of coexistence suggesting a first order transition. In addition, the appearance of additional reflections at ca. 2.32, 2.33 and 2.41 on cooling indicate the low temperature phase has an additional $Cmc2_1$ superstructure associated with a modulation.

Two phase refinements on the PND data collected during the transition using two basic (commensurate) $Cmc2_1$ models allowed the volume fractions of the high and low temperature phases to be estimated as the transition progressed. The resulting phase fractions are plotted as a function of temperature in **figure 3.11**. The data show a continuous variation in phase fraction consistent with a first order transformation. As only basic $Cmc2_1$ models were used, the goodness-of-fit (χ^2) improves with increasing temperature as the IC phase and the associated satellite reflections (which are not fitted) disappear.

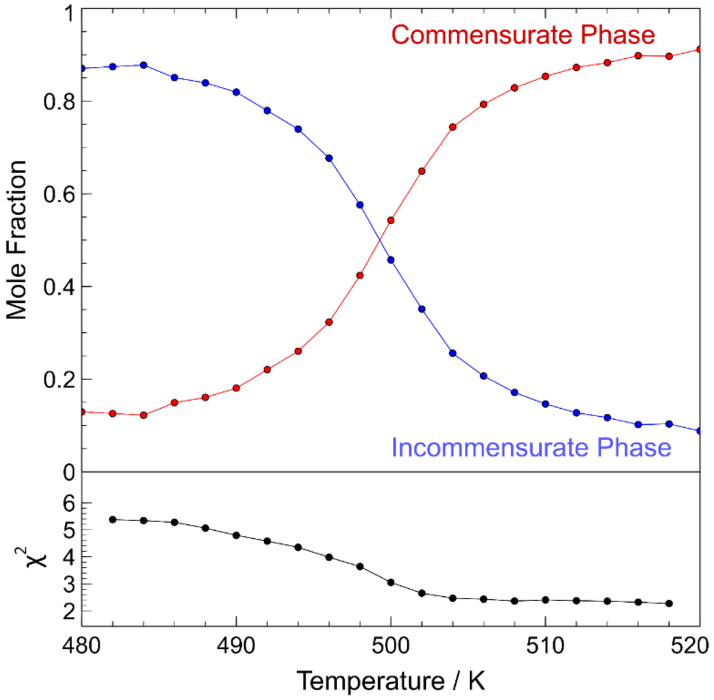

Figure 3.11: Plot of mole fraction of each orthorhombic phase and goodness-of-fit, χ^2, across the IC-C transition. Data were fitted to two basic (commensurate) $Cmc2_1$ models, one for each of the high and low temperature phases. The low temperature incommensurate phase becomes more prominent as temperature decreases. This is evident in the deterioration in the goodness-of-fit as only the average unit cell has been fitted and satellite reflections have not been considered. χ^2 values for 483 and 523 K have been omitted as these data were collected for three times the duration than other temperatures.

As mentioned previously, a more detailed analysis of the structural change and variation in lattice parameters during this transition is presented in Chapter 4 where determination of the nature of the IC phase allows full refinement of the data to include the superlattice reflections. For the purposes of this chapter which re-evaluates the phase transition sequence, analysis using a basic (unmodulated, commensurate) $Cmc2_1$ model for the IC phase is sufficient.

3.3.5 Re-examination of Variable Temperature X-Ray Diffraction

With the IC-C transition identified as 1st order based on analysis of the PND data, the x-ray diffraction data was re-examined using a 2-phase model, in order to explore the possibility of fitting high temperature commensurate and low temperature incommensurate $Cmc2_1$ models at the transition. The patterns collected during the transition, however, show only a very subtle variation in peak shape. **Figure 3.12** shows a small 2θ range (12 – 16°) for patterns collected at 499, 505 and 513K corresponding to below, during and above the transition on heating, respectively. The pattern at 505 K contains some reflections which are broadened, which on initial analysis using a single phase, was reasonably well accounted for by refining profile coefficients. However, when overlaying patterns generated from two *Cmc*2_1 phases, it is easy to see how the pattern collected at 505 K could be constructed from an approximately 1:1 mixture of both phases.

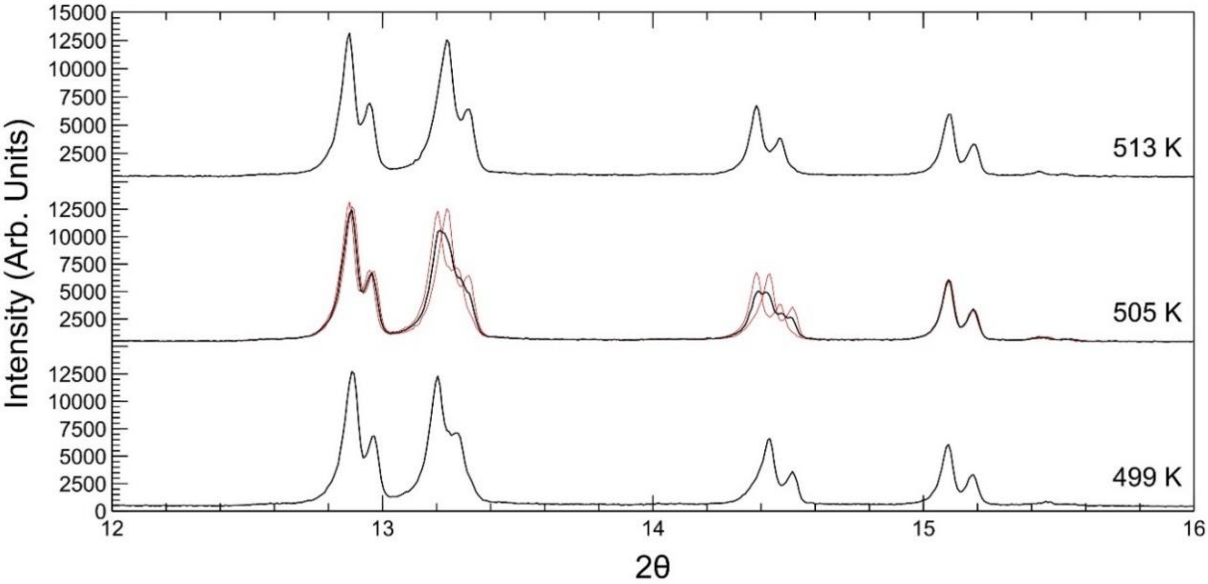

Figure 3.12: PXRD data (black curves) collected for m-LaTaO$_4$ at 499, 505 and 513 K corresponding to below, at, and just after the incommensurate – commensurate transition. Some of the diffraction peaks present at 505 K are slightly broadened in comparison to 499 and 513 K. An overlay of an equal contribution from the two *Cmc*2_1 phases of the 499 and 503 K data, each with distinct lattice parameters, (red curves) illustrate that the 505 K data can be well represented by this phase mixture.

The x-ray data collected at 505 K was refined again using two *Cmc*2_1 phases. In order to obtain reasonable starting parameters for each phase in the mixture, the patterns collected at 499 and 513 K were refined and used to generate corresponding structural models. **Figure 3.13** shows a comparison of the PXRD data refined using: (a) a single *Cmc*2_1 phase and (b) using two distinct *Cmc*2_1 phases. Visually, both sets of calculated parameters seem to fit the diffraction data well. The clearest difference between methods is shown in the improved matching of peak intensities by the two-phase methods. The overall improvement of the fit by using the two-phase method is seen more clearly by the difference curve, which has much smaller perturbations - especially above 20°2θ. Closer inspection of the 12 - 16°2θ region (inset of **figure 3.13** - the same range as **figure 3.12**) shows the similarity between each fit. **Figure 3.13(b)** shows the two-phase refinement profile, where the refined phase fraction is ~1:1 – similar to that found from analysis of PND data at this temperature.

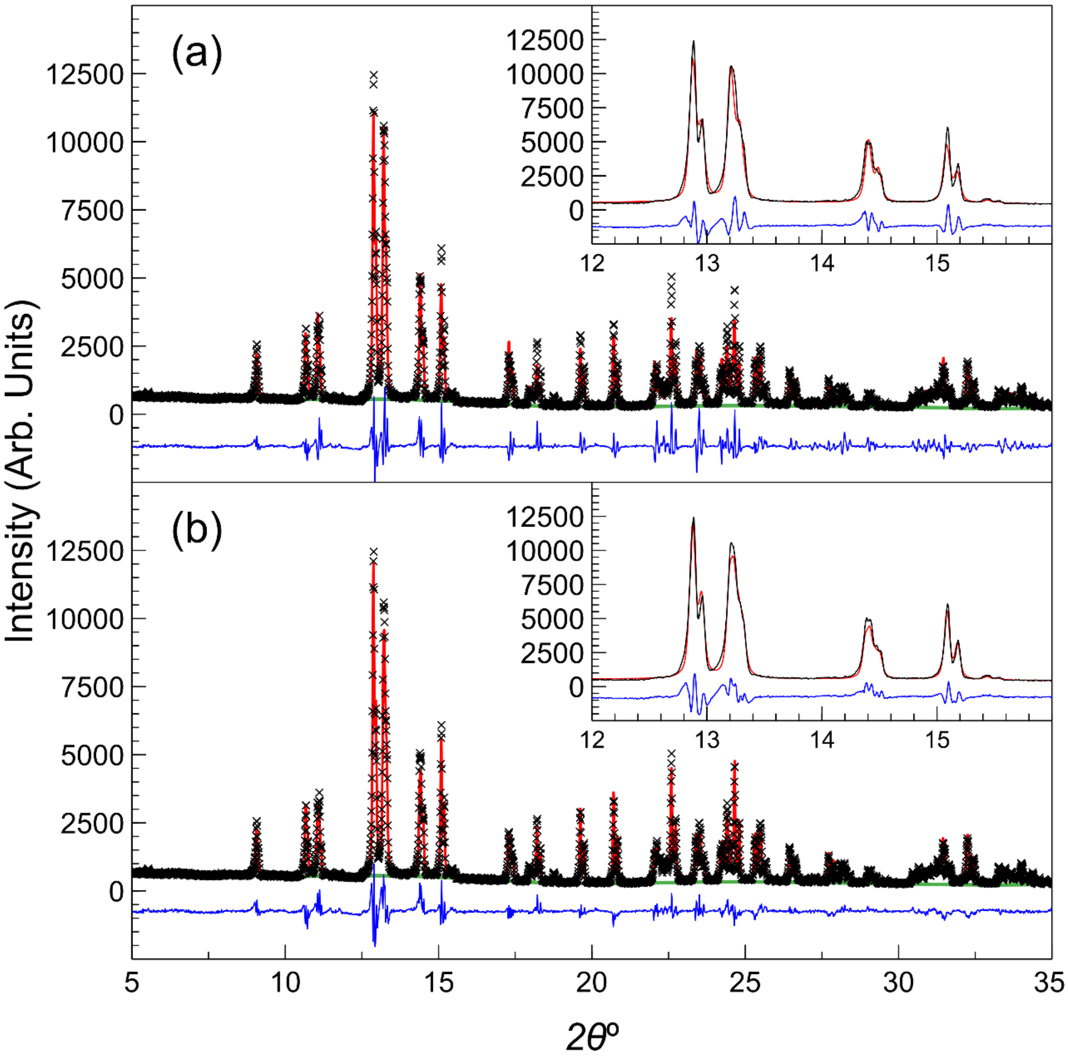

Figure 3.13: Rietveld refinement of PXRD data collected at 505 K using (a) a single *Cmc*2$_1$ model and (b) two *Cmc*2$_1$ models with different starting lattice parameters. Although visually quite similar, refinements using two distinct phases give a weighted pattern *R* factor (w*R*p = 9.89%) than that with only a single phase (w*R*p = 15.56%).

From this re-examination of the PXRD with the knowledge of the 1st order nature of the transition based on PND data it is easy to see how the PXRD data across the transition could be interpreted to be continuous in nature. If refinements of this data had been initially conducted with a two-phase model, the improvement of the fit would not be statistically significant enough to suggest that there was coexistence of two very similar $Cmc2_1$ phases. The large number of additional refined parameters that a two-phase model would introduce would not improve the goodness-of-fit by a justifiable amount - if it were not already known to be the case from refinement of PND data.

3.3.6 Strain Analysis

PND data as a function of temperature were obtained up to 773 K in a cooling sequence for o-$LaTaO_4$ and in both heating and cooling sequences up to 573 K for m-$LaTaO_4$. PND data for o-$LaTaO_4$ above 523 K were collected as part of a previous HRPD experiment by Dr Charlotte Dixon in 2013. Lattice parameters were determined by Rietveld refinements using appropriate combinations of $P2_1/c$ and (commensurate) $Cmc2_1$ models. All data points are reproduced in **figure 3.14**. o-$LaTaO_4$ exists in the incommensurate orthorhombic phase ($Cmc2_1$ (IC)) in the range of ~300 – 500 K, where there is positive thermal expansion (PTE) in the *a* and *c* axes and negative thermal expansion (NTE) of the *b* axis, **figure 3.14(a)-(c)**. It then transitions to the unmodulated phase ($Cmc2_1$ (C)) at ~500 K, which is marked by a clear decrease in the (positive) thermal expansion coefficient of *a* and *c* and change to PTE in the *b* axis.

m-$LaTaO_4$, which exists in the monoclinic phase under ambient conditions, shows PTE of all axes until it transitions to the incommensurate orthorhombic phase at ~440 K. Once in the IC phase, the lattice parameters exhibit the same behaviour as the o-$LaTaO_4$ sample, with PTE of the *a* and *c* axes, and NTE of the *b* axis until the IC-C transition at ~500 K, above which it exhibits PTE in all axes. The cell volumes of both samples exhibit PTE over the entire temperature range, **figure 3.14(d)**.

The uniaxial NTE exhibited by the IC orthorhombic phase is common in layered perovskites and is generally attributed to condensation of octahedral rotation modes and anisotropic elastic compliance.[7] Specifically, Ablitt *et al.* showed that for $LaTaO_4$ the presence of the Γ_1^+ mode, which contributes to the octahedral tilting, means that the rotation angles of the octahedra respond to changes in the *c* axis.[7] In our current investigation, it is important to note that uniaxial NTE is only observed in the $Cmc2_1$ (IC) phase and reverts to PTE in the $Cmc2_1$ (C) phase above $T_{IC\text{-}C}$. This strongly suggests that the NTE behaviour in this case is driven by the incommensurate octahedral tilting which inhibits effective packing of the perovskite layers along the *b*-axis – this is discussed in more detail in Chapter 4.

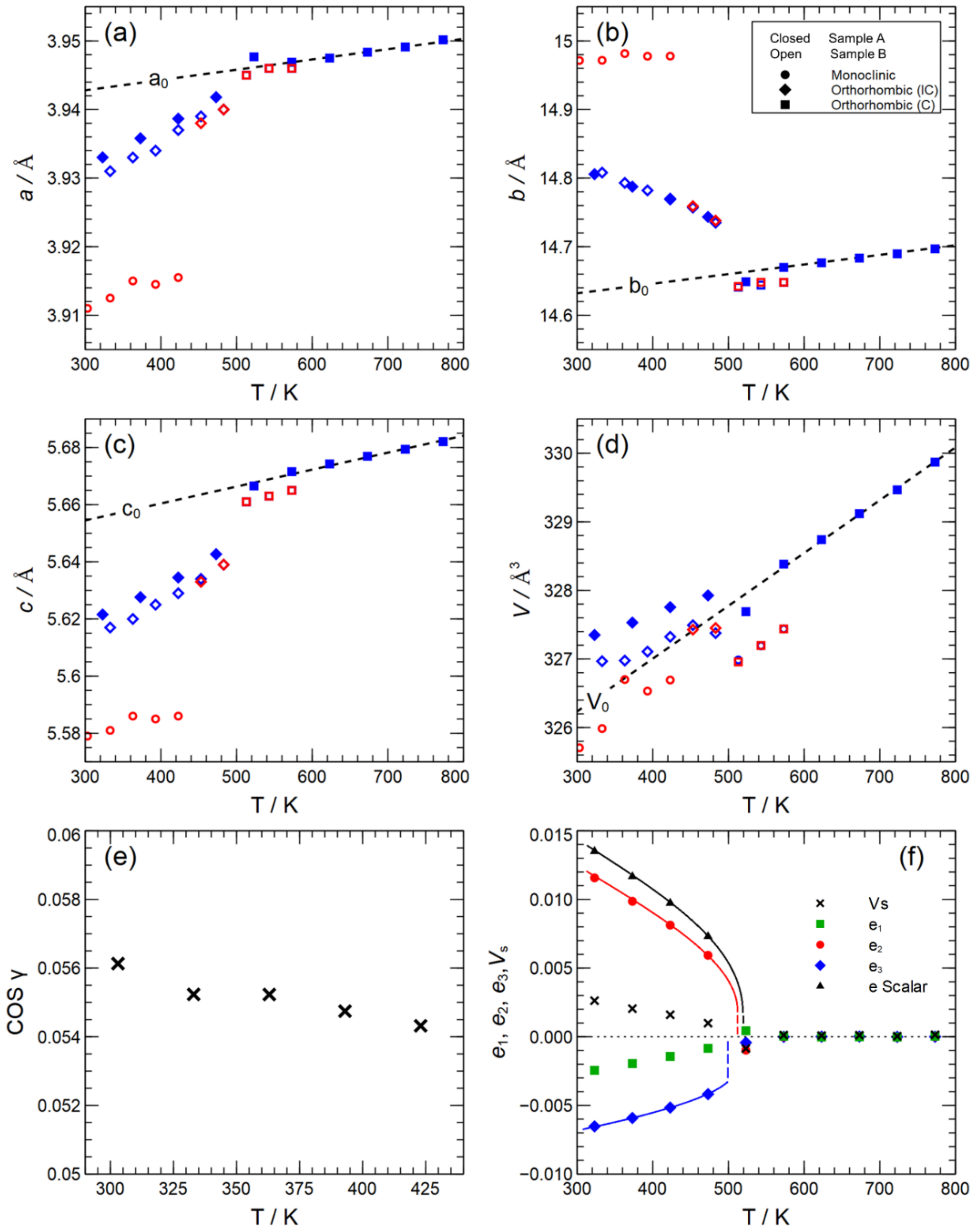

Figure 3.14: Strain analysis based on lattice parameters (a)-(d) for both o-$LaTaO_4$ (Sample A) and m-$LaTaO_4$ (Sample B). Data for the monoclinic $P2_1/c$ phase are transformed to a pseudo-orthorhombic Cmc2$_1$ unit cell for easy of comparison. Linear variations of the reference parameters, a_o, b_o, c_o, V_o, for calculation of spontaneous strains below $T_{IC\text{-}C}$ were obtained by fitting to the $Cmc2_1$ (C) phase in the temperature interval 573-773 K. Variations of lattice parameters of the m-$LaTaO_4$ sample are closely similar to those of o-$LaTaO_4$. (e) Variation of $\cos\gamma (\approx e_6)$ for the monoclinic structure of m-$LaTaO_4$, as determined from the monoclinic angle, γ, of a cell aligned with that of the $Cmc2_1$ structure. (f) Variation of spontaneous strains are defined with respect to the $Cmc2_1$ structure of o-$LaTaO_4$. Curves are fits of Equation 3.1 to the data, consistent with the view that the $Cmc2_1$ C → IC transition is weakly first order and has a transition temperature, T_{tr}, between ~510 and ~520 K.

The spontaneous strain components in the each of the three axes, e_1, e_2 and e_3, on cooling from the high temperature $Cmc2_1$ phase were determined from the lattice parameters. Reference parameters a_o, b_o and c_o were obtained from fitting data in the temperature range 573 – 773 K and extrapolated to below the IC-C transition to yield variations from these parameters. Values of the three linear strains were obtained as $e_1=(a-a_o)/a_o$, $e_2=(b-b_o)/b_o$, $e_3=(c-c_o)/c_o$, and are shown in **figure 3.14(f)**. The magnitude of each strain is up to ~1%, which is much larger than the typical strain associated with octahedral tilting transitions in perovskites.[8] The strains illustrated here are in good agreement with the above description of lattice parameters, where the incommensurate phase introduces a positive *b*-axis strain. Each strain component shows the same pattern of nonlinear variation and abrupt disappearance between 473 and 523 K, consistent with a 1st order transition. The solution for a first order transition from a 246 Landau expansion, as would apply in this case, is:

$$q^2 = \frac{2}{3}q_0^2\left\{1+\left[1-\frac{3}{4}\left(\frac{T-T_c}{T_{tr}-T_c}\right)\right]^{1/2}\right\}, \qquad 3.1$$

where q is the order parameter, q_o represents the magnitude of the discontinuity in q at the transition temperature, T_{tr}, and T_c is the critical temperature. Individual strains are related to q according to $e_1 \propto e_2 \propto e_3 \propto q^2$. Replacing q^2 by e and q_o^2 by e_o leads to the fits to e_2 and e_3 shown in **figure 3.14(f)**, representing a weakly first order transition with $T_{tr} \approx$ 510 K. The overall pattern is clear, but the fit parameters are not tightly constrained because of the limited number of data points. A "best" fit has been obtained by combining the three linear strains as a scalar strain, $e_{scalar}=\sqrt{e_1^2+e_2^2+e_3^2}$, and the fit parameters for the curve shown in **figure 3.14(f)** are T_c = 516 K, T_{tr} = 518 K, e_o = 0.0016. All three fits shown in **figure 3.14(f)** (curves, with discontinuities at T_{tr} shown as vertical dashed lines) have the same form, marking a weakly first order transition at T_{tr} between ~510 and ~520 K with differences between T_{tr} and T_c of a few degrees. There is a small, positive volume strain ($V_s = (V-V_o)/V_o \leq$ ~0.003) associated with the transition when calculated in the same way as for the linear strains [**figure 3.14(d), (f)**]. This is a consequence of the incommensuration (discussed in Chapter 4), where the modulated nature of the cation positions and associated octahedral tilting results in a small contraction in the *ac* plane but imposes a larger effect in preventing close packing of octahedral sheets in *b.*

3.3.7 Resonant Ultrasound Spectroscopy

Figure 3.15 shows a stack of spectra collected in the second cooling sequence for the o-$LaTaO_4$ sample. The y-axis represents the amplified signal from the detecting transducer, in volts, but the spectra have been offset in proportion to the temperature at which they were collected (highest temperature at the top). Resonance peaks which do not vary with temperature are from the alumina buffer rods. Peaks which vary with temperature are from the o-$LaTaO_4$ and the one which can be followed most readily through most of the temperature range has frequency ~345 kHz at 800 K. Blue peaks are fits to the data in the range where distinct elastic softening occurs with decreasing temperature.

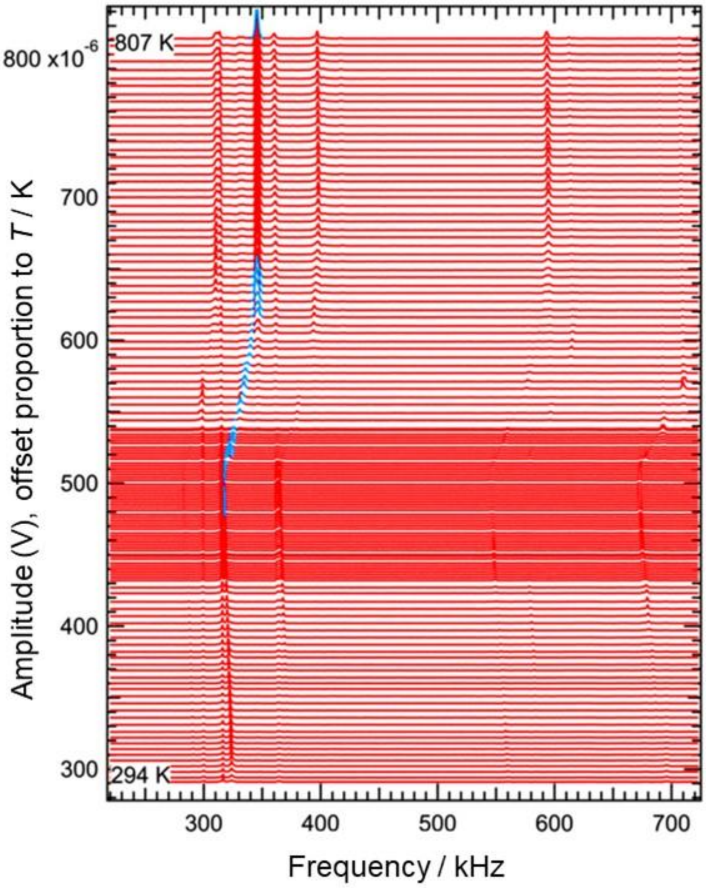

Figure 3.15: Segments of RUS spectra from polycrystalline o-$LaTaO_4$, collected in the second cooling sequence. They are stacked with offsets up the y-axis in proportion to the temperature at which they were collected. Resonance peaks which do not change frequency with changing temperature are from the alumina buffer rods. Blue lines are fits to resonance peaks of the sample in the temperature interval of elastic softening with decreasing temperature. RUS data was collected and analysed by Prof. M. A. Carpenter (University of Cambridge).

Figure 3.16 contains the results of fitting the sample peak with frequency near 345 kHz at 800 K using an asymmetric Lorentzian function. Most resonances of a polycrystalline sample involve predominantly shearing motions with the consequence that the square of peak frequencies, f^2, can be taken to scale with the shear modulus. Q^{-1} is the inverse mechanical quality factor and is a measure of acoustic loss. In RUS measurements it is generally specified as $\Delta f/f$, where Δf is the peak width at half maximum height. Elastic softening starts below ~650 K and has a rounded minimum at ~510 K, before further slight stiffening as temperature decreases further. The maximum softening amounts to ~20% of the value at high temperatures. There are small differences between f^2 values between heating and cooling sequences in the temperature interval of softening and recovery. Q^{-1} is more or less constant from ~800 K down to ~480 K where it decreases to a more or less constant lower value. There is an increase in Q^{-1} with falling temperature below ~310 K which appears to presage some increase in loss at lower temperatures.

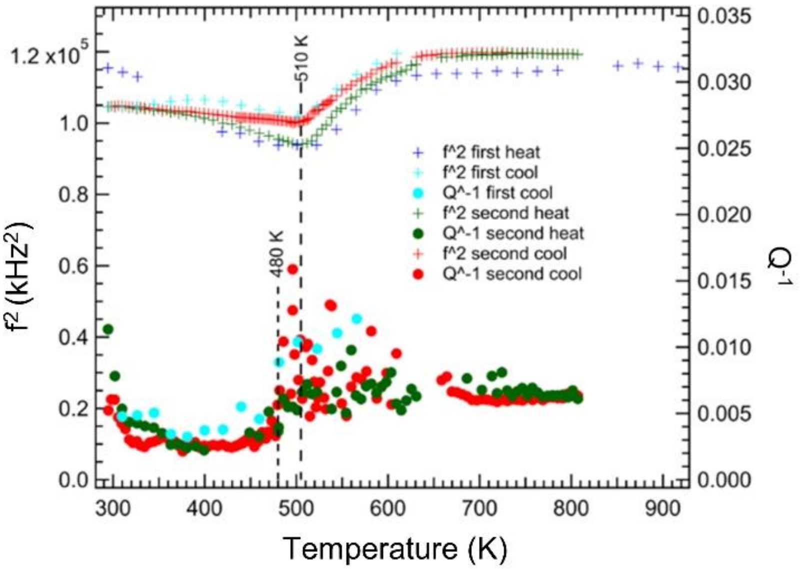

Figure 3.16: Variations of f^2 and Q^{-1} from fitting of a single resonance peak in RUS spectra from a polycrystalline sample of o-$LaTaO_4$, using an asymmetric Lorentzian function. The peak has frequency ~345 kHz at 800 K. There is a rounded minimum in f^2 at ~510 K and the small difference in values between heating and cooling has its maximum at the same temperature. There is a reduction in Q^{-1} at ~480 K and the onset of an increase below ~310 K. Scatter in the data for Q^{-1} between ~500 and ~600 K is, at least in part, an experimental artifact due to interaction of sample peaks with rod peaks. Resonant Ultrasound Spectroscopy (RUS) data was collected and analysed by Prof M. A. Carpenter (University of Cambridge).

By comparison with expected patterns of elastic softening for different types of phase transitions, as set out in Carpenter and Salje[9], the observed variation of f^2 is consistent with the $Cmc2_1$ (C) → $Cmc2_1$ (IC) transition being weakly first order (consistent with PND analysis and the Raman data described below) and having coupling between the driving order parameter and non-symmetry breaking strains. The transition is co-elastic, *i.e.* not involving any symmetry breaking strain, and the coupling terms for non-zero strains e_1, e_2, e_3 have the form λeq^2. Softening as the transition is approached from above can be accounted for by fluctuations, in the same manner as occurs ahead of the α – β transition in quartz [10]. Relatively low acoustic loss below the transition is consistent with the absence of any microstructure, such as ferroelastic domain walls, that could be mobile under applied shear stress on a time scale of ~10^{-6} s. Relatively high loss above the transition point implies that some aspect of the structure responds to externally applied dynamical stress. There is no real indication of a peak in Q^{-1} at the transition point which would be evidence of critical slowing down.

The patterns of dielectric loss, expressed either as ε'' or $\tan\delta$, are closely similar for o-$LaTaO_4$ and m-$LaTaO_4$ and for other comparable samples reported in the literature.[4,5] The loss is low at room temperatures but increases steeply above ~400 K with some dependence on frequency[5] or structure type (this study). The pattern of acoustic loss is not exactly the same but Q^{-1} shows a stepwise increase above ~480 K in the RUS data from o-$LaTaO_4$ (**figure 3.16**). Thus, it appears that there is a dielectric loss mechanism which emerges at the same temperature and measuring frequencies as a change in acoustic attenuation in o-$LaTaO_4$. There is also elastic softening in a temperature interval of ~100 K ahead of the transition, which is a typical indicator of precursor fluctuations.

Results for the $Cmc2_1$ (C) → $Cmc2_1$ (IC) transition in o-$LaTaO_4$ appear to be classical with respect to strain and elasticity. The transition temperature from strain data is between 473 and 523 K (**figure 3.14**), the minimum in shear modulus occurs at ~510 K and a drop in acoustic attenuation occurs at ~480 K (**figure 3.16**). These changes correlate more or less with a peak in permittivity observed at ~490 K during heating and at ~485 K cooling (**figure 3.3**). Incommensurate transitions tend to be second order in character (positive values of coefficient of the Landau fourth order term) but the strain and elasticity data provide direct evidence for significant coupling of the driving order parameter with non-symmetry breaking strains. This is a classic mechanism for renormalizing the Landau fourth order coefficient and could be responsible for making it negative, hence accounting for the observed weakly first order character. The pattern of softening of the shear modulus is similar to the change in velocities of some of the shear modes obtained through the equivalent transition in $BaMnF_4$, as observed by ultrasonic velocity measurements at frequencies of 4-30 MHz [11]. The transition in $BaMnF_4$ (at 250 K) has been described by Scott, where the antiferroelectric modulated orthorhombic phase has an incommensurate modulation in *c* ($Cmc2_1$ setting)[12], in contrast to the incommensurate modulation in *a* for $LaTaO_4$ (chapter 4).

RUS spectra for m-$LaTaO_4$ collected in the second cooling sequence are shown in **figure 3.17** in the same format as for spectra from o-$LaTaO_4$ in **figure 3.15**. The resonance peaks in the spectra collected from this m-$LaTaO_4$ are clearly weaker than those obtained from o-$LaTaO_4$. Most, if not all, of the resonance peaks in spectra collected below ~440 K are from the buffer rods but the increased amplitude of these in frequency ranges which follow the temperature-dependent softening of sample peaks is due to interaction of buffer rod resonances with sample resonances which are too weak and/or broad to appear directly. There are several peaks which vary systematically with temperature at higher temperatures, however, and the peak which can be followed most readily through most of the temperature range has frequency ~500 kHz at 800 K. Blue peaks are fits to this.

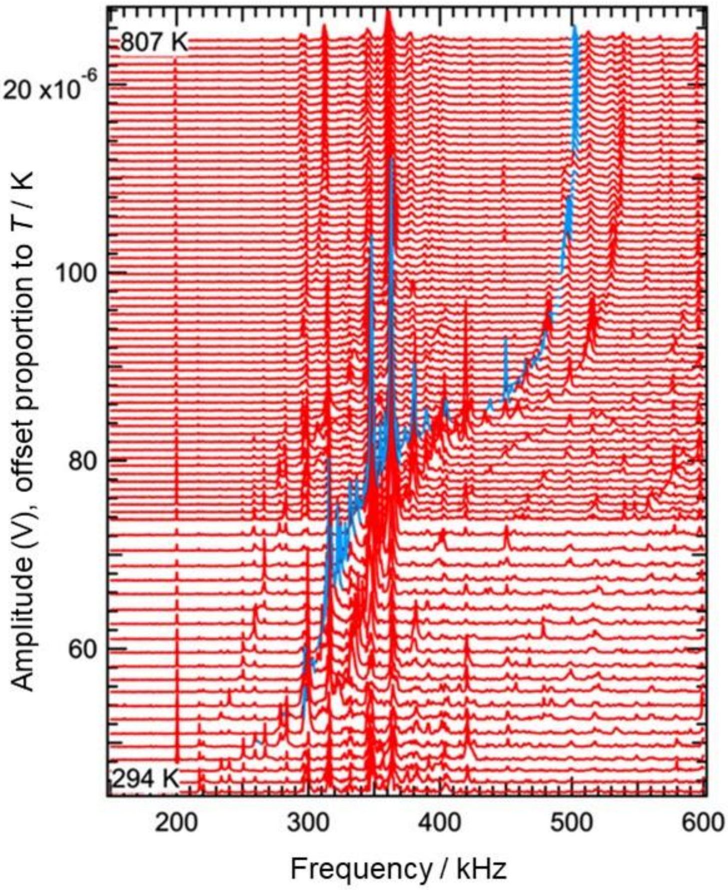

Figure 3.17: Segments of RUS spectra from a polycrystalline sample of m-LaTaO$_4$ collected in the second cooling sequence. They are stacked with offsets up the y-axis in proportion to the temperatures at which they were collected. Resonance peaks which do not change frequency with changing temperature are from the alumina buffer rods. Blue lines are fits to a resonance peak from the sample which has frequency ~500 kHz at 800 K and appears to trend towards ~220 kHz at room temperature. Resonant Ultrasound Spectroscopy (RUS) data was collected and analysed by Prof M. A. Carpenter (University of Cambridge).

Variations of f^2 and Q^{-1} from fitting of the peak highlighted in **figure 3.17** are shown as a function of temperature in **figure 3.18**, as well as variations for what appears to be the same peak in spectra collected in the prior experiments up to ~1141 K. There are three main features. Firstly, f^2 (proportional to the shear modulus) shows a softening trend from 1141 K down to ~580 K. There is then steep softening with decreasing temperature in the interval ~580-520 K. This is followed by further softening down to room temperature. Secondly, resonance peaks from the o-LaTaO$_4$ are not directly visible in spectra collected below ~400 K, indicating strong attenuation.

Finally, there is a marked hysteresis between heating and cooling shown by f^2 variations in each of the two heating/cooling sequences. As for o-LaTaO4, f^2 values are higher during cooling than during heating but they show essentially the same overall pattern of temperature dependence. Holding the o-LaTaO4 at ~1141 K for 1-2 days resulted in a shift to higher frequencies of all the resonance frequencies. Data for Q^{-1} show scatter due to the fact that all resonances from this sample were weak, but they do not show any obvious features in the interval ~1140-400K.

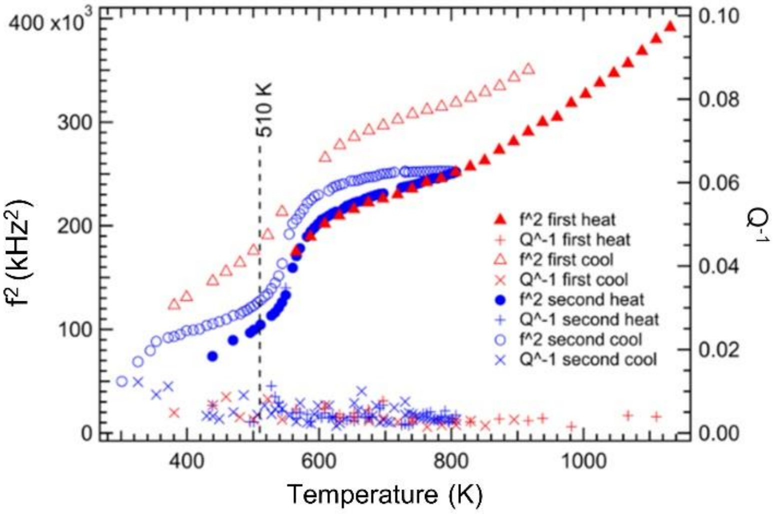

Figure 3.18: Variations of f^2 and Q^{-1} from fitting of a resonance peak which has frequency ~500 kHz at ~800 K. Individual peaks from the sample became progressively weaker and harder to distinguish from buffer rod peaks below ~430 K but the trend of elastic softening with falling temperature clearly continued below 350 K. A dashed line is shown at 510 K to mark the temperature at which a minimum in f^2 was observed in spectra from o-LaTaO4 (**figure 3.19**). Resonant Ultrasound Spectroscopy (RUS) data was collected and analysed by Prof M. A. Carpenter (University of Cambridge).

The overall pattern of softening with decreasing temperature through the full temperature interval shown in **figure 3.18** is very different from that shown by o-LaTaO4 (**figure 3.16**). It amounts to a total softening by ~80% over the full temperature interval in **figure 3.18**, rather than the ~20% step seen in **figure 3.16.** Furthermore, although the spontaneous strain variations for the $Cmc2_1$ (C) → $Cmc2_1$ (IC) transition are almost indistinguishable for the two samples, the steep softening in the interval ~580 to ~520 K is larger than the softening in o-LaTaO4 and shifted to higher temperatures. High acoustic loss below ~440 K on heating is consistent with a monoclinic structure because ferroelastic twin walls are likely to be mobile in response to an external stress in the same manner as observed in perovskites.[13]

Comparisons of the lattice parameter data for m-$LaTaO_4$ with those for o-$LaTaO_4$ indicate a closely similar pattern of strains and first order character for the $Cmc2_1$ (C) → $Cmc2_1$ (IC) transition in m-$LaTaO_4$. The transition temperature, between 483 and 513 K, is also essentially the same. However, not everything is the same between the two samples. For example, the temperature interval of steep softening ahead of the transition extends up to at least 1140 K in m-$LaTaO_4$ (**figure 3.18**) instead of only up to ~600 K (**figure 3.16**), but this could be a reflection of the quality of the ceramic in terms of how well-sintered individual grains are to each other. There is also a difference between the evolution of relative permittivity between the two samples (**figure 3.2**). The peak for o-$LaTaO_4$ at ~490 K becomes a break in slope at ~500 K for m-$LaTaO_4$. In this context it is worth noting that dielectric data of Abreu *et al.*[5] for a monoclinic sample, analogous with m-$LaTaO_4$, show a frequency dependent peak in permittivity near 500 K which falls ~5 K below the anomalies in heat capacity (~510 K) that mark the actual transition point. The increase in permittivity above the transition point shown by m-$LaTaO_4$ may therefore also be an effect arising from differences in microstructure. More significantly, the overall softening by ~80%, instead of ~20%, must be a reflection of the substantial shear strain (e_6 ~ 0.06) which distinguishes the monoclinic structure from the orthorhombic structure.

3.3.8 Raman Spectroscopy Data

Observations of low frequency phonons(s) in fluorides such as $BaMF_4$ [14,15] (which is isostructural with $LaTaO_4$) are often associated with IC-C phase transitions. Low frequency Raman spectroscopy studies on such phonon modes in $LaTaO_4$ have not yet been reported. Therefore, it is of interest to examine the low energy phonon behaviour on m-$LaTaO_4$ employing Raman spectroscopy to cover all the sequence of phase transitions of interest. **Figure 3.19** shows the Raman spectra measured at various temperatures during a heating cycle. At room temperature (298 K) two Raman modes were identified in the frequency range 10-75 cm^{-1}. The spectra exhibit dramatic changes across the monoclinic $P2_1/c$ - $Cmc2_1$ (IC) - $Cmc2_1$ (C) phase transitions from 298 to 583 K. Sudden changes in spectral features across the phase transitions indicate involvement of first order transitions. The two modes located at 42 and 54 cm^{-1} gradually shift towards each other during heating and then disappear at 443 K. A new Raman mode at 67 cm^{-1} and another at 44 cm^{-1} begin to appear at 443 K. The band frequency of 44 cm^{-1} mode shifted downward with increasing temperature and can be attributed to a soft phonon as its frequency (ϖ) decreases linearly and vanishes as the temperature approaches 528 K, the temperature at which the last of the IC phase transforms. A discussion of the soft phonon is presented later.

As can be seen in **figure 3.19**, another new mode at 56 cm^{-1} begins to appear at 493 K and its intensity increases monotonically between 493 and 583 K. These spectral features of disappearance and appearance of phonon modes clearly corroborates the phase transition from low temperature monoclinic to $Cmc2_1$ (IC) phases at 443 K and $Cmc2_1$ (IC) to $Cmc2_1$ (C) between 493 and 528 K. By analogy with the intensities of superlattice reflection peaks in neutron powder diffraction patterns, examination of the intensities of Raman bands can help with the determination of phase fractions in regions of coexistence.[16] Coexistence of IC and C phases between 493 and 583 K is evident from the observation of a unique band at 56 cm^{-1} of the high temperature $Cmc2_1$ (C) phase as shown in **figure 3.19**. The intensity of this band increases with increasing temperature in the range 493-583 K. It suggests an increase in phase fraction of $Cmc2_1$ (C) phase and corroborates the coexistence of IC and C phases, in agreement with the neutron diffraction data.

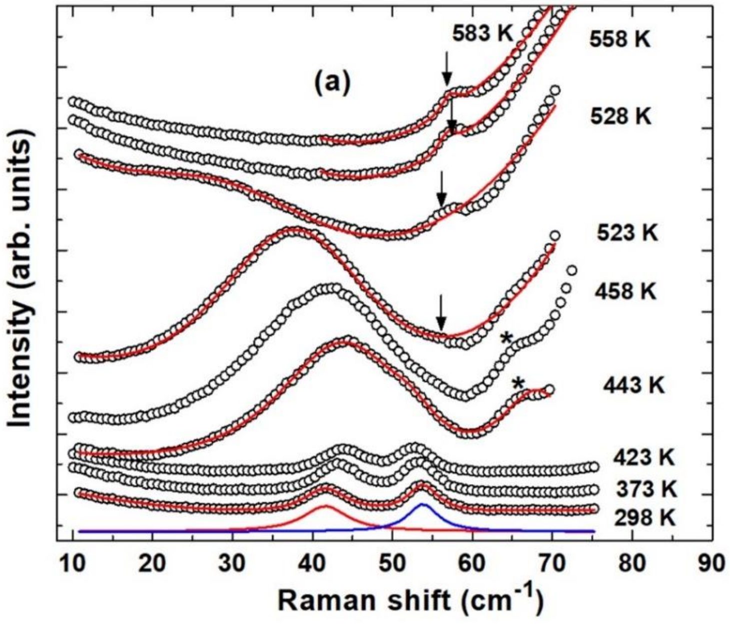

Figure 3.19: Raman spectra of m-$LaTaO_4$ sample measured at different temperatures from T = 298 – 583 K shows $T_{m\text{-}o}$ at ~443 K and region of phase coexistence at associated with $T_{IC\text{-}C}$ at 493 - 528 K. Open circles are the experimental data. Continuous solid lines are fit for individual Raman bands and total Lorentzian fit to the data. Appearance of new Raman modes are indicated by arrow and star symbols. Raman Spectroscopy data was collected and analysed by Dr. K. K. Mishra and Prof. R. S. Katiyar (University of Puerto Rico).

The temperature dependences of the phonon frequencies are shown in **figure 3.20**. Phonons in the $Cmc2_1$ (IC) phase have stronger dependence on temperature, indicating higher anharmonicity of this phase. The soft mode with frequency 44 cm^{-1} at 443 K originates from the fluctuation in incommensurate structural modulation and would freeze ($\varpi = 0$) on transformation to the commensurate phase.

Raman spectral activity (selection rules) is closely related to the point group of the crystal involved. As both the IC and C $Cmc2_1$ have the same point group, C_{2v}, all the zone centre ($q = 0$) Raman active phonons of the $Cmc2_1$ (IC) phase are expected to also be active in the $Cmc2_1$ (C) phase. The fact that the soft phonon is frozen in the IC-phase and becomes inactive in the C-phase suggests that it is a zone boundary (q) phonon of the high temperature $Cmc2_1$ (C) phase. The structural modulation is driven by this soft zone boundary phonon of $Cmc2_1$ (C) phase which is observed as a zone centre phonon in the $Cmc2_1$ (IC) due to folding of zone boundary phonons into the Brillouin zone centre ($q = 0$). A soft zone boundary phonon with frequency 40 cm^{-1} at low temperatures is important in the IC-C phase transition of the isostructural $BaMnF_4$ compound [14].

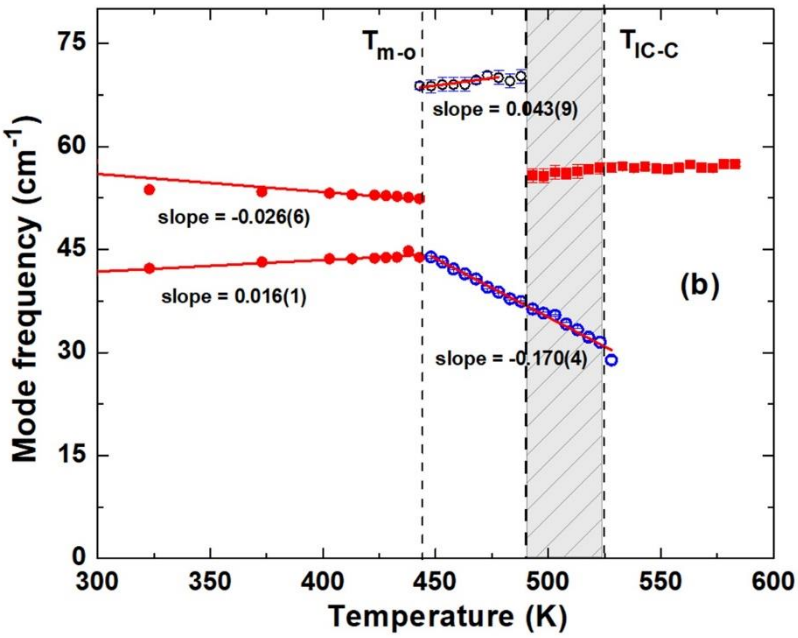

Figure 3.20: Temperature-dependent Raman mode frequencies of m-$LaTaO_4$. Discontinuous changes of the mode frequencies are consistent with both transitions being first order. A zone boundary soft mode of the $Cmc2_1$ (C) phase appears at $T_{m\text{-}o}$ = 443 K with frequency 44 cm^{-1} and continuously softens, disappearing at ~528 K. Raman Spectroscopy data was collected and analysed by Dr. K. K. Mishra and Prof. R. S. Katiyar (University of Puerto Rico).

The Raman spectra measured in low temperature (298 K) monoclinic (point group: C_{2h}) and high temperature (460 K) orthorhombic IC phases (point group: C_{2v}) are depicted in **figure 3.21**. Several discernible and unique Raman peaks in spectrum for the orthorhombic *Cmc*2_1 phase, such as those located at 78, 101, 643, 843 cm^{-1}, are not observed in the spectrum measured at 298 K, suggesting that absence of any substantial coexistence of orthorhombic *Cmc*2_1 phase at room temperature. The optical phonons in the high temperature orthorhombic phase (*Cmc*2_1) are $\Gamma_{opt} = 11A_1+6A_2+5B_1+11B_2$, where A_1, A_2, B_1 and B_2 are non-degenerate Raman active modes, and A_1, B_1 and B_2 are non-degenerate IR active modes[5]. Hence, 33 Raman active non-degenerate optical phonons are expected. On the other hand, the optical phonons in the room temperature monoclinic phase (*P*2_1/*c*) are $\Gamma_{opt} = 18A_g+18B_g+17A_u+16B_u$, where A_g and B_g modes are Raman active, and A_u and B_u are IR active [5]. All these A_g, B_g, A_u, B_u modes are non-degenerate. Hence, 36 Raman active nondegenerate optical phonons are expected. **Figure 3.21** shows the Raman spectra of $LaTaO_4$ measured at 298 and 460 K. At 298 K, a total of 26 distinct Raman bands were identified in the frequency range 10-1000 cm^{-1}. On the other hand, at 460 K, only 21 distinct Raman bands could be found in the same frequency range. The number of bands experimentally observed is lower than actually group theoretically predicted ones, which could be due to either accidental degeneracy of band frequency or inadequate intensity arising from small polarizability of several Raman bands[17]. The sharpening of the line widths at low temperature (298 K) is understood to be due to thermal effects. However, the sharpening of the linewidths cannot explain the additional Raman bands observed at low temperature. Raman spectra of the sample were measured in the frequency range 10-1000 cm^{-1} employing a triple monochromator-based HORIBA Jobin Yvon micro-Raman spectrometer with a spectral resolution of ~1 cm^{-1}. Therefore, it is clear that the broad Raman bands at 460 K cannot hide peaks spaced more than 1 cm^{-1}. The smallest spacing between the bands in the 298 K spectrum is ~10 cm^{-1} (e.g., there are bands at ~42, 54, 115 and 126 cm^{-1}) as shown in **figure 3.21(b)**. So, they would be well resolved in the 460 K spectrum if present. Since they are not present in the orthorhombic 460 K spectrum, they are not observed. Thus, those bands are not hidden under the broad bands due to resolution problems. The asymmetry in the line shape in the 460 K spectrum is most likely due to phono-phonon interaction between same symmetry phonons.

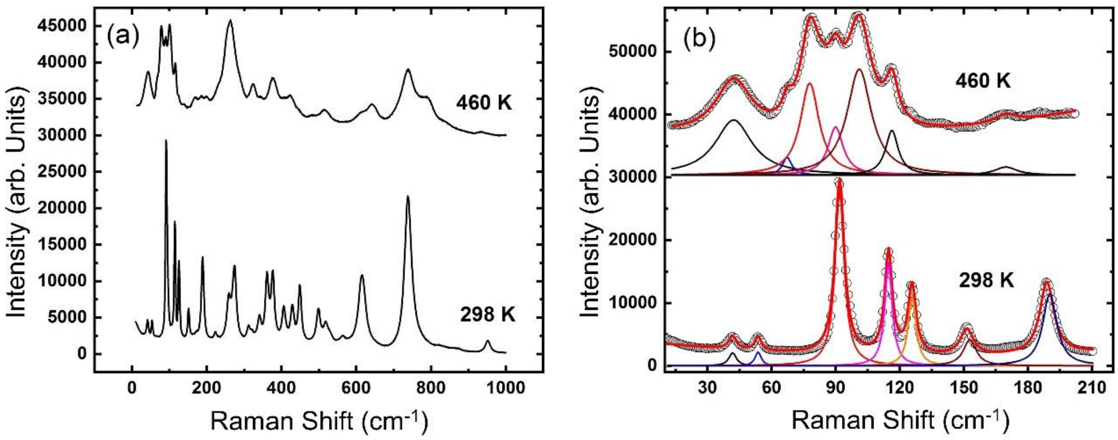

Figure 3.21: (a) Raman spectra of m-$LaTaO_4$ in the frequency range 10-1000 cm^{-1}, as measured at 298 K (monoclinic phase) and 460 K ($Cmc2_1$ (IC) phase). The large number of almost equal spaced Raman lines with frequencies in the range 100-500 cm^{-1} in the spectrum of the low temperature $P2_1/c$ phase (at 298 K) suggests that the monoclinic phase involves at least a 4× multiplication of the primitive unit cell of the already modulated orthorhombic $Cmc2_1$ (IC) phase. (b) Low frequency Raman spectra deconvoluted to sum of Lorentzian peaks for monoclinic phase (298 K) and orthorhombic phase (460 K). Individual fitted peaks are also shown. Raman Spectroscopy data was collected and analysed by Dr. K. K. Mishra and Prof. R. S. Katiyar (University of Puerto Rico).

Raman spectroscopy is often useful to infer longer unit cell (Brillouin zone folding) of phase involved in crystallographic phase transition. If a vibrational branch (such as a longitudinal optical vibration) is subject to n folds of its Brillouin zone, it will give rise to n-1 new evenly spaced vibrations of comparable intensity[14,18]. Suppose the unit cell approximately doubles along c-axis at low temperature. This will permit Raman spectra of one extra very low frequency optical phonon, which would be described as Brillouin zone boundary in the high temperature phase. Suppose instead that the unit cell quadruples. This will permit three extra lines, almost evenly spaced in frequency.

This is the logic behind the argument which suggests that the monoclinic phase of $LaTaO_4$ below $T_{\text{m-o}}$ ~443 K is likely to have at least quadruple multiplication of primitive unit cell of high temperature orthorhombic phase. **Figures 3.19 and 3.20** show that a soft Raman band appears around 44 cm^{-1} in the incommensurate orthorhombic phase near 443 K and disappear in high temperature orthorhombic C phase above 528 K. Below the orthorhombic IC phase near 443 K, this soft band disappears and a doublet around 42 and 54 cm^{-1} is found. The doublet is worthy of note, because no Raman active phonons are doubly degenerate in any orthorhombic symmetry. Therefore, the peak doubling is more likely to arise from a folding of at least 4× in the unit cell along a particular axis; that is, these two lines are probably low frequency optical modes at $q^*/2$ and $q^*/4$ in the original pseudo-orthorhombic phase, and their doubling is not from the monoclinic distortion but from the unit cell multiplication. Further support for a large supercell of the monoclinic phase below $T_{m\text{-}o}$ ~443 K comes from the very large number of Raman lines, and from the almost uniform spaced array of nearly half a dozen Raman lines of comparable intensity at 100-500 cm^{-1} in 298 K spectrum (**figure 3.21(a)**), indicating that vibrational optical branch is subjected to multifold to its Brillouin zone. It can be mentioned that 500 cm^{-1} is a reasonable value for LO phonon (maximum frequency) in a relatively hard material. Although the Raman data above indicates there may be a multiplication of the primitive cell, the other techniques employed in this current investigation have shown no further evidence of such superstructure. However, as an incommensurate monoclinic phase has been observed in the isostructural fluoride, $BaMnF_4$ [19], it would be worth investigating this possibility in future work. As discussed in the next chapter, the local origin of the incommensuration in the orthorhombic phase of $LaTaO_4$ was identified by electron microscopy. It would then be appropriate to explore the possibility of a similar modulation in the monoclinic phase using this technique, as a follow up to this current work.

3.4 Summary and Conclusions

Using a variety of complementary techniques, the phase transition sequence of $LaTaO_4$ from 298 to 773 K has been re-established using new knowledge of an intermediate, modulated orthorhombic phase. The symmetry sequence for $LaTaO_4$ is as follows:

$$P2_1/c \underset{\sim 303\text{ K}}{\overset{\sim 440\text{ K}}{\rightleftharpoons}} Cmc2_1\,\text{(IC)} \xleftrightarrow{\sim 503\text{ K}} Cmc2_1\,\text{(C)} \xleftrightarrow{?} Cmcm$$

It is now shown that on heating, m-$LaTaO_4$ samples will undergo a first order structural phase transition at ~440 K, not to the basic $Cmc2_1$ phase as originally reported, but instead to an incommensurately modulated $Cmc2_1$ structure. o-$LaTaO_4$ samples which already adopt this phase under ambient conditions undergo a transition to the monoclinic phase on cooling below room temperature. PND data collected for both sample types reveal a clear set of satellite peaks which belong to this intermediate phase – these act as evidence of the modulation and allow the modulated structure to be explored in detail (discussed in the next chapter).

Initial in-house PXRD methods had already determined that the conclusions reached by Abreu[5] were incorrect by allowing the structure above the transition at ~480 K to be fitted to a $Cmc2_1$ model, but the relative insensitivity of this technique did not reveal the modulation of the $Cmc2_1$ or allow for the nature of the transition to be correctly determined. Close inspection of PND data at $T_{\text{IC-C}}$ revealed a clear discontinuity of diffraction peaks and phase coexistence at $T_{\text{IC-C}}$ - evidence of a 1st order structural transition which is in direct contrast to the initial evidence of a continuous, 2nd order transition suggested by PXRD data. The identification of the modulated intermediate phase would hence have likely been impossible without the use of more sensitive structural techniques, such as PND or electron diffraction.

From this investigation the nature of the $P2_1/c$ – $Cmc2_1$ (IC) transition ($T_{\text{m-o}}$) and the $Cmc2_1$ (IC) - $Cmc2_1$ (C) transition ($T_{\text{IC-C}}$) have been revealed. The transition sequence with falling temperature in $LaTaO_4$ is $Cmc2_1$ (C) $\rightarrow$ $Cmc2_1$ (IC) $\rightarrow$ $P2_1/c$. The $Cmc2_1$ (C) $\rightarrow$ $Cmc2_1$ (IC) transition is allowed by symmetry to be thermodynamically continuous, and it is commonly found that transitions to incommensurate structures are second order in character. $P2_1/c$ is a subgroup of $Cmcm$ but not of $Cmc2_1$ (including the IC structure), so that $Cmc2_1$ (IC) $\rightarrow$ $P2_1/c$ is necessarily first order - the order parameter has one non-zero component and the transition is improper ferroelastic. As well as the aforementioned PND results, discontinuity in some Raman peaks and the elastic properties depicted by the RUS data is coherent in indicating a weakly first order structural transition. At some high temperature both o-$LaTaO_4$ and m-$LaTaO_4$ would be expected to eventually transform to the parent (untilted) $Cmcm$ structure but is as-yet unreported. $Cmc2_1$ and $P2_1/c$ are different subgroups of $Cmcm$ and the active representation for $Cmcm \rightarrow Cmc2_1$ is Γ_2^- [20]; the order parameter has one component and the $Cmc2_1$ phase is a proper ferroelectric. The, as yet unreported, $Cmcm \rightarrow Cmc2_1$ transition would therefore be allowed by symmetry to be thermodynamically continuous.

3.5 References

1. Cava, R. J. & Roth, R. S. The Structure Analysis of $LaTaO_4$ at 300 °C by Neutron Powder Profile Analysis. *J. Solid State Chem.* **36**, 139–147 (1981).
2. Vullum, F., Nitsche, F., Selbach, S. M. & Grande, T. Solid Solubility and Phase Transitions in the System $LaNb_{1-x}Ta_xO_4$. *J. Solid State Chem.* **181**, 2580–2585 (2008).
3. Siqueira, K. P. F. & Dias, A. Effect of the Processing Prameters on the Crystalline Structure of Lanthanide Orthotantalates. *Mater. Res.* **17**, 167–173 (2014).
4. Cordrey, K. J. *et al.* Structural and Dielectric Studies of the Phase Behaviour of the Topological Ferroelectric $La_{1-x}Nd_xTaO_4$. *Dalt. Trans.* **44**, 10673–10680 (2015).
5. Abreu, Y. G., Siqueira, K. P. F., Matinaga, F. M., Moreira, R. L. & Dias, A. High-temperature antiferroelectric and ferroelectric phase transitions in phase pure $LaTaO_4$. *Ceram. Int.* **43**, 1543–1551 (2017).
6. Hidaka, M., Nakayama, T., Scott, J. F. & Storey, J. S. Piezoelectric resonance study of Structural Anomalies in $BaMnF_4$. *Phys. B+C* **133**, 1–9 (1985).
7. Ablitt, C., Craddock, S., Senn, M. S., Mostofi, A. A. & Bristowe, N. C. The Origin of Uniaxial Negative Thermal Expansion in Layered Perovskites. *npj Comput. Mater.* **3**, 44 (2017).
8. Carpenter, M. A., Bacerro, A. I. & Seiferi, F. Strain Analysis of Phase Transitions in (Ca,Sr)TiO3 Perovskites. *Am. Mineral.* **86**, 348–363 (2001).
9. Carpenter, M. A., Salje, E. K. H. & Graeme-Barber, A. Spontaneous Strain as a Determinant of Thermodynamic Properties for Phase Transitions in Minerals. *Eur. J. Mineral.* **10**, 621–691 (1998).
10. Carpenter, M. A. *et al.* Calibration of Excess Thermodynamic Properties and Elastic Constant Variations Associated with the α ↔ β Phase Transition in Quartz. *Am. Mineral.* **83**, 2–22 (1998).
11. Fritz, I. J. Ultrasonic Velocity Measurements Near the 250°K Phase Transition in $BaMnF_4$. *Phys. Lett. A* **51**, 219–220 (1975).
12. Scott, J. F. Phase transitions in $BaMnF_4$. *Reports Prog. Phys.* **42**, 1055–1084 (1979).
13. Carpenter, M. A. Static and Dynamic Strain Coupling Behaviour of Ferroic and Multiferroic Perovskites from Resonant Ultrasound Spectroscopy. *J. Phys. Condens. Matter* **27**, (2015).
14. Ryan, J. F. & Scott, J. F. Raman study of Soft Zone-Boundary Phonons and Antiferrodistortive Phase Transition in $BaMnF_4$. *Solid State Commun.* **14**, 5–9 (1974).
15. Quilichini, M., Ryan, J. F., Scott, J. F. & Guggenheim, H. J. Light Scattering from Soft Modes in Ferroelectric $BaZnF_4$ and $BaMgF_4$. *Solid State Commun.* **16**, 471–475 (1975).

16. Ravindran, T. R., Sivasubramanian, V. & Arora, A. K. Low Temperature Raman Spectroscopic Study of Scandium Molybdate. *J. Phys. Condens. Matter* **17**, 277–286 (2005).

17. Mishra, K. K. *et al.* Soft modes and anharmonicity in $H_3[Co(CN)_6]$: Raman Spectroscopy and First-Principles Calculations. *Phys. Rev. B - Condens. Matter Mater. Phys.* **92**, 1–9 (2015).

18. Dultz, W., Krause, H. & Winchester, L. W. The Raman Spectrum of NaCN Under Hydrostatic Pressure. *J. Chem. Phys.* **67**, 2560–2566 (1977).

19. Sciau, P., Lapasset, J., Grebille, D. & Berar, J. F. Incommensurate Modulated Structure of $BaMnF_4$ with Monoclinic Symmetry at 100 and 210 K. *Acta Crystallogr. Sect. B Struct. Sci.* **44**, 108–116 (1988).

20. Liu, X. Q., Li, G. J. & Chen, X. M. Topological Ferroelectricity in Layered Perovskite $LaTaO_4$: A first Principles Study. *Solid State Commun.* **247**, 31–35 (2016).

4 Chapter 4: Incommensurate Orthorhombic Phase in $LaTaO_4$

4.1 Introduction

With the discovery of an incommensurate modulation existing in $LaTaO_4$, the next logical step is to fully characterise the modulated structure. The Carpy – Galy, $A_nB_nX_{3n+2}$ structures are comprised of 'sheets' of interconnected BX_6 octahedra separated by inter-octahedral A-cations – the thickness these sheets being related to *n*. The value of *n* can be thought of as the number of octahedra deep each 'sheet' is – with larger values of *n* bringing the structure closer to that of the conventional 3D perovskite. The polar orthorhombic phase of this material contains sheets of octahedra which all tilt in-phase with an accompanying shift of the inter-octahedral cation in the polar axis. Luckily, there are several of these Carpy – Galy materials which exhibit a modulated orthorhombic phase. The family of isostructural $n = 2$ fluorides, $BaMF_4$ (M^{2+} = Mn, Fe, Mg, Zn), which have been studied extensively, contain many members which contain similar (incommensurately) modulated orthorhombic phases. The modulation wavevector, *q*, in these materials runs parallel to the polar axis (it is important to note that these studies use the $A2_1am$ space group, which is an alternative setting of $Cmc2_1$). The modulation arises from a continuous displacement of inter-octahedral cations with an associated distortion of the octahedral sheets.[1–7] Unfortunately, other incommensurate $n = 2$ Carpy – Galy oxides have not been reported from which to draw comparisons, but the $n = 4$ oxides, $Sr_2Nb_2O_7$ and $La_2Ti_2O_7$, both have reported incommensurately modulated orthorhombic phases. Although the nature of the modulation in these oxides is structurally similar to the fluorides, the wavevector runs orthogonal, rather than parallel, to the polar axis.[8,9]

In this chapter, a structural model for the incommensurately modulated (IC) phase is constructed from various diffraction techniques. The satellite reflections identified in the PND data are fully accounted for using a $Cmc2_1(\alpha 00)0s0$ superspace group, which is comparable to a previous study of the $n = 4$ oxide, $Sr_2Nb_2O_7$. The modulation vector refines to give a value of $q \approx (0.456\ 0\ 0)$ at 483 K which equates to an approximate 11× supercell in the *a*-axis. The modulation is driven by the displacement of inter-octahedral La^{3+} cations, towards and away from the octahedral layers, which in turn corrugate cooperatively with the cation displacements. These structural distortions are thought to arise as a mechanism to improve the overall bonding environment of La^{3+}, which is shown as an overall improvement in calculated bond valence sum (BVS) for the IC phase when compared to the unmodulated structure.

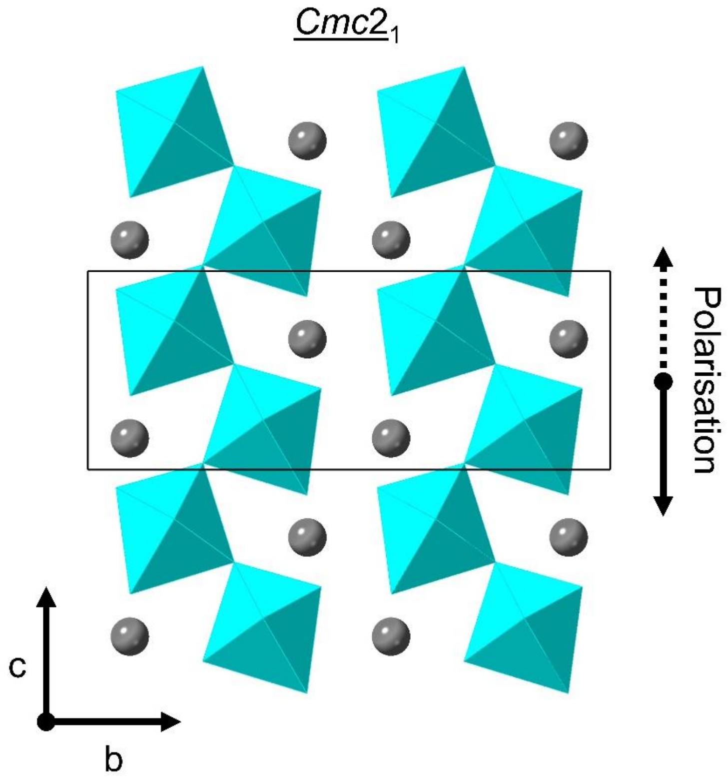

Figure 1: Structural Diagram of the $Cmc2_1$ phase with polarisation along *c* orientated downwards on the page.

The local origin of the modulation is also investigated by electron microscopy techniques, which reveal that the incommensuration arises from a partial ordering in the *a*-axis of smaller units with structural variations. These structural units, M and N, are 3× and 2.5× expansions of the basic $Cmc2_1$ cell, respectively. While this is at odds with the continuous displacement model constructed from PND data, it is found that both models are somewhat consistent and the latter 'averaged' model provides the vital clues for the origin of the modulation. The ~11× supercell generated by the PND model is easily broken down into 2M and 2N units – suggesting the macroscopic modulation is constructed of these two units in approximately equal quantities, although the ordering at the local level can vary.

4.2 Methods

PND data was collected on the orthorhombic sample using the high-resolution powder diffraction (HRPD) instrument at ISIS. Data was collected on cooling from 523 K in 2 K increments to 483 K, for close observation of the IC-C phase transition – collection time for each time was 1 h (40 μAh integrated proton current to the target), except 483 K and 523 K which was 3 h (120 μAh). Data was also collected between 473 K and 323 K at 50 K increments for observation of modulation of vector as a function of temperature – all collection times were 3 h (120 μAh). Data collection on cooling was performed to eliminate any residual monoclinic phase. Approximately 5 g of sample was analysed. PND data were refined by the Rietveld method using GSAS software.[10,11] Jana2006[12] was used in determining the modulated structure from variable temperature PND data. The modulation vector is typically presented as $q = (\sigma_1, \sigma_2, \sigma_3)$, where each sigma value represents a fractional coordinate with respect to reciprocal unit cell axes a^*, b^* and c^*, respectively.

Selected area electron diffraction (SAED) patterns and high-resolution transmission electron microscopy (HRTEM) images were recorded using a Gatan 794 CCD camera on a JEOL JEM-2011 electron microscope fitted with a LaB_6 filament operating at an accelerating voltage of 200kV. For sampling, specimens were ground into powder in acetone with a pestle and mortar. A copper grid coated with a thin holey carbon film was used to support the powder sample. All TEM images were collected by Dr Shitao Wu.

4.3 Results

4.3.1 Determination of Macroscopic Modulation

Jana2006 was used to determining the modulated structure from variable temperature PND data. The super-space group (SSG) was taken from a study of comparable $n = 4$ materials (*e.g.* $Sr_2Nb_2O_7$) where there is a similar modulation observed in the *a* axis.[8,9] Although these $n = 4$ analogues have a modulation vector of $q \approx (0.5, 0, 0)$ and is similar to the doubling of the *a* axis in $BaMnF_4$ ($A2_1am$ space group setting), reported by Hidaka.[13] It is important to note that due to the alternate space group setting the incommensuration in $BaMnF_4$ lies along the polar axis, but in the $n = 4$ oxides the incommensuration is orthogonal to the polarisation. Given the similarities between the reported modulations in $A_2B_2O_7$ ferroelectrics and the candidate modulation vectors determined from TEM here, a modulation vector of approximately $q = (0.5, 0, 0)$ was used as an initial value in refinements of data at 483 K. This resulted in a final value of q = (0.456, 0, 0) for $LaTaO_4$ at 483 K. Refining the PND data collected for the incommensurate phase using the $Cmc2_1(\alpha00)0s0$ SSG, with a maximum satellite index of 3, gave a satisfactory fit of all reflections, with an overall $\chi^2 = 2.57$ (wRp = 5.6%) across two HRPD detector banks (**Figure 4.2**).

The symmetry operations induced by the superspace group $Cmc2_1(\alpha00)0s0$ are listed fully in **table 4.2**. These contain the usual operations expected of a basic $Cmc2_1$ structure but with the addition of a *t* component which indicates the modulation phase at that given position. For example, the fraction which follows this *t* component indicates a shift in the modulation phase for this atomic position, *i.e.*, the displacement of the atom in this position is that of *t* + ½, where atoms without an indicated shift in modulation are at *t*.

Table 1: Symmetry operations induced by the $Cmc2_1(\alpha00)0s0$ superspace group.

x	y	z	t
- x	- y	z + ½	-t
x	- y	z + ½	t + ½
- x	y	z	- t + ½

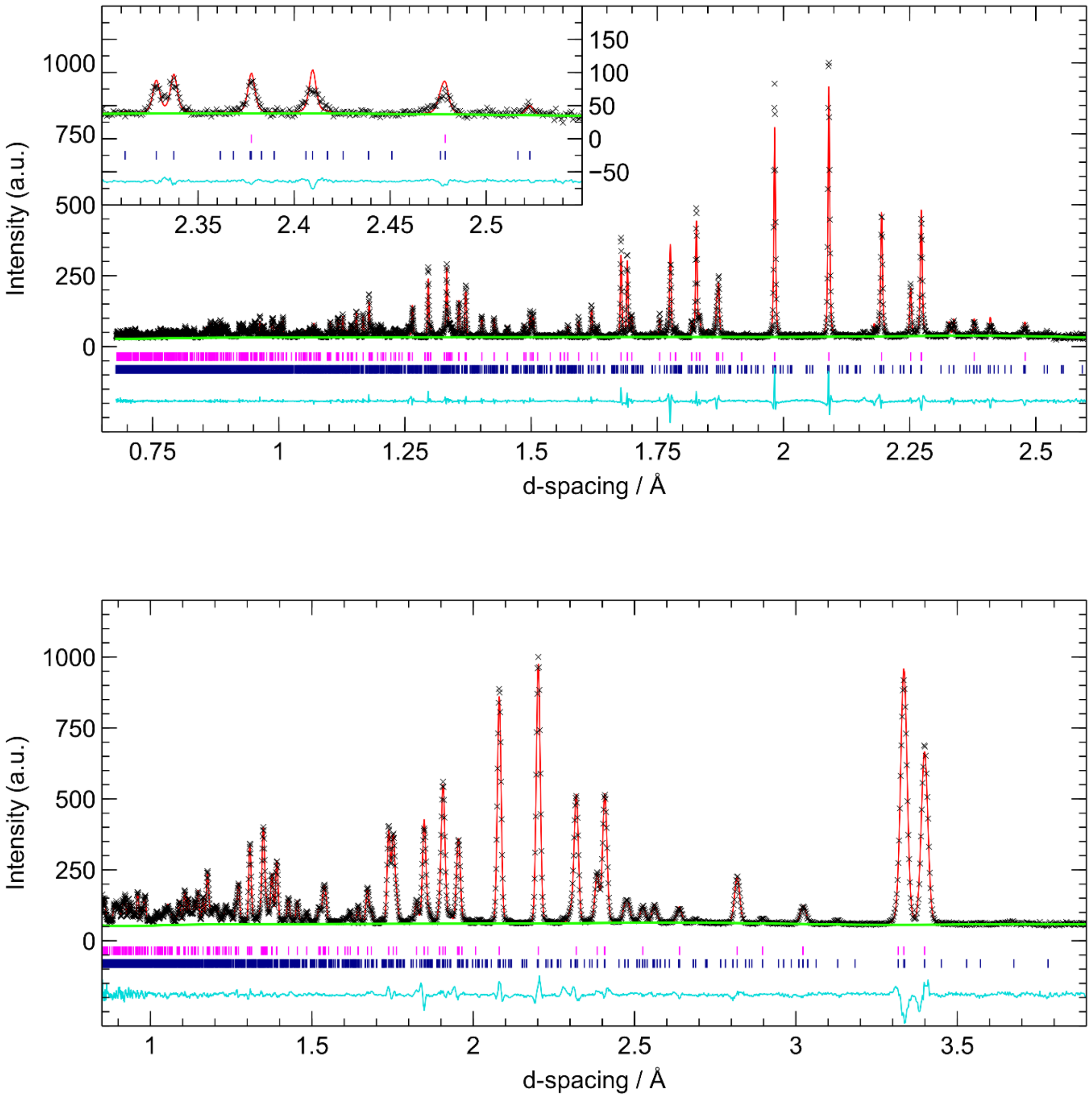

Figure 4.2: Profile fits using JANA2006 of diffraction data collected on HRPD detector banks 1 (top) and 2 (bottom) at 483 K. Observed data is shown as black crosses and the calculated pattern as a red line. The background (green) and difference (cyan) curves are also shown. Main reflections are denoted by magenta (upper) ticks and satellite reflections are represented by dark blue (lower) ticks. Superspace group $Cmc2_1(\alpha 00)0s0$ was used to fit the modulated structure with w*R*p = 5.6%. The refined value of α = 0.456 *i.e.*, q = (0.456, 0, 0). Calculate satellite reflections of up to the 3rd order were used to fit the pattern with structural modulations being characterised by a 3rd order Fourier function. Higher order functions did not improve the fit.

It is clear from visual inspection of the data collected at 323 K that there is an improved fit when considering a modulated model. The most prominent satellite reflections that were highlighted in chapter 3 are now well accounted for by the refined modulated structure. **Figure 4.3** shows a comparison of the Rietveld refinements of the data collected for o-$LaTaO_4$ at 323 K; one considering only the basic $Cmc2_1$ structure and one with the modulated $Cmc2_1(\alpha 00)0s0$ model. As mentioned in the previous chapter, refinement of PND data found that o-$LaTaO_4$ samples contained approximately 6 wt% monoclinic phase.

The diffraction data presented in the top panel of **figure 4.3** is a reproduction of that shown in chapter 3 (with a smaller d-spacing range which focusses on the most prominent satellite reflections), where a two-phase refinement of o-$LaTaO_4$ at 323 K is performed using the basic (commensurate) $Cmc2_1$ and $P2_1/c$ models. This yielded a fit with wRp = 8.59% and revealed a monoclinic content of 5.9 wt%. However, comparing the calculated and observed patterns shows small discrepancies in the fitting of the data with the pair of peaks observed at approximately 2.4 Å shown to be poorly fit by the refinement. These observed reflections are known to be satellite reflections due to their persistence up to T_{IC-C} and the ability to fit them sufficiently well with a modulated orthorhombic phase (as shown in **figure 4.3**). The tick marks below the plot are indicative of the calculated reflections produced by the model and these show that the JANA2006 is attempting to erroneously fit the monoclinic phase to the satellite reflections (this was expected to result in an overestimation of monoclinic phase fraction). The satellite reflection at 2.46 Å is not fitted at all.

The bottom panel of **figure 4.3** is a refinement of the same dataset but with a modulated orthorhombic phase. It is immediately clear that this model more closely represents o-$LaTaO_4$ at 323 K as all satellite reflections are now adequately fitted. This is reflected in the fit statistics of this new model with wRp = 5.24% - an improvement of 3.35%. The satellite reflections are completely accounted for by the modulated orthorhombic phase and as expected the monoclinic phase fraction has dropped to 5% - a much smaller decrease than what was expected. It can also be seen from the plot that some main reflections now have much improved fit. In both cases gamma 1 and 2, and sigma 1 and 2 profile coefficients have been allowed to refine but it seems that the erroneous fitting of the satellite peaks has prevented the refinements from converging on appropriate profile coefficients. This is most obvious when observing the differences in the peak at 2.36 Å in each plot.

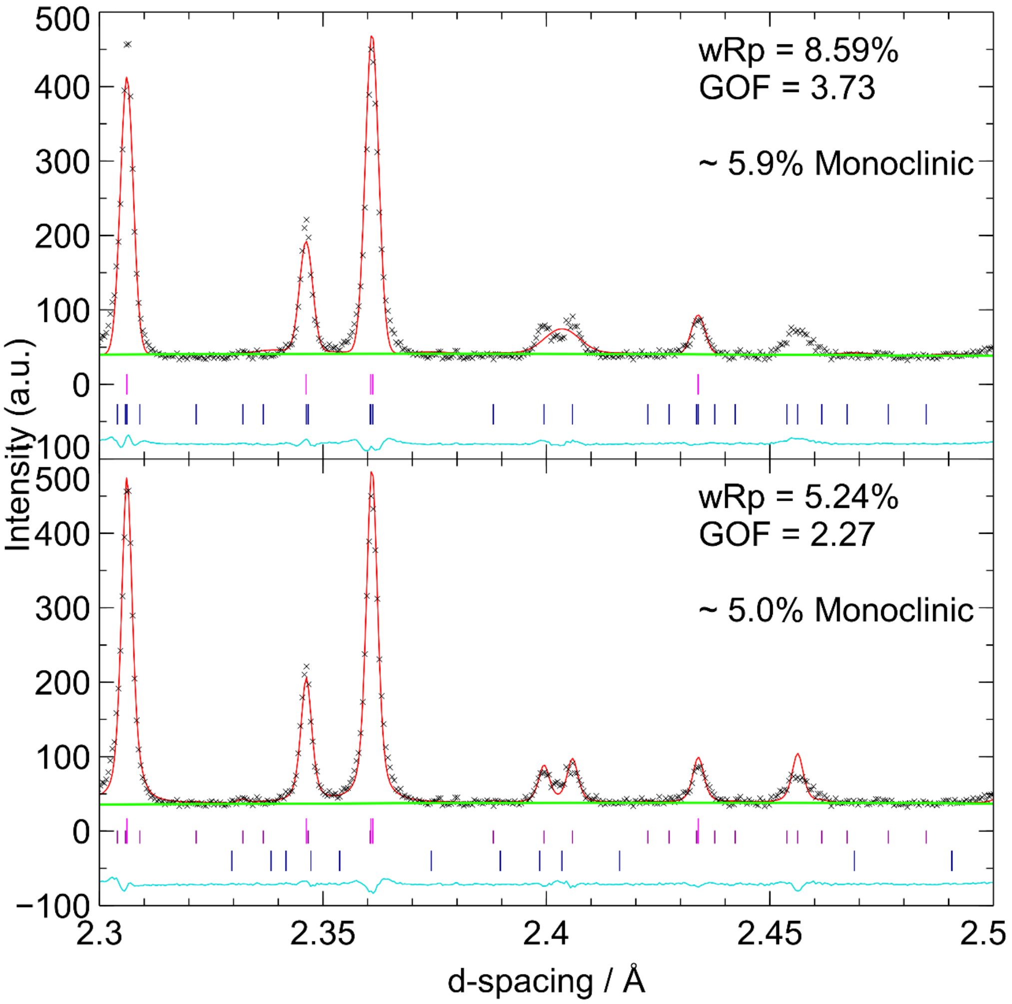

Figure 4.3: Comparison of two-phase refinements for HRPD detector bank 1 (323 K) with (bottom) and without (top) a modulation in the a axis. Observed data is shown as black crosses and the calculated pattern as a red line. Green background and cyan difference curves are also shown. The calculated main reflections for the orthorhombic (magenta) and monoclinic (dark blue) phases are shown under each fitted dataset, with satellite reflections for the modulated orthorhombic phase being shown as smaller magenta ticks.

It is noted that performing a two-phase Rietveld refinement with a 3D+1 incommensurate structure is somewhat more complicated than one which concerns just basic 3D models. Attempts to refine the $Cmc2_1(\alpha00)0s0$ phase 'from scratch' (*i.e.,* atomic modulation function (AMF) Fourier coefficients, modulation vector, etc.) or with estimated starting parameters were always unsuccessful – refinements were unstable and failed to converge or produced unreasonable results. In order to perform a successful two-phase refinement, it was found necessary to first only refine the $Cmc2_1(\alpha00)0s0$ phase.

The starting parameters for this phase were taken from refinements of higher temperature datasets (above $T_{m\text{-}o}$, where only a single-phase refinement is necessary) and the refinement was heavily damped. This allowed the $Cmc2_1(\alpha00)0s0$ phase to first be refined to a reasonable model without the potential influence of monoclinic reflections. The monoclinic phase could then be introduced in the next refinement and produced an improved fit with phase fractions similar to that decerned from previous refinements with only basic 3D phases.

Refining a modulated structure introduces numerous additional parameters which may be refined compared to a basic (unmodulated) structure. It is at the user's discretion which parameters are considered, and this can often be derived from the suspected complexity of the structure itself. It is unsurprising that this complexity is often reflected by the intricacy of the modulation function itself – a structural modulation which can be characterised by a simple sinusoidal wave is simpler than that which requires a 3rd order Fourier series to describe. This concept is straightforward but since the nature of the structural modulation was not initially known, the appropriate number of Fourier components included in the AMF's had to be determined. In order to do this, the $Cmc2_1(\alpha00)0s0$ phase was systematically refined with increasingly complex AMF's.

Table 4.2 shows the fit statistics for refinements of o-$LaTaO_4$ PND data (483 K) with the associated order of Fourier series considered. From the fit statistics, AMF's with less than 3 Fourier components do not adequately describe the modulation of the structure. It is also shown that increasing the number of components to 4 does not improve the fit. From this iterative process, the appropriate number of Fourier components to be used in refining the modulation of the $Cmc2_1(\alpha00)0s0$ phase was determined to be 3 – and this was adopted for all subsequent modulated structure refinements.

Table 4.2: Comparison of fit statistics for refinements of o-$LaTaO_4$ at 483 K. All refinements are performed with calculated satellite reflections up to the 3rd order with a modulation vector of $q \approx (0.456, 0, 0)$. Statistics represent the overall fit of the data over two banks.

Order of AMF Fourier Series	w*R*p	GOF
1	6.22	2.84
2	6.04	2.77
3	5.60	2.57
4	5.63	2.57

When comparing this information with the modulation reported for the $n = 4$ phase $Sr_2Nb_2O_7$ it is very apparent that the modulation in $LaTaO_4$ is more complex. In the study by Daniels *et al*. the uniaxial modulation of $Sr_2Nb_2O_7$ is adequately described by a simple sinusoidal wave (1st order Fourier function) - including a higher harmonics did not improve the fit and led to highly correlated parameters and unstable refinements.[8] Although a single sinusoidal wave could fit all satellite reflections present in the PND data, the 10% improvement in wRp value when using a 3rd order Fourier function was deemed significant enough that a more complex modulation should be considered. The seemingly more complicated modulation in the $n = 2$ phase compared that reported in the $n = 4$ phase $Sr_2Nb_2O_7$ is thought to be related to the thickness of the octahedral sheets and subsequent connectivity of the TaO_6^{7-} octahedra.

The complexity in the modulation found for $n = 2$ compared to $n = 4$ is best rationalised when considering the structures as a whole. **Figure 4.4** shows a side-by-side comparison of the $n = 2$ and $n = 4$ orthorhombic *Cmc*2_1 structures. The $n = 4$ Carpy-Galy phases contain a layer of interconnected BO_6 which is 4 octahedra deep and also introduces a new A-cation environment within the layer. The addition of a perovskite-like A site (the A2 site) and increased connectivity of the octahedra produces a more rigid structure than what is found in the n = 2 phases. For the $n = 2$ phase one might therefore easily imagine these layers are more flexible and prone to distortion than thicker $n = 4$ layers.

The effect of the cation sizes alone may also influence the complexity of the modulation. The Goldschmidt tolerance factor can be considered for a theoretical 3D perovskite of $LaTaO_3$ and $SrNbO_3$ to compare the predicted distortion of these structures due to cation size effects alone. The tolerance factor for $LaTaO_3$ and $BaMnF_3$ are comparable at 0.955

and 0.959. respectively, which is unsurprising given the relative similarity of their modulations. $SrNbO_3$, however, has a somewhat higher tolerance factor of 0.994, which indicates a lesser degree of size mismatch and may result in lesser structural distortion in $Sr_2Nb_2O_7$ and a subsequently more simplistic modulation, compared to $LaTaO_4$ and $BaMnF_4$.

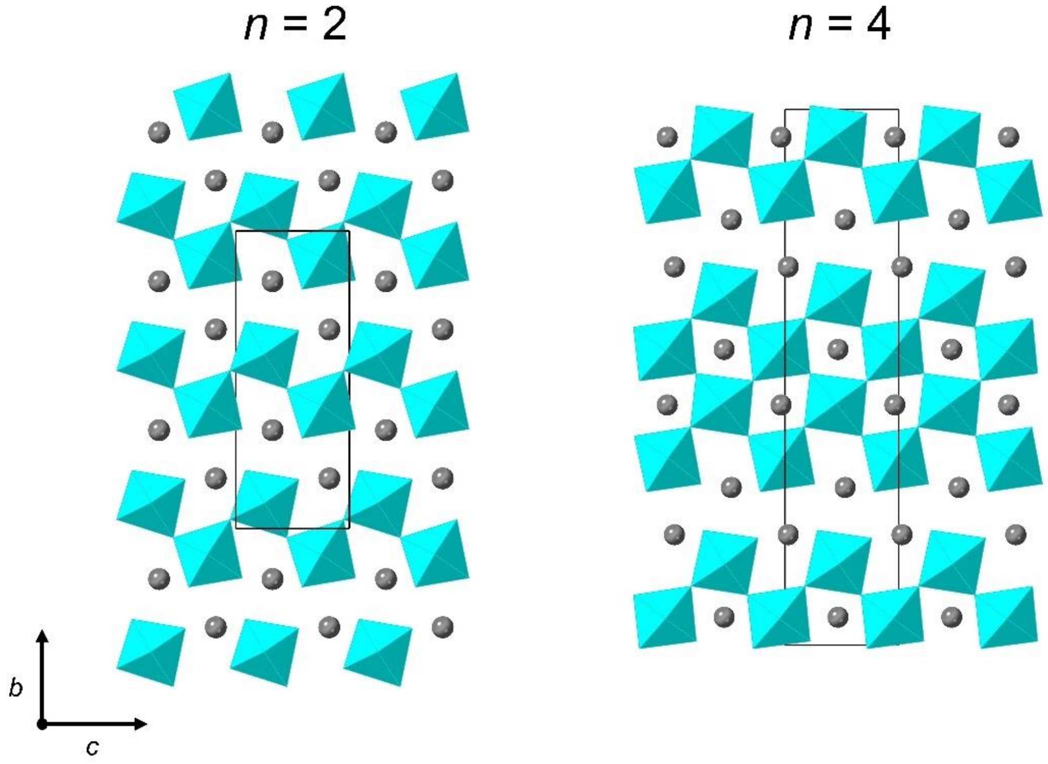

Figure 4.4: Comparison of *n* = 2 and *n* = 4 *Cmc*2₁ Carpy – Galy phases. The additional depth in the octahedral layers introduce an internal 'perovskite-like' A2 cation environment. The addition of this site and the increased octahedral connectivity is thought to contribute to a much more rigid structure.

Although the incommensurate modulation in orthorhombic $LaTaO_4$ is identified, it is important to consider why this structural feature exists. Daniels *et al.* speculate that the modulation in $Sr_2Nb_2O_7$ arises as a mechanism to resolve unusual Sr - O bond lengths which exist due to the irregular coordination of Sr^{2+} - it is logical to consider that a similar mechanism gives rise to the modulation in $LaTaO_4$.[8] In the study of $Sr_2Nb_2O_7$, the most prominent atomic displacement is the shift of the inter-octahedral Sr^{2+} cation towards and away from the octahedral layer and back towards the 'ideal perovskite position' (the position it would occupy if it was within a perovskite layer as opposed to between layers). A similar displacement of La^{3+} is observed in $LaTaO_4$.

Figure 4.5 shows a 3D, real space, representation of the IC orthorhombic phase as determined from refinement of the data at 483 K (**Figure 4.2**). As expected, the most obvious structural modulation is the displacement of the La^{3+} cations in the inter-octahedral sites. This is similar to the observation in $Sr_2Nb_2O_7$, where the A-cation is displaced from its average 'unmodulated' position, either towards the 'ideal perovskite position' or away from the octahedral layer.[8] Also shown is the complimentary tilting of the octahedra, which is not as pronounced as the displacement of La^{3+} but is mechanistically important to the improvement in the overall A site bonding environment.

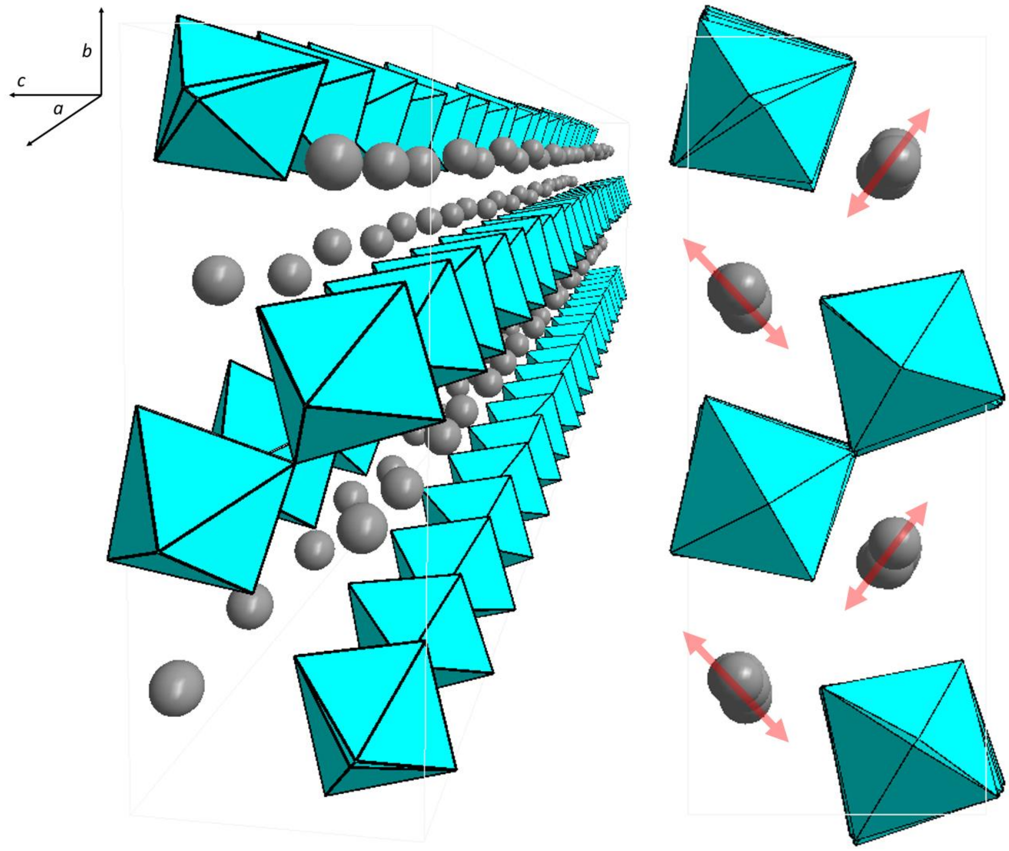

Figure 4.5: Visual representation of the modulated $LaTaO_4$ structure, projected 20 unit cells along the *a* axis (20 unit cells is an arbitrary number and was chosen for illustrative purposes only). The most prominent variation is displacement of the La^{3+} cations in and out of the inter-octahedral spaces between octahedra in the layers. This is accompanied by tilting of the TaO_6 octahedra.

Figure 4.6 also shows that there is a cooperation between the phase of each modulation in each layer. The symmetry operations of the $Cmc2_1(\alpha00)0s0$ superspace group dictate that the displacement of La^{3+} cations either side of an octahedral layer are in phase, which allows for cooperative tilting in this layer. Adjacent layers, however, have modulations which are out of phase with each other by $t + ½$. This is most easily illustrated by the approximate supercell. In the bottom layer we can identify two sets of octahedra which are essentially untilted and lie ~11 unit cells apart in *a* (the centre of which are marked by red lines) – this is our approximate supercell. The same untilted set of octahedra in the adjacent layers is shifted ~5.5 unit cells (half a supercell) in *a*.

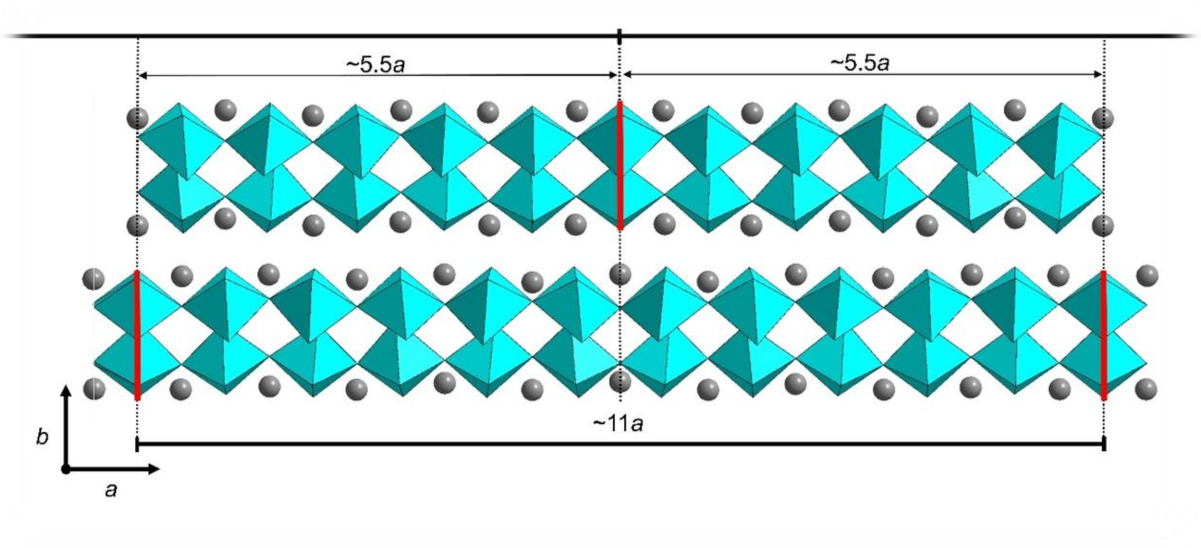

Figure 4.6: View of the modulated structure in the ab plane where the tilting pattern of the octahedra is observed to repeat after approximately 11 unit cells in *a*. This is marked with red lines indicating the most untilted octahedra in each layer. The position of the untilted octahedra in adjacent layers are shifted by half a supercell in *a*, indicating the distortions in each adjacent layer are out of phase by ½.

The out-of-phase tilting of the layers is believed to accommodate a greater degree of beneficial distortion (or at least allows the layers to pack more densely). A combination of this cooperative geometry and a better fit of the PND data ultimately led to the decision that $Cmc2_1(\alpha00)0s0$ was the most likely superspace group compared to alternatives such as $Cmc2_1(\alpha00)000$, where cooperative out-of-phase distortions do not occur between the layers.

It is easier to visualise the modulation of structural parameters as a function of the phase of the modulation wave, *t*. **Figure 4.7** shows the displacement of the La^{3+} cation from its 'basic' position within the unit cell, as a function of the phase of the modulation.

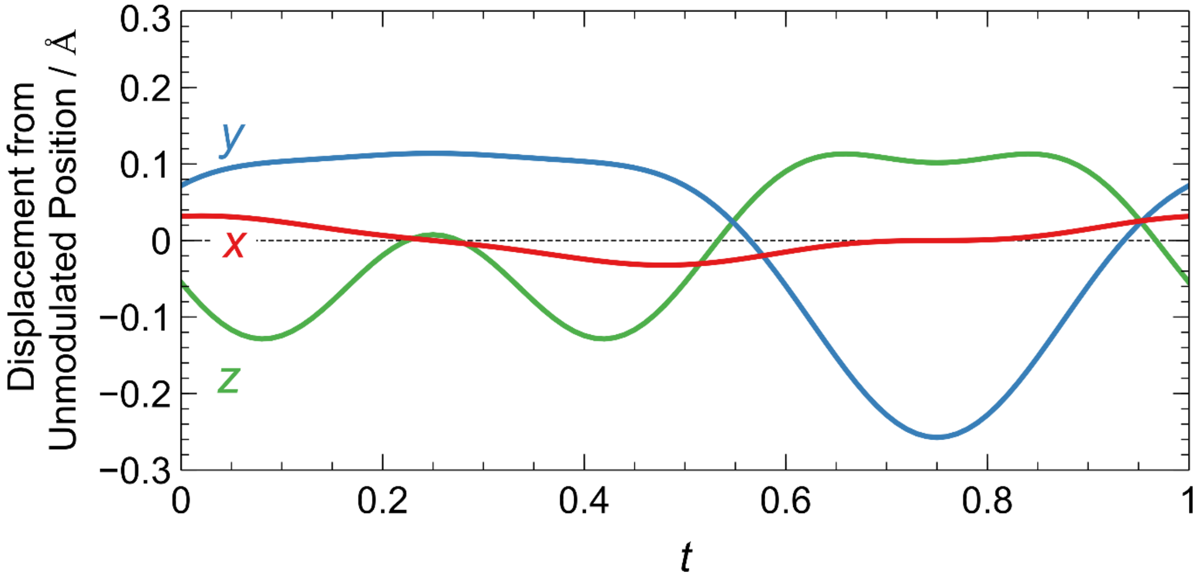

Figure 4.7: Displacement of La^{3+} cations in the *x*, *y* and *z* directions from the unmodulated position (dotted line) as a function of modulation wave phase, *t*.

As we move along the modulation vector (parallel to *x* in this case) the greatest variation in the La^{3+} position is observed orthogonal to the modulation axis, *i.e.*, the La^{3+} cation is shifting mostly in the *bc* plane (indicated by arrows in **figure 4.5**). When this is considered in terms of the overall structure it makes a great deal of sense given that the La^{3+} cations sit within the interstices between the octahedral sheets. This gives La^{3+} the greatest degree of freedom in comparison to the other atoms in the system, as it can move freely in and out of these sites without the need for any additional significant structural distortions. In contrast to this, the displacement *t*-plot shows a relatively small deviation in the *x* coordinate in comparison to *y* and *z*. This may be due to the steric hindrance of the A-cation in this axis or a more pronounced modulation of La^{3+} in *a* is simply not beneficial to its overall bonding environment.

Evidence of this modulation now becomes obvious when we re-examine the PND data presented in chapter 3. **Figure 4.8** shows a reproduction of the lattice parameter data from chapter 3 with a closer examination of the IC-C transition. Only the main reflections have been refined and the IC modulation has not been considered.

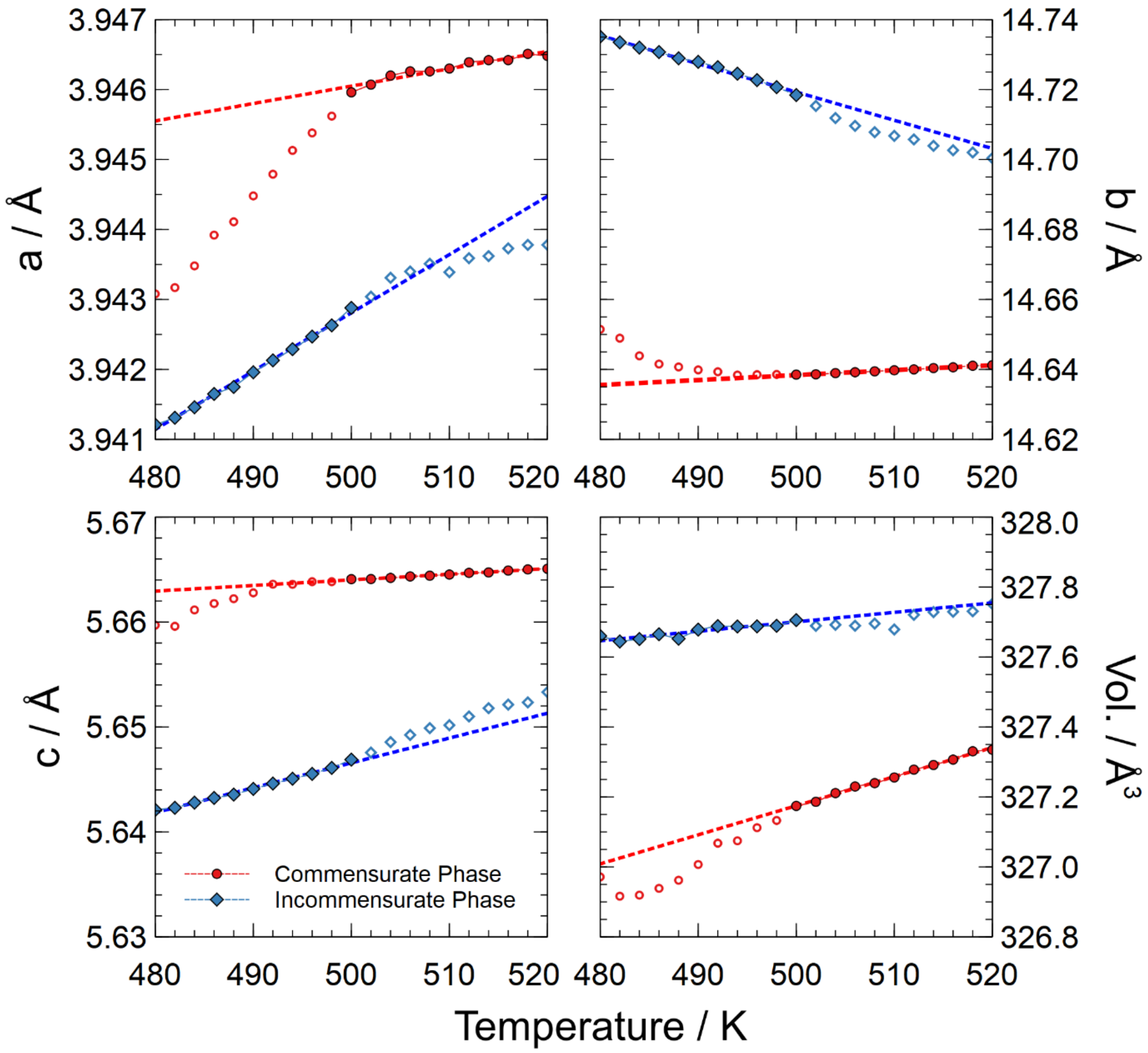

Figure 4.8: Lattice parameters of the low temperature (IC) [blue] and high temperature (C) [red] phases at the IC-C transition (483 – 523 K). Solid markers indicate data that was interpreted from regions where the phase is most prominent. Hollow markers represent regions where the phase fraction of the second phase is low, and subsequently associated values are less reliable. A linear relationship with temperature is assumed and lattice parameters are extrapolated from regions with greater confidence.

The atomic displacements introduced by the modulated structure consequently have an effect on the lattice parameters of the orthorhombic cell. As the structure undergoes a first order transition to the basic $Cmc2_1$ phase, there is a clear step change in the lattice parameters which reflects the structural distortions introduced by the modulation. **Figure 4.8** shows that the modulated phase has shorter *a* and *c* parameters, but a larger *b* parameter compared to the commensurate phase. It is unsurprising that the *a* and *c* axes behave in a similar way given the connectivity of the octahedra in the *ac* plane. The *b* axis - along which the octahedral sheets stack - is elongated in the modulated phase due to the displacement of the La^{3+} cation and the octahedral sheets, which are now corrugated in conjunction with these La^{3+} displacements. This hinders the packing of the octahedral sheets in the *b* axis. The corrugation of the octahedral sheets also accounts for the shorter *a* and *c* parameters.

The thermal expansion of each of these phases is also unique. We observe that all axes in the commensurate phase exhibit positive thermal expansion (PTE) whereas the incommensurate phase exhibits uniaxial (negative) NTE in *b*. It is no surprise that the axis which behaves differently is the stacking axis, where we have a large degree of disconnection between the octahedral layers. As discussed in chapter 3, Ablitt *at al.* rationalise the NTE exhibited by $LaTaO_4$ to the extra degrees of freedom introduced by the layering of the Carpy-Galy phases (in comparison to a standard perovskite).[14] Although this conclusion may, in part, be correct, the rationale behind their analysis may need to be re-examined as their analysis assumed a commensurate $LaTaO_4$ structure, based on the PND analysis of Cordrey *et al.*, who at the time were unaware of the incommensurate phase. As shown in **figure 4.8**, uniaxial NTE is only exhibited by the IC $Cmc2_1(\alpha00)0s0$ phase and the emergence of *b*-axis PTE observed at higher temperature by Cordrey *et al.* coincides with the newly identified IC-C transition. Therefore, the conclusion that the basic $Cmc2_1$ structure displays NTE similar to the other layered structures examined in their study is likely incorrect. The NTE is inherently linked to the IC $Cmc2_1(\alpha00)0s0$ structure and this behaviour therefore arises due to the modulation. The La^{3+} displacements are found to be larger at lower temperature so the octahedral layers pack closer together as temperature increases.

As mentioned previously, the existence of the modulation in $LaTaO_4$ is suspected to be a mechanism to improve the overall bonding environment of La^{3+}. In order to quantify the effect this, the bond valence sum of the La^{3+} cation is calculated as a function of the modulation phase – in this way every possible bonding environment in the crystal structure (based on the refined model) can be accounted for. **Figure 4.9** shows the ten shortest La – O bond distances and associated bond valence sum (BVS) as a function of *t*.

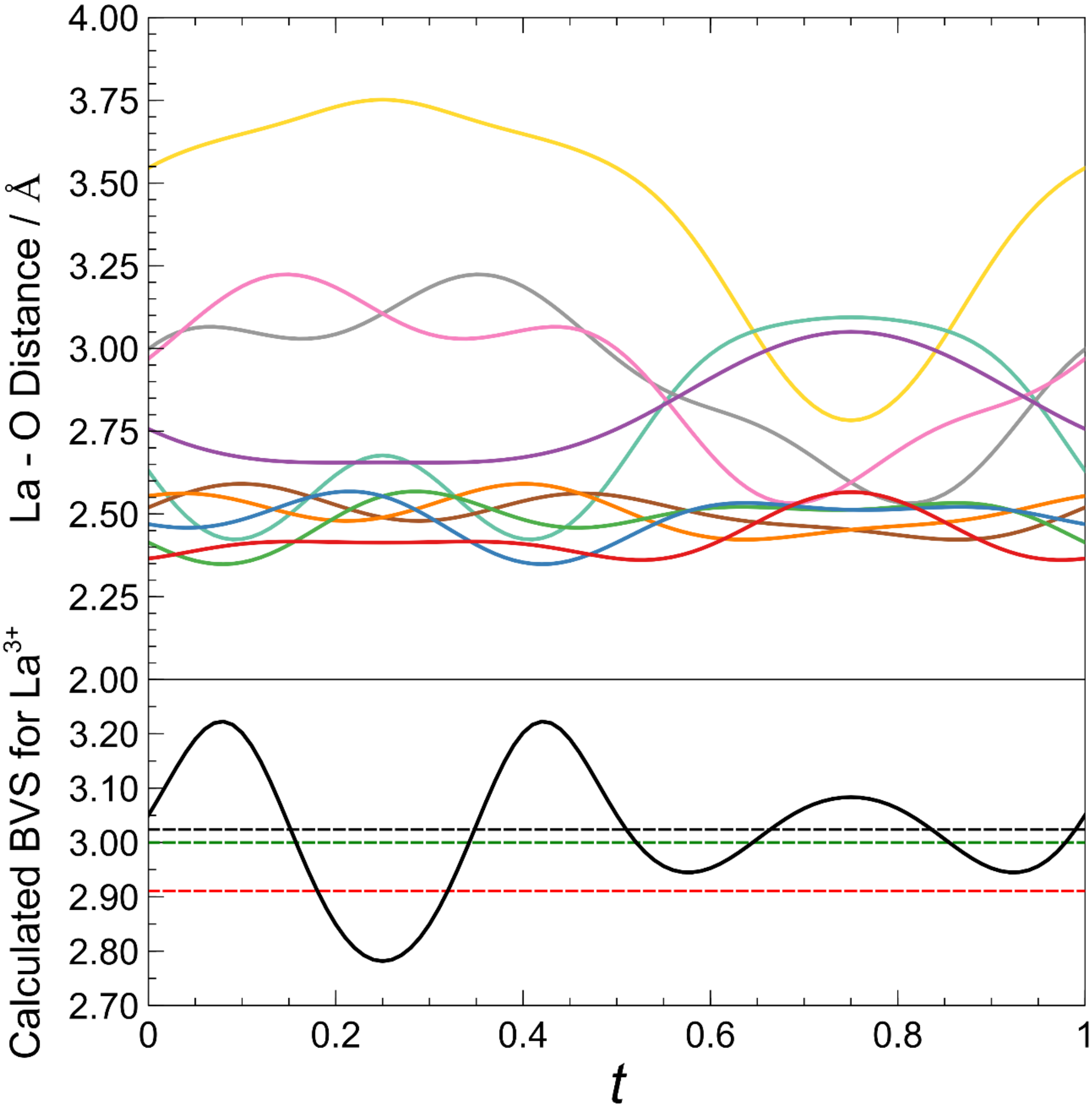

Figure 4.9: Plot of La-O interatomic distances (top) and resulting bond valence sum for La (bottom panel, black solid line) as a function of the modulation phase, *t*, obtained from the refined IC structural model at 483 K. The average valence of the La cations in the modulated structure (black dashed line) shows a marked improvement over the valence of the basic (unmodulated) $Cmc2_1$ structure (red dashed line), bringing it much closer to the ideal value of 3 (green dashed line).

Although the variation of La–O bond distances looks complex, we can easily rationalise the modulation in terms of the effect this has on the bond valence sum (BVS) of La. As the improvement of overall bonding environment is suspected to be the driving force behind the modulated structure, it is reassuring to observe that the result of each displacement which affects the various La-O bond distances is a relatively simple variation in BVS. Each curve shown in the top panel of **figure 4.9** shows a bond which was included in the BVS calculations. At first glance it may seem unusual that some abnormally long La–O bond lengths appear but when the A-cations surroundings and the observed structural modulations are considered, the necessity of their inclusion becomes apparent. **Figure 4.10** illustrates the local coordination (bonding) environment of La^{3+} and helps visualise each La–O bond in the modulated structure as well as how the bonding of La^{3+} is improved by certain structural distortions.

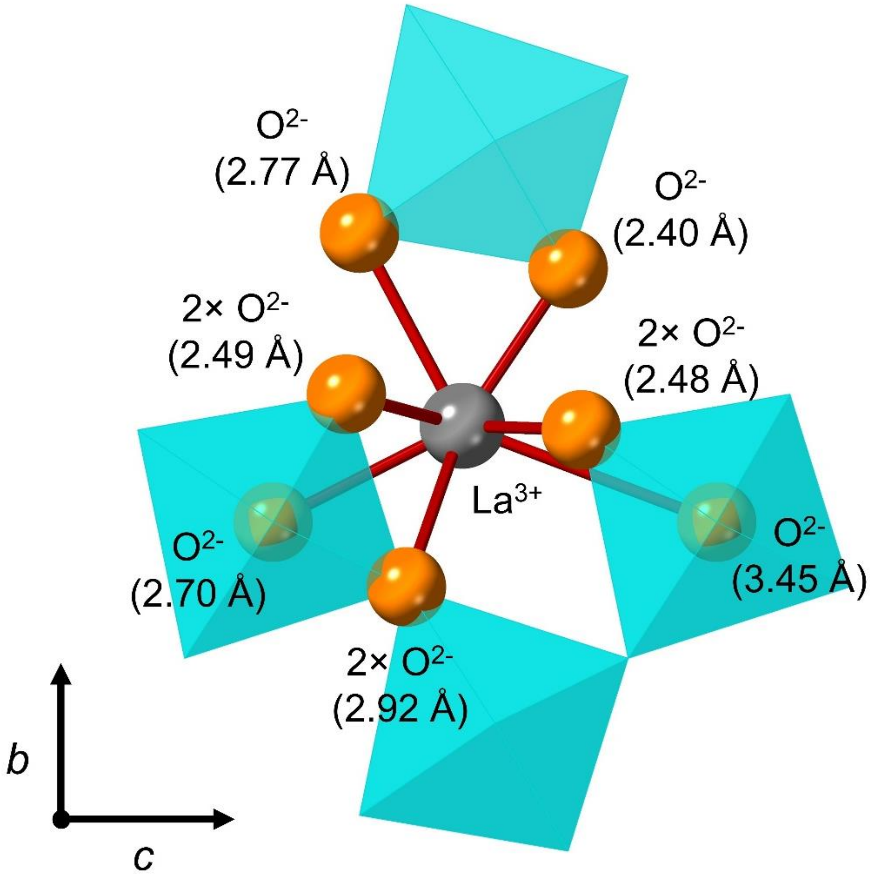

Figure 4.10: Visual representation of the suspected coordination of La^{3+} to surrounding oxygens in the unmodulated structure. It is important to remember that the La^{3+} lies in plane with the uppermost octahedra, whereas 6 octahedra are present in the bottom layer, shifted by ½ in *a*. Instances where 2× multiplicity is noted, indicate another bonding oxygen, one unit cell directly behind the one that is visible *i.e.*, belonging to the next octahedra along *a* (into the plane of the page).

For the unmodulated structure shown in **figure 4.10**, the bond from the central La^{3+} cation to the rightmost O^{2-} anion is the longest one observed (3.45 Å) and this correlates to the yellow curve in **figure 4.9**. From the unmodulated model it is hard to justify the inclusion of this bond in the BVS calculations but in the modulated structure this bond shortens significantly at some values of t (~0.75) and undoubtedly contributes to the bonding of La^{3+}. This significant shortening is due to a corrugation of the octahedral sheets, which leads to this corner sharing oxygen displacing towards the inter-octahedral site. This is of course coupled with the much more significant displacement of the La^{3+} cation towards and away from the octahedral sheet. It is not clear why, in the case of $Sr_2Nb_2O_7$, the authors have opted to include all surrounding oxygens to create a 15-fold coordination when conducting their own BVS calculations, given how exceptionally long some of these bonds are (up to 4.213 Å) and how little they would contribute.[7] Inclusion of the next five closest oxygens in BVS calculations for $LaTaO_4$ made no significant difference to the BVS *t*-plot or overall (average) valence of La^{3+}.

The resulting BVS calculations do show evidence that the modulation has optimised the bonding environment of La^{3+}. The peaks and troughs observed in the BVS show phases of the modulation where the La^{3+} BVS value oscillates above and below the ideal value of 3 (green dashed line). Although, there are some situations where the BVS shows a greater degree of deviation from the ideal value, when the average valence of La^{3+} is considered (black dashed line) it is clear that there is a marked improvement compared to that of the unmodulated structure (red dashed line). The average BVS increased from 2.91 in the basic (averaged commensurate) structure to 3.02 in the (incommensurately) modulated one. Even if we only consider how much of the modulated BVS plot lies within the range of 3 ± 0.09, we can already see a clear improvement in the bonding environment. Although the BVS value oscillates between regions where bonding improves and worsens, it ultimately positively impacts the structure as a whole - this acts as evidence of the necessity of a modulated structure to improve A-cation bonding. No simple distortion of the basic cell exists which will improve the bonding in $LaTaO_4$ without destroying the translational symmetry and adversely impacting the bonding of the neighbouring cell. The impact of the modulated structure on bonding must be considered over the whole crystal.

This analysis supports the hypothesis that the modulation in $LaTaO_4$ exists as a means of improving the bonding environment of La^{3+} in the orthorhombic phase. While many comparisons have been drawn between $LaTaO_4$ and $Sr_2Nb_2O_7$ when the suspected underlying cause for the modulation in each compound is considered, there seems to now be a small discrepancy. The BVS plot as a function of *t* for $Sr_2Nb_2O_7$ published by Daniels *et al.* shows a variation in BVS which is much smaller and also does not improve the overall bonding of the inter-octahedral Sr1 cation. In fact, the overall bonding environment of their perovskite-like Sr2 cation actually strayed further from the ideal value of 2. The modulation as described in their study, however, was hypothesised to exist as a means of alleviating unusually short Sr - O bond distances and not as a means of improving the overall bonding of the inter-octahedral Sr^{2+}.[8] As discussed earlier, the n = 4 phase is somewhat more constricted in its distortions by the extra octahedral connectivity and therefore the only beneficial modulation which can exist in this phase is one which increases the average bond length between Sr1 and its four closest neighbouring oxygens.[8] It is then assumed that the less rigid n = 2 structure allows not only the shortest La–O bonds to be lengthened (on average) but also allows for the overall bonding of the A-cation to be optimised. In addition to this, evidence discussed in the next chapter suggests that a size effect for the A-cation also contributes to the stabilisation of the IC phase and a relationship between ionic radii and $T_{\text{IC-C}}$ is presented.

4.3.2 Electron Microscopy

Refinement of the PND data allowed an average model of the atomic structure of the incommensurate phase to be constructed, where a similar modulation to other layered perovskites is observed. The structure is composed of regions of varying degrees of cation displacement with an accompanying octahedral tilt and the model, whose repeating distance spans approximately 11 unit cells in the *a* axis [$q \approx (0.456, 0, 0)$]. The first strong evidence for a modulation, however, was observed by SAED and from this data starting values for refinement of the macroscopic modulation were established.

Figure 4.11(a) shows an SAED pattern of o-LaTaO4 viewed down the [001] direction of the orthorhombic unit cell with a = 3.9349 Å, b = 14.7566 Å, c = 5.6326 Å, space group $Cmc2_1$. The main diffraction spots can be indexed onto this basic unit cell with (100) and (010) spots absent. No extra spots corresponding to a superstructure are observed along the [010] zone axis. However, some satellite spots are visible in the [100] direction. These weak spots are not at positions of simple fractions, but in segment of the distance from (000) to (200) with separations of “0.229, 0.229, 0.084, 0.229, 0.229” as shown in **figure 4.11(a)**. The value of 0.229 falls in between 0.20 (1/5) and 0.25 (1/4) and cannot be generated from a simple fraction. Therefore, these weak spots are diffraction peaks from an incommensurate superstructure.

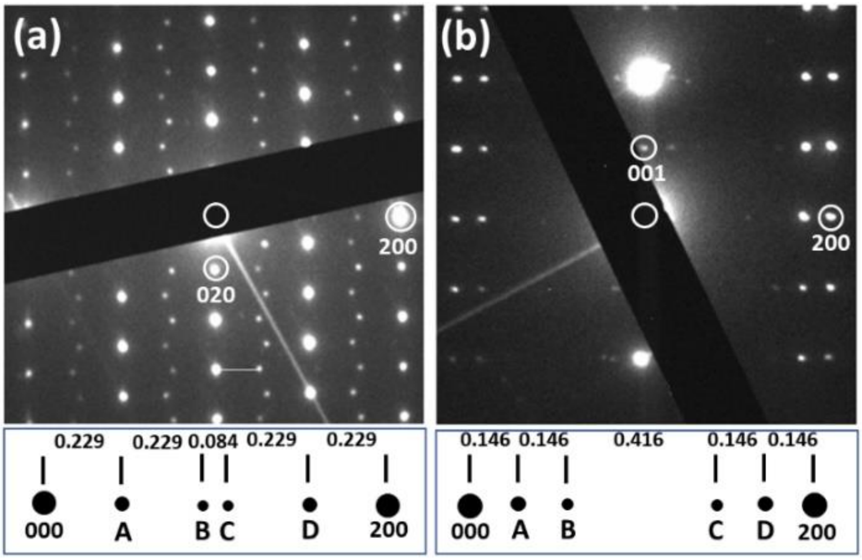

Figure 4.11: SAED patterns and HRTEM image of o-LaTaO$_4$. (a) SAED pattern of a particle view down the [001] zone axis. (b) SAED pattern of another particle on the projection of the [010] direction. The positions of the satellite spots are marked below the two SAED patterns.

If the satellite spot "A" along the [100] direction in the SAED pattern of **figure 4.11(a)** is shifted from 0.229 to 0.227, leading to a segmentation of "0.227, 0.227, 0.092, 0.227, 0.227" or simply "5, 5, 2, 5, 5", the smallest approximate superstructure is eleven-fold along this direction.

Figure 4.11(b) shows an SAED pattern from another o-LaTaO4 particle, viewed down the [010] axis. No superstructure is observed along the [001] direction, except that the originally absent (001) spot appears. Some weak satellite spots along the [100] direction are found again. However, their positions are different from those in **figure 4.11(a)**, having fractions between (000) and (200) spots, "0.146, 0146, 0.416, 0.146, 0.146". The spots "A" are at a position between 1/7 (0.143) and 1/6 (0.167), but much close to the former and so an approximate commensurate unit cell would be 7-fold along the [100] axis. The discrepancy between each of these patterns suggests that the modulation is not locally homogeneous – the macroscopic modulation observed by PND is not entirely applicable to the local structure.

With this evidence of an inhomogeneous modulation, the model which has been constructed from PND data must (for now) be disregarded. The continuous nature of this model is incompatible with the discontinuous local structure that is observed from electron microscopy and a new origin of the incommensuration is considered. To understand the formation mechanism of the incommensurate superstructure, a commensurate superunit cell with reasonable dimensions can be considered. Such a hypothetical unit cell must contain two or more types of blocks (or two superstructural vectors) - since single blocks can only form a commensurate superstructure. If these blocks are randomly arranged along a certain direction, diffused diffraction patterns are observed. The situation is similar to disordered layered defects.[15] If the blocks are perfectly ordered, a commensurate superstructure forms. If they are partially ordered, the superstructure becomes incommensurate.[16,17] It is then proposed that the incommensurate superstructure observed in $LaTaO_4$ can be broken down into a partial ordering of two sub units, which are supercells constructed from the basic $Cmc2_1$ cell.

It can be assumed that the incommensurate structure can be attributed to partial ordering of two blocks, M and N, with dimensions of 6*m* and 5*m*, where *m* is a half of the basic unit cell parameter *a*. These relatively stable blocks can then be connected to each other in different manners along the *a* axis, with very small difference in lattice energy, e.g. M-M, N-N and M-N. When ordering from 2M and 2N blocks occurs, an 11-fold commensurate superstructure can be constructed (the approximate value obtained from PND). The appearance of the satellite spots may be attributed to a combination of diffraction peaks from M and N. As a general property of incommensurate structures, the ratios of the blocks, M : N and their permutations in different particles or in different areas of a particle would be variable – hence we observe a variation in inter-spot distances (and therefore modulation vector) based on the area of sample analysed.

Information on the periodicity of the structure could also be extracted from HRTEM images collected for the incommensurate phase. **Figure 4.12** shows a repeating pattern of light and dark stripes propagating along the [100] direction – parallel to the modulation vector – which shows the periodicity of the structural units proposed (M and N). The image shows blocks along the [100] direction consistent with the description above. Careful measurement revealed three different thicknesses of the blocks, 11.7, 13.8 and 15.6 Å, which could be expressed as M (6*m*), O (*7m)* and P (8*m*), where *m* = *a*/2. The appearance of the satellite diffraction spots can be attributed to a combination of diffraction peaks from these blocks. The hypothetical seven-fold superunit cell discussed earlier may contain 2 × O or M + P blocks. In the real incommensurate structure, more blocks with partial ordering may exist. Therefore, when different areas to create FFT patterns are chosen, the observed satellite spots shift from one area to another. The proposed commensurate superstructure consisting of blocks, which contain elements of structural origin, is a simplified model to help understand the formation mechanism of the incommensurate superstructure.

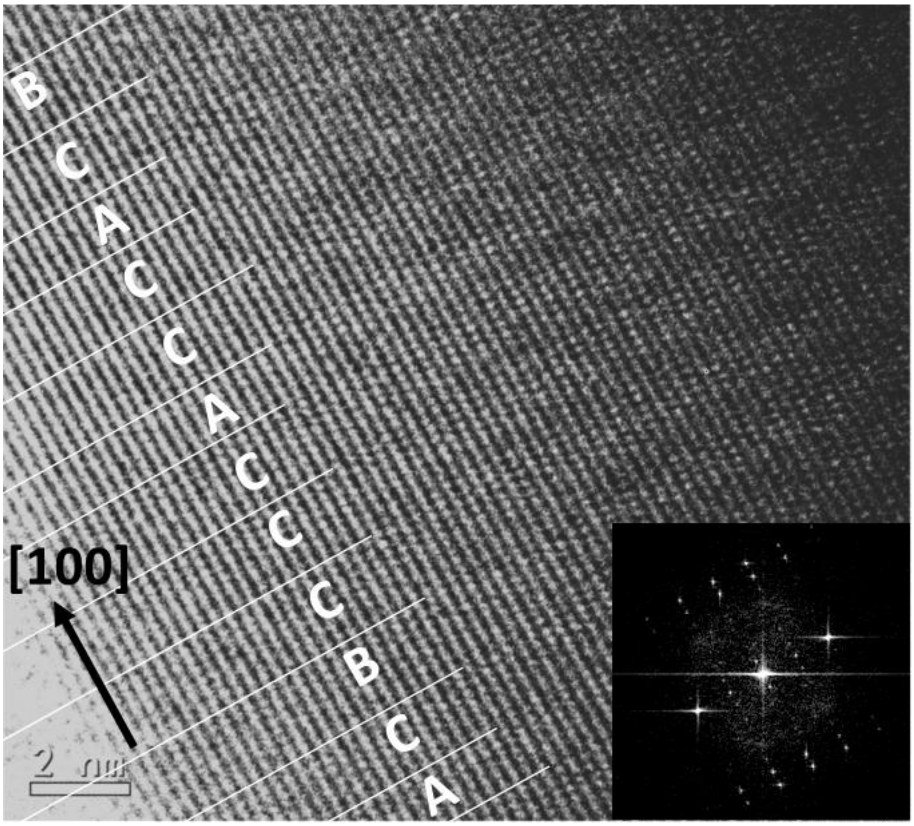

Figure 4.12: HRTEM image with fast Fourier transform (FFT) (inset) corresponding to **Figure 4.11 (b)**. The thicknesses of the blocks are marked, A: 11.7, B: 13.8 and C: 15.6 Å.

4.3.3 Structural Units

With the newest model constructing the incommensurate phase from partially ordered sub-units it is important to compare this model with the continuous modulation derived from PND data and assess its validity. Obviously with the incommensuration originating from a partially ordered structure the continuous model is not reflective of the real IC phase but can be used to elucidate the structural information which cannot be readily extracted from the SAED or HRTEM data. The most important factor in assessing the validity of each model is their consistency with each other.

Figure 4.13 shows a representation of the modulated phase produced from refinement of PND data (also shown in **figures 4.5 and 4.6**). Reassuringly, the ~11*a* supercell generated from this model can be visually broken down into the units proposed by electron microscopy and are as described previously, where they assume a thickness of 3*a* (M) and 2.5*a* (N). Despite the PND model being constrained to a continuous modulation and not being a valid representation a partially ordered structure, it can be used to identify how the M and N units can emerge from regions with distinct structural distortions. The units themselves are structural configurations which improve the bonding of La^{3+} almost equally, in the same manner as described before, and alternate along the polar *a* axis; the tilting of the octahedra would inevitably generate lattice strain in the octahedral layers and a natural way to release such a strain is that, over a certain distance, the octahedral titling changes its manner. The approximate tilt direction of each octahedra is denoted by red arrows in **figure 4.13** and this shows how the tilting pattern (and La^{3+} displacements) define the structural unit.

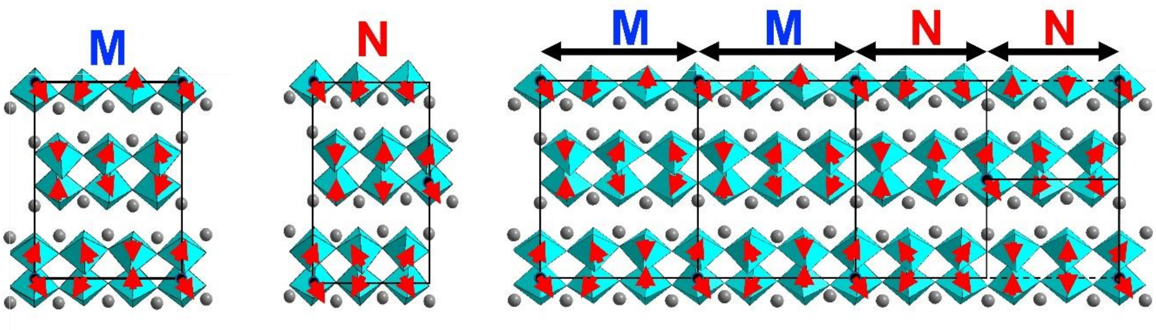

Figure 4.13: Suggested structural units built from diffraction data. Incommensuration originates from the partial ordering of the M and N supercells in the *a* axis. The M unit is a 3× expansion of the basic cell in *a* and N unit is a 2.5× expansion. Red arrows denote the rough tilting direction of the TaO_6 octahedra and highlight equivalent octahedra that are created by translational symmetry.

The nature of the tilting in each of these units also dictate certain rules that are followed when these units order and this is illustrated in **figure 4.14**. M units stack along the *a* axis freely and are related by translational symmetry in *a*. N units, however, dictate that neighbouring units are also shifted by ½ unit cell in *b* - though the tilt system also forbids any stacking of different unit cells in *b* and so prohibits any supercells being generated in this axis. Because these new supercells also do not have any implications for the *c* axis, it can be thought that these units will form ‘slabs’ of supercells which stretch infinitely in *b* and *c*, while partially ordering in *a*. This ‘slab’ nomenclature is adopted from a study of strontium barium niobate, whose incommensurate structure is reported to be compiled of similarly ordered ‘slabs’ of supercells.[18] These slab-like units can theoretically have any thickness in *a* but HRTEM images in the present work suggest they have very limited ordering and extension, due to generation and relaxation of the lattice strain.

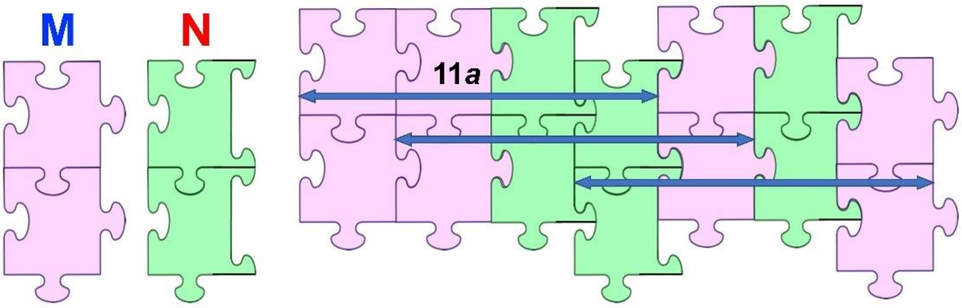

Figure 4.14: Illustration of the relationship between each block and adjacent layers; where M blocks will stack directly along *a* and N blocks will shift adjacent blocks by ½ unit cell in *b*. A combination of two of each block yields an 11*a* supercell, a close approximate of the incommensurate wave vector observed by PND.

As previously mentioned, comparisons can also be drawn with $n = 4$ $La_2Ti_2O_7$, which has an incommensurate layered perovskite structure which is made up of different structural units – similar to that suggested here for $LaTaO_4$.[9] Despite the similarities, $La_2Ti_2O_7$ has been shown to have a continuous displacement of La and accompanying tilt of octahedra, which over the course of the modulation wave results in a combination of the basic high temperature and low temperature unit cells stacking alongside each other in the *a*-axis.[9] For $LaTaO_4$ this would mean the IC phase would consist of units of basic orthorhombic and monoclinic phases. There is no evidence of this from this study and hence this possibility has not been pursued further.

4.3.4 Temperature Dependence of *q*

From refinement of the neutron data, it is observed that the modulation has a clear temperature dependence. Refinement of *q* at various temperatures shows the fractional coordinate of the modulation in a^*, σ_1, decreases over the measured temperature range (**figure 4.15**). The approximate commensurate supercell at 483 K is 11*a*, whereas at 323 K the approximate supercell is 21*a*. This trend can be interpreted to suggest a greater degree of ordering as we increase in temperature and approach the transition into the commensurate HT phase. At temperatures close to the transition, shorter acquisition times and resulting poorer signal-to-noise ratio in the diffraction data, coupled with decreasing intensity of the satellite peaks, means accurate fitting of the satellite peaks is increasingly difficult but still give values consistent with this trend.

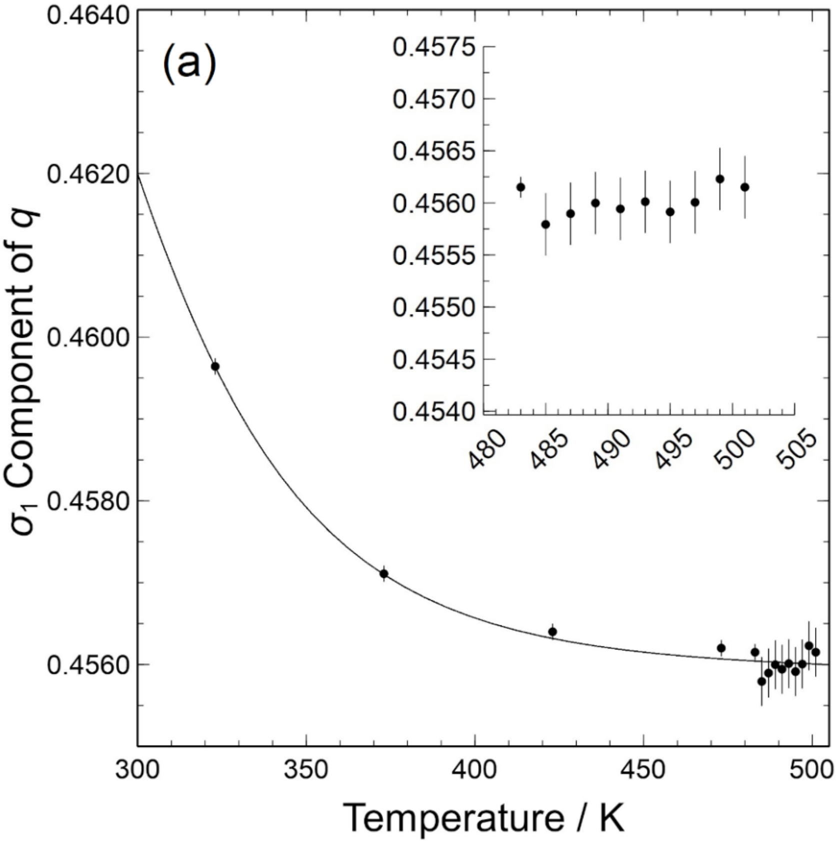

Figure 4.15: Plot of the σ_1 component of the modulation vector as a function of temperature. As temperature increases the overall repeating distance of the structure is increasing in real space. This trend is seemingly continuous but more incremental measurements would be needed to rule out the possibility of a 'Devil's staircase'.

This shows the (apparently) continuous relationship between the modulation and temperature, where decreasing temperature sees the value of q increase (the repeating distance in real space therefore decreases). It is noted that some previous studies of $BaMnF_4$ have misinterpreted a similar relationship between temperature and q, where a 'Devil's staircase' was only revealed when studying single crystals of higher quality than that of previous investigations.[4] Powder methods obviously lack the same accuracy as analysis of a single crystal and so the seemingly continuous relationship seen in **figure 4.15** should be taken as an approximation of the temperature dependence of q. A characteristic jump between lock-in values may not be evident in the current data and hence the possibility of a 'Devil's staircase' should be investigated further in future work.

4.4 Summary and Conclusions

Re-examination of $LaTaO_4$ by electron microscopy and variable temperature powder neutron diffraction reveals that the orthorhombic $Cmc2_1$ structure is incommensurately modulated below 483 K. On heating, the material then undergoes a transition to a commensurate $Cmc2_1$ structure. Neutron diffraction data indicates the overall IC modulation is best described as q = (~0.456, 0, 0) (at 483 K) resulting in the four-dimensional super-space group $Cmc2_1(\alpha00)0s0$. Although this approximate cell doubling in *a* is reminiscent of that observed in isostructural $BaMnF_4$ [19], it is important to note the alternate space group settings: in $BaMnF_4$ the modulation occurs along the polar axis, whereas in $LaTaO_4$ the modulation is orthogonal to the polar axis and hence closer comparisons can be drawn with the modulation of the n = 4 oxides such as $Sr_2Nb_2O_7$. The origin of the modulation may be similar to that in $Sr_2Nb_2O_7$, whereby the position of the inter-octahedral A-cation is modulated as a means of improving the overall bonding environment. In contrast to $Sr_2Nb_2O_7$, however, $LaTaO_4$ does not have the same continuous modulation of atomic positions incommensurate to the basic unit cell but instead the incommensuration arises from disordered stacking of larger structural units in *a*. Models for these units, M and N, have been proposed as 3*a* and 2.5*a* supercells, respectively, to demonstrate the principle of the formation of the incommensurate superstructure. Observation of the modulation vector at varying temperature shows a reduction in the magnitude with increasing temperature, suggesting that the ordering of the M and N units improves as the IC-C transition is approached.

4.5 References

1. Eibschütz, M., Guggenheim, H. J., Wemple, S. H., Camlibel, I. & DiDomenico, M. Ferroelectricity in $BaM^{2+}F_4$. *Phys. Lett. A* **29**, 409–410 (1969).

2. Shimamura, K. *et al.* Ferroelectric Properties and Poling of $BaMgF_4$ for Ultraviolet All Solid-State Lasers. *Appl. Phys. Lett.* **89**, 3–6 (2006).

3. Cox, D. E., Shapiro, S. M., Cowley, R. A., Eibschütz, M. & Guggenheim, H. J. Magnetic and Structural Phase Transitions in $BaMnF_4$. *Phys. Rev. B* **19**, 5754–5772 (1979).

4. St-Gregoire, P. *et al.* On the Incommensurate Phase in $BaMnF_4$: A Neutron Scattering Study. *Ferroelectrics* **53**, 307–310 (1984).

5. Hidaka, M., Scott, J. F. & Storey, J. S. Energy Dispersive X-ray Diffraction Study of Structural Phase Transitions in $BaMnF_4$. *Phys. B+C* **123**, 291–299 (1984).

6. Scott, J. F., Habbal, F. & Hidaka, M. Phase Transitions in $BaMnF_4$: Specific Heat. *Phys. Rev. B* **25**, 1805–1812 (1982).

7. Hidaka, M., Nakayama, T., Scott, J. F. & Storey, J. S. Piezoelectric Resonance Study of Structural Anomalies in $BaMnF_4$. *Phys. B+C* **133**, 1–9 (1985).

8. Daniels, P. *et al.* The Incommensurate Modulation of the Structure of $Sr_2Nb_2O_7$. *Acta Crystallogr. Sect. B Struct. Sci.* **58**, 970–976 (2002).

9. Ishizawa, N., Ninomiya, K. & Wang, J. Structural Evolution of $La_2Ti_2O_7$ at Elevated Temperatures. *Acta Crystallogr. Sect. B Struct. Sci. Cryst. Eng. Mater.* **75**, 257–272 (2019).

10. Von Dreele, R. B. & Larson, A. C. General Structure Analysis Sytem (GSAS). Los Alamos Natl. Lab LAUR, 86–748 (1994).

11. Toby, B. H. EXPGUI , a graphical user interface for GSAS. J. Appl. Crystallogr. 34, 210–213 (2001).

12. Petříček, V., Dušek, M. & Palatinus, L. Crystallographic Computing System JANA2006: General features. Zeitschrift für Krist. - Cryst. Mater. 229, (2014).

13. Hidaka, M. *et al.* Incommensurate Cooperative Tilting Modes of MnF_6 Octahedra Related to the Structural Phase Transitions in $BaMnF_4$. *Phase Transitions* **73**, 503–522 (2001).

14. Ablitt, C., Craddock, S., Senn, M. S., Mostofi, A. A. & Bristowe, N. C. The Origin of Uniaxial Negative Thermal Expansion in Layered Perovskites. *npj Comput. Mater.* **3**, 44 (2017).

15. Zhou, W. *et al.* A study of the Structural Series in the TlCaBaCuO Superconducting System. *J. Solid State Chem.* **88**, 193–200 (1990).

16. W. Zhou, D. A. Jefferson, J. M. T. Defect Fluorite Structures Containing Bi_2O_3: The System Bi_2O_3 -Nb_2O_5. *Proc. R. Soc. London. A. Math. Phys. Sci.* **406**, 173–182 (1986).

17. Zhou, W. Microstructures of Some Bi-W-Nb-O phases. *J. Solid State Chem.* **163**, 479–483 (2002).

18. Bursill, L. A. & Lin, P. J. Incommensurate Superstructures and Phase Transition of Strontium Barium Niobate (SBN). *Acta Crystallogr. Sect. B Struct. Sci.* **43**, 49–56 (1987).

19. Cava, R. J. & Roth, R. S. The Structure Analysis of $LaTaO_4$ at 300 °C by Neutron Powder Profile Analysis. *J. Solid State Chem.* **36**, 139–147 (1981).

5 Chapter 5: A-site Doping of $LaTaO_4$

5.1 Introduction

In previous chapters the existence of an incommensurate orthorhombic phase of $LaTaO_4$ has been explored in detail; this IC phase had not been identified in previous studies despite $LaTaO_4$ exhibiting a dielectric anomaly at high temperature (well above the normal monoclinic – orthorhombic transition).[1,2] Even without the knowledge of this intermediate incommensurate orthorhombic phase, the study by Cordrey *et al*. demonstrated that samples which had been stabilised as the monoclinic polymorph by 10% Nd^{3+} doping (*i.e.*, $La_{0.9}Nd_{0.1}TaO_4$) exhibited a 150 K increase in the monoclinic – orthorhombic transition temperature.[1] The stabilisation of the monoclinic phase to higher temperatures would be expected to be a size effect – introducing smaller cations into the A-sites decreases the average size and so the higher density monoclinic (and IC orthorhombic) phase is favoured – in essence a “chemical pressure” effect. In light of the confirmed presence of the IC orthorhombic phase, it is logical to explore the implications a smaller A-cation may have on the modulated structure, especially as the incommensuration is hypothesised to exist as a product of irregular geometry in order to satisfy under-bonding of the A-site cation.

In this chapter, the relationship between the average A-cation radius and the stabilisation of the monoclinic and IC orthorhombic phases is explored. A series of samples doped with smaller A-site cations are synthesised in the monoclinic polymorph as described in previous chapters, according to the formula: $La_{1-x}Ln_xTaO_4$ where Ln = Ce^{3+}, Pr^{3+} and Nd^{3+}, and with $0 \leq x \leq 0.3$. This series exploits the lanthanide contraction with ionic radius decreasing with increasing Z across the lanthanide series and hence the size mismatch between the A-cation and the inter-octahedral site volume increases. Each of the dopants of interest should be capable of occupying the A-site, given each of $LnTaO_4$ (Ln = La^{3+}, Ce^{3+}, Pr^{3+}, Nd^{3+}) assumes the same monoclinic $P2_1/c$ Carpy-Galy structure. In general, compounds of Ln = La – Pr will form the monoclinic this phase, whereas Ln = Nd – Lu will form monoclinic fergusonite type structures.[3–5] The limit for the solid solution of $La_{1-x}Nd_xTaO_4$ forming the Carpy-Galy structure is not known and has not been explored in this investigation. If the stabilisation of the monoclinic phase is purely a size-driven effect, plotting the transition temperatures as a function of average ionic radius for all series of doped structures should yield a relatively well correlated linear trend. This appears to be the case for the Pr^{3+} and Nd^{3+} doped materials but, counterintuitively, the Ce^{3+} series shows an unusual relationship between doping concentration and transition temperature (despite Ce^{3+} being most comparable in size to La^{3+}). X-ray photoelectron spectroscopy suggests that doped Ce^{3+} cations readily oxidise and introduce interstitial oxygens into the structure, which may contribute to the unusual behaviour of the $La_{1-x}Ce_xTaO_4$ series.

5.2 Methods

All materials in this chapter were produced using basic ceramic synthesis. Stoichiometric amounts of precursor oxides were ground together with a mortar and pestle until a homogeneous mixture was produced – Nd_2O_3, Pr_2O_3 and $Ce(NO_3)_3$ were used as sources of dopant Ln^{3+} cations. To ensure variations in structure / composition were not affected by synthetic conditions, all samples were produced under the same conditions. As the insertion of smaller A-cations has been found to direct the formation of the monoclinic polymorph, samples were synthesised under conditions which also favoured formation of this phase in $LaTaO_4$, as outlined in previous chapters (pellets were pressed under 30,000 psi isostatic pressure then annealed for 6 hrs at 1650 °C). This ensured there was a much smaller degree of monoclinic/orthorhombic phase coexistence at room temperature and all three phases of interest could be examined, namely $P2_1/c$, $Cmc2_1$ (IC) and $Cmc2_1$ (C).

Structural characterisation was conducted by in-house PXRD. Room temperature diffraction data was collected over a range of 5 to 70° 2θ for 1 hour (monochromated Cu-$K\alpha_1$ radiation). Variable temperature PXRD data was collected (Mo $K\alpha_1$ / $K\alpha_2$ radiation) at 30 K intervals over appropriate temperature ranges which covered all expected phase transitions with data collected over 5 to 35° 2θ for 1 hour at each temperature. Each data set was refined using GSAS-II and only a basic (unmodulated) structure was considered for orthorhombic phases. (Note that in any case the satellite reflections associated with the IC phase are not readily observed by PXRD and so refinement of a modulated structure was not possible).

X-ray photoelectron spectroscopy (XPS) data was collected on 10mm, as-annealed ceramic pellets using a ESCA300 X-Ray Photoelectron Spectrometer using as an excitation source a monochromatic Al anode ($K\alpha$ = 1486.6 eV), operated at 12 kV, 200 W; pass energy 150 eV. Data was processed using Casa XPS version 2.3.22PR1.0.[6]

5.3 Results

5.3.1 Room Temperature PXRD

All A-cation doped samples were successfully synthesised using the methods outlined above with little orthorhombic phase present at room temperature. **Figure 5.1** shows the collected PXRD patterns for all prepared compositions of $La_{1-x}Nd_xTaO_4$ (x = 0 to 0.3) as an example.

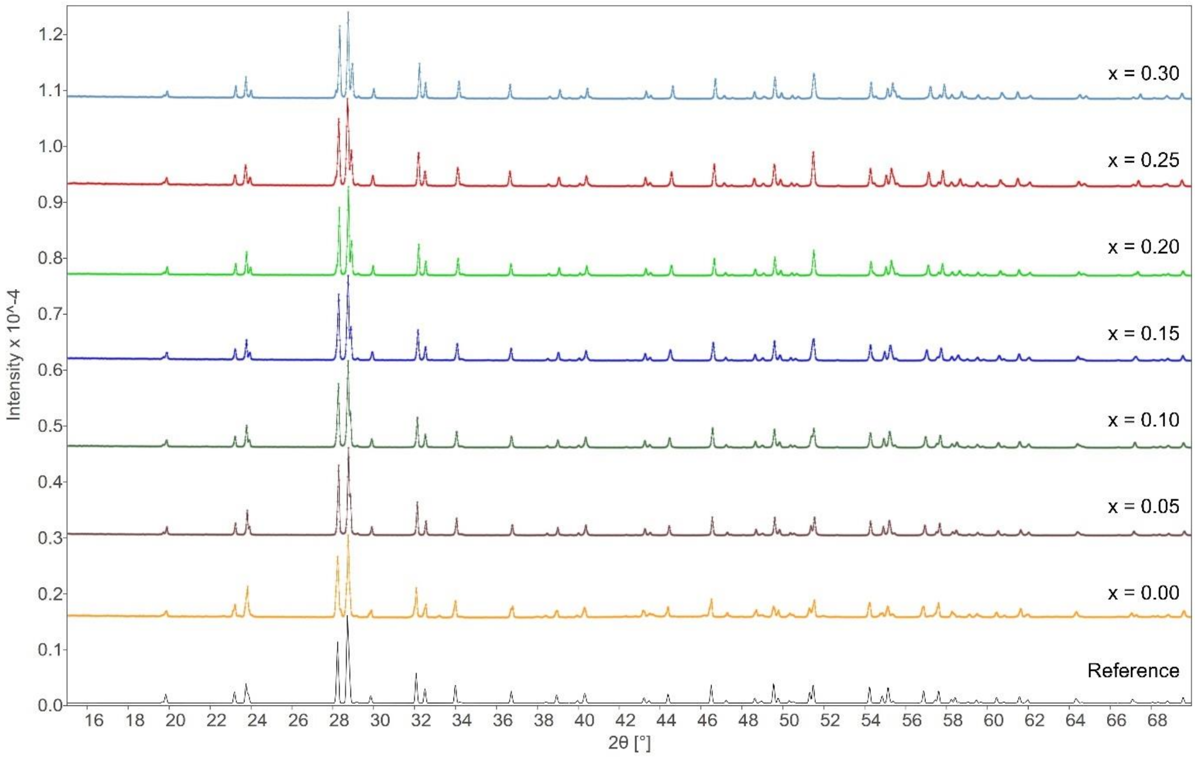

Figure 5.1: Diffraction patterns for all samples of $La_{1-x}Nd_xTaO_4$ ($0 \leq x \leq 0.3$) at room temperature. All samples assume the $P2_1/c$ phase with no detectable orthorhombic phase present.

Each of these patterns can be fitted by the basic $P2_1/c$ model with very similar quality of fit and it can easily be seen from visual inspection that no major structural change is induced by increasing levels of Nd^{3+} doping – all peaks can be accounted for by the monoclinic model. This is observed for all three dopants: Nd^{3+}, Pr^{3+} and Ce^{3+}. It is unsurprising that the introduction of smaller A-cations into the structure causes a contraction of the lattice parameters (**figure 5.2**).

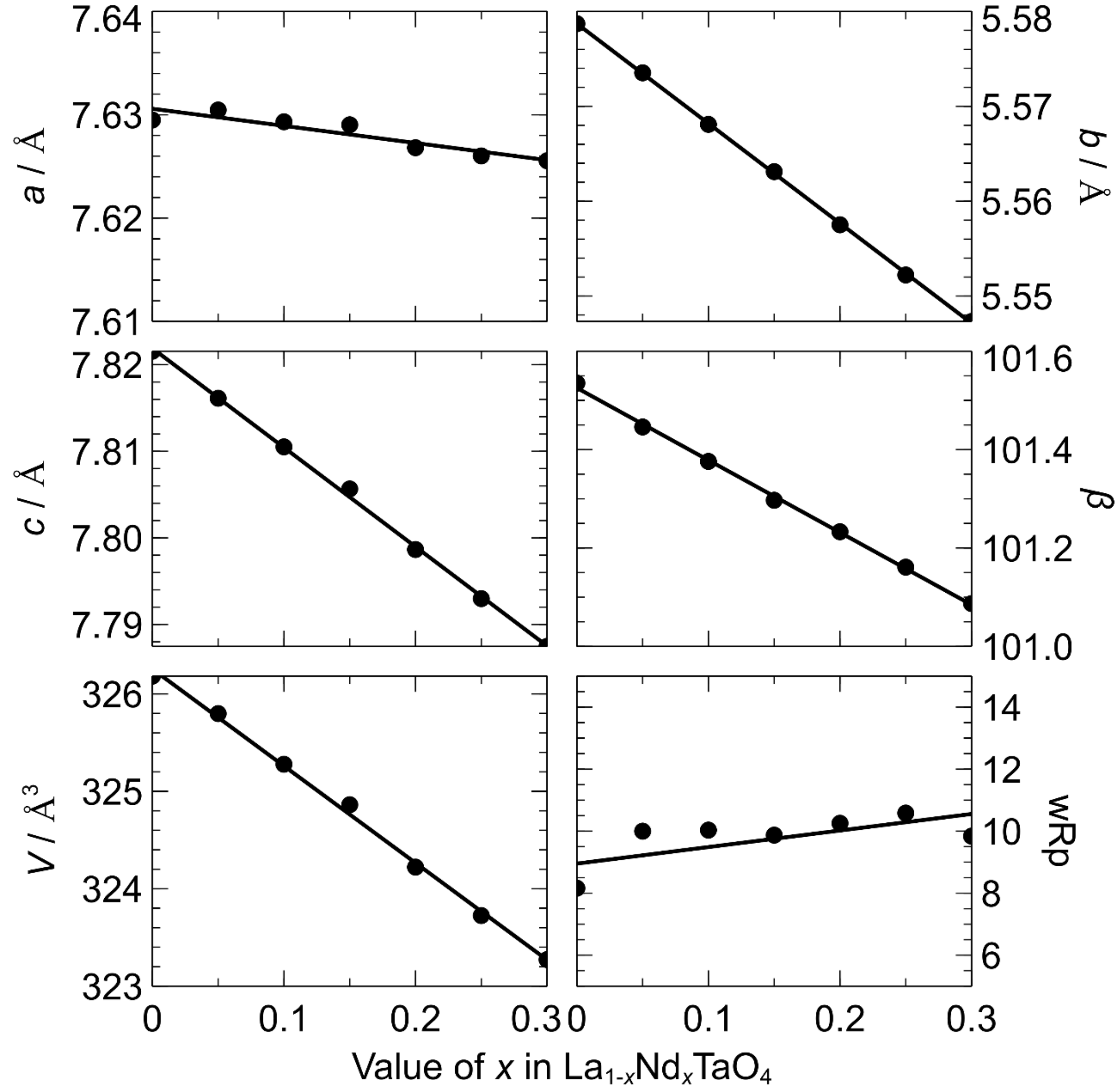

Figure 5.2: Lattice parameters for $La_{1-x}Nd_xTaO_4$ as a function of dopant concentration, x ($0 \leq x \leq 0.3$). Higher concentrations of the smaller Nd^{3+} A-cation in the structure causes the lattice parameters to contract. Although all diffraction peaks are accounted for by the $P2_1/c$ model there is a small deterioration in the overall fit of the data (wR_p increases). Error bars are included but are smaller than the datapoint.

As smaller A-cations are introduced into the structure a similar degree of contraction of the *b* and *c* parameters is observed, which is undoubtedly due to the interconnectivity of the TaO_6 octahedra in this plane. The *a*-axis does not share this same interconnectivity – the octahedral sheets stack in *a* in the $P2_1/c$ phase – and consequently the *a* parameter behaves slightly differently in that the degree of contraction is less pronounced.

A similar variation in lattice parameters as a function of *x* is observed for all investigated dopant cations – each smaller A-cation causes the unit cell to shrink anisotropically in a similar way. The strong correlation between the dopant concentration and lattice parameters is a reassuring sign that each of the smaller cations are being incorporated into the A-site. In order to determine if the reduction in lattice parameters is purely a size effect, the lattice parameters were plotted as a function of average A-cation radius (shown in **figure 5.3**). The lattice parameters of all series of solid solutions follow a linear trend of contraction as the average atomic radius decreases (*i.e.*, as dopant concentration increases).

It is unclear exactly why the *a* parameter is affected so much less than the *bc* plane, but it could be speculated that the degree of octahedral tilting is greatly affected by the A-cation size (more corrugated sheets would contract the *bc* plane) and the resulting increased tilting prevents the octahedral sheets from packing efficiently in *a*. Structures derived from the PXRD data have shown no correlation between the octahedral rotations (*e.g.* tilt angle) and the dopant concentration, but this is likely due to the limitations of x-ray diffraction, specifically identification of oxygen positions. It is therefore difficult to confirm whether the nature of the octahedral rotation is affecting the *a* parameter but the contraction of the *bc* plane may be enough to imply there is a greater degree of rotation present. With the suggestion of a modulated structure from Raman data presented in chapter 3, the contraction of the unit cell may also be influenced by an incommensuration. As it is hypothesised that the incommensuration is generated from a cation / site size mismatch, it is logical to surmise that smaller A-cations are driving increased corrugation of the octahedral sheets in the form of some structural modulation but confirming this would require much more sensitive characterisation techniques such as neutron diffraction and/or electron microscopy.

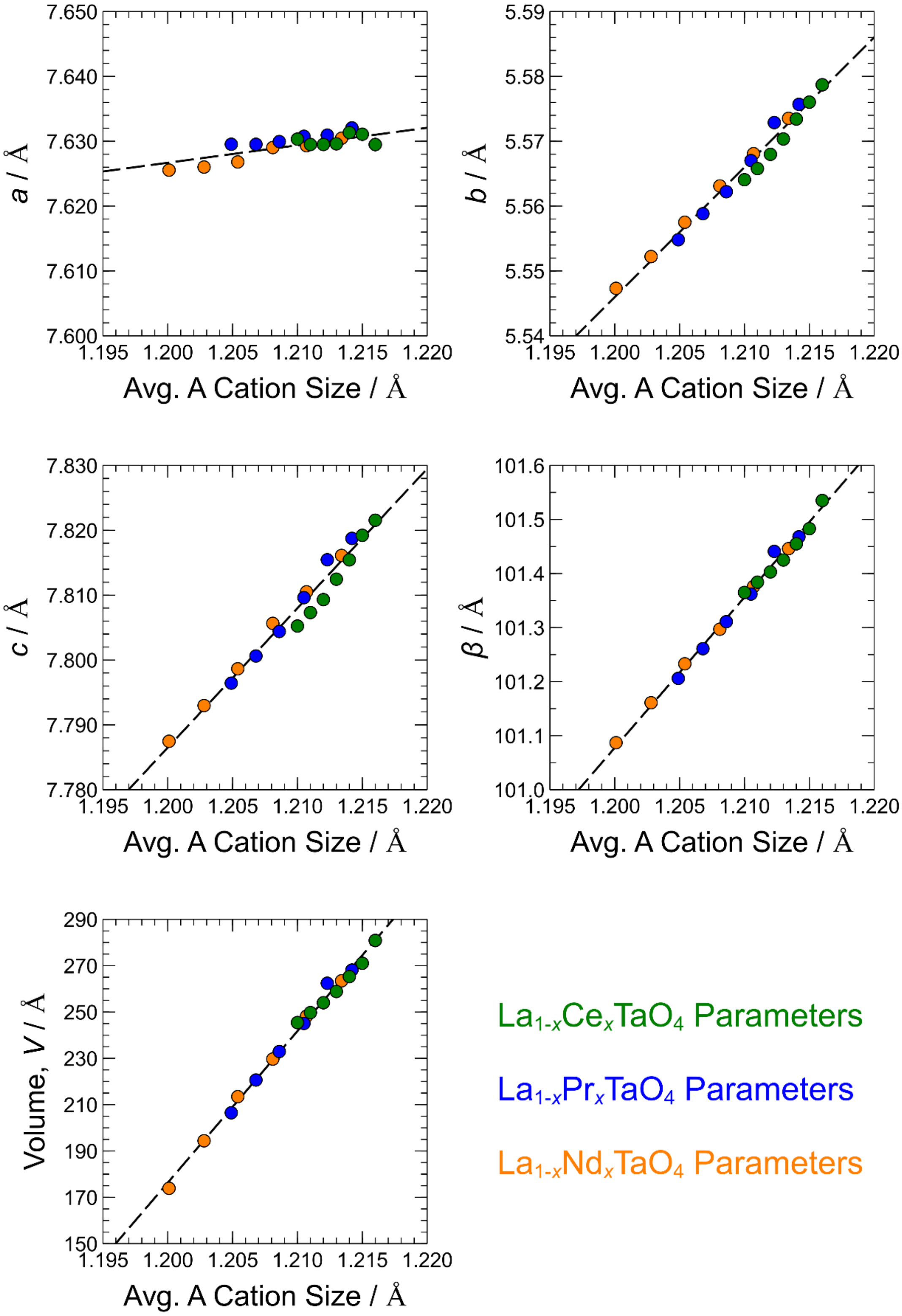

Figure 5.3: Lattice parameters of Ce^{3+}, Pr^{3+} and Nd^{3+} doped $LaTaO_4$ as a function of the average A-cation radius. All plots follow a similar linear trend where an increase in dopant concentration (decrease in average ionic radius) decreases the magnitude of each cell parameter. Error bars are included but are smaller than the datapoint.

5.3.2 Dielectric Spectroscopy

Comparison of the undoped m-$LaTaO_4$ samples examined in this investigation to the 10% Nd^{3+} doped m-$LaTaO_4$ samples produced by Cordrey *et al.* shows an obvious effect on all the phase transition temperatures.[1] Their study shows that the m-$La_{0.9}Nd_{0.1}TaO_4$ sample, which is stabilised in the monoclinic phase by Nd^{3+} doping, has higher phase transition temperatures of $T_{m\text{-}o}$ = 523 K and $T_{IC\text{-}C}$ = 673 K, compared to $T_{m\text{-}o}$ = 443 K and $T_{IC\text{-}C}$ = 503 K in undoped m-$LaTaO_4$. It is evident that the introduction of smaller cations into the A-site has a stabilising effect not only on the monoclinic phase but also stabilises the IC *Cmc*2$_1$ phase to higher temperatures. If the stabilisation of these phases occurs purely by a size effect, there should be a simple correlation between Nd^{3+} cation content and phase transition temperature(s). Dielectric spectroscopy was employed to observe the phase transition sequence of each series of A-cation doped $LaTaO_4$ samples and the results for 0 to 10% Nd^{3+}-doped samples are shown in **figure 5.4**.

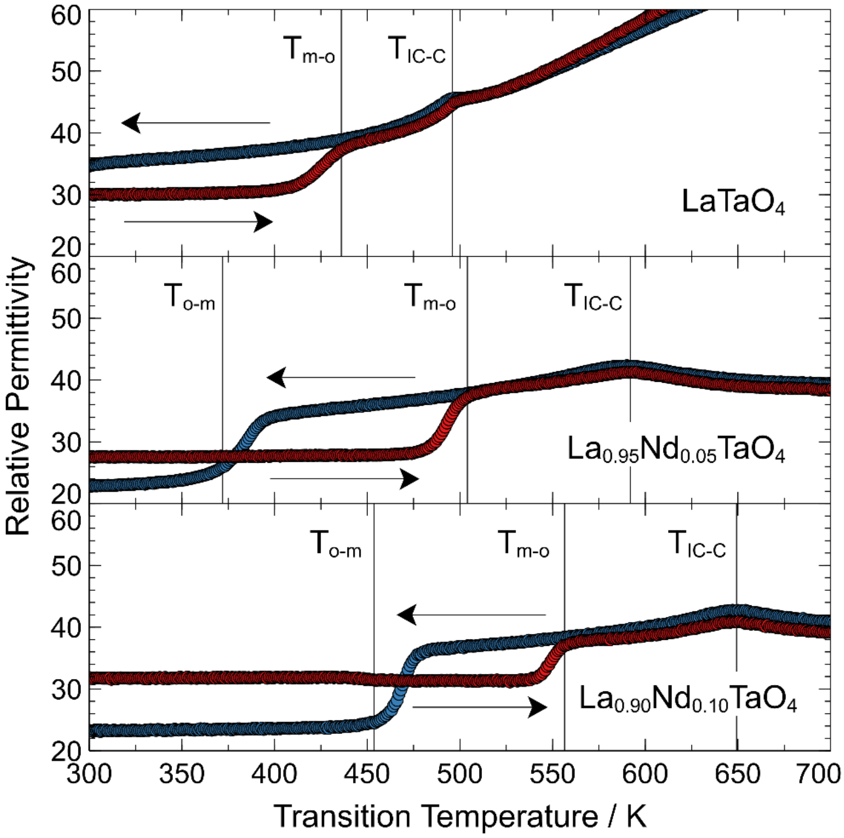

Figure 5.4: Dielectric spectroscopy data for 0 to 10% Nd^{3+}-doped m-$LaTaO_4$. Red traces indicate data that was collected on heating and blue traces indicate cooling (thermal cycle also indicated by arrows). The orthorhombic to monoclinic transitions on cooling ($T_{o\text{-}m}$), monoclinic to orthorhombic transitions on heating ($T_{m\text{-}o}$) and orthorhombic incommensurate – commensurate transitions ($T_{IC\text{-}C}$) are indicated. $T_{o\text{-}m}$ for $LaTaO_4$ is absent from the plot but occurs at just below 300 K.

As the Nd^{3+} content of $La_{1-x}Nd_xTaO_4$ increases we can see that all three of the transitions of interest increase in temperature. This is also true for the Pr^{3+} and Ce^{3+} doped analogues, and the transition temperatures of all dopant series are shown in **figure 5.5**. In most cases we see that all transition temperatures are increased by roughly the same amount as a function of the dopant content, x. This suggests that the size of the A-cation influences both the stabilisation of the monoclinic and incommensurate orthorhombic phase in similar ways *i.e.*, these two phases only become energetically favourable at higher temperatures due to greater size mismatch between the A-cation and the available site volume.

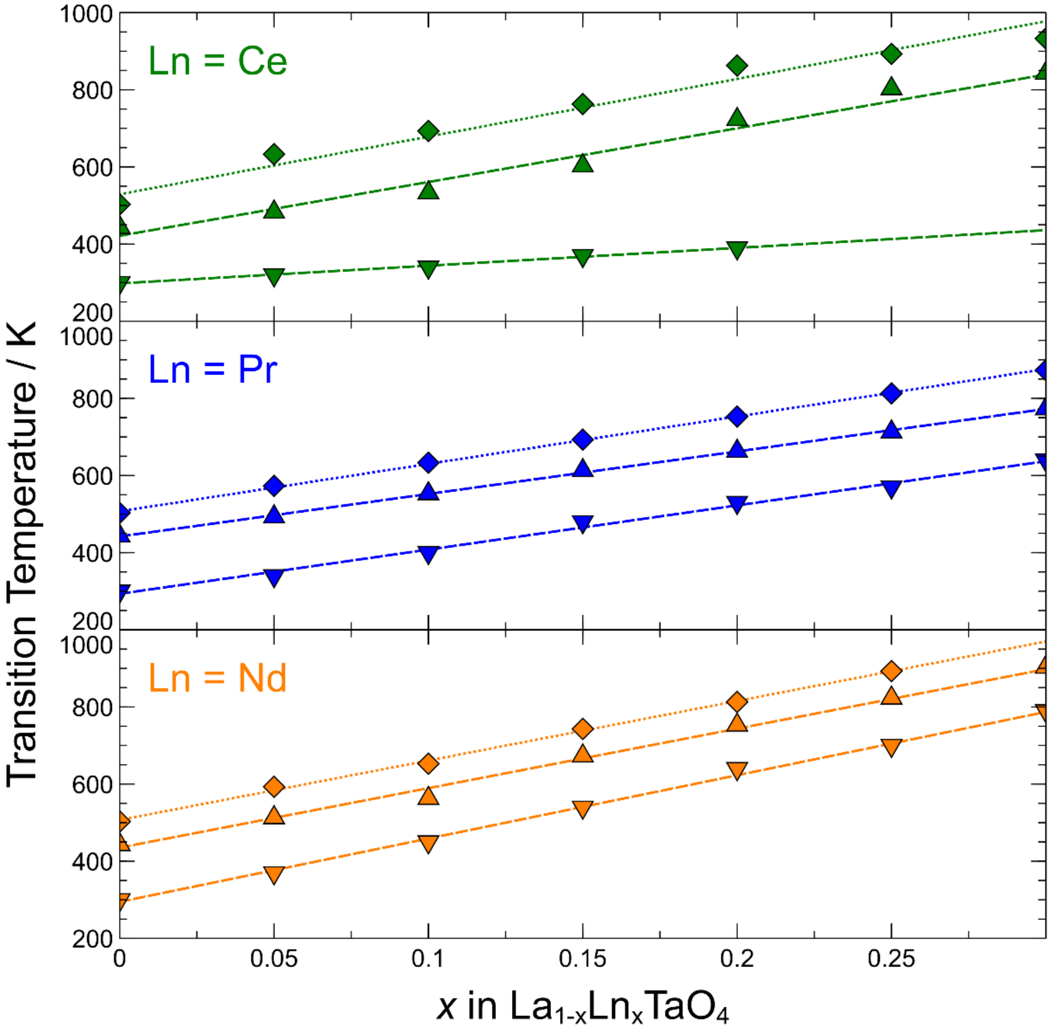

Figure 5.5: Plot of transition temperatures for $La_{1-x}Ln_xTaO_4$ (Ln = Ce^{3+}, Pr^{3+}, Nd^{3+}). $T_{m\text{-}o}$ is indicated by upward pointing triangles, $T_{o\text{-}m}$ is indicated by downward pointing triangles, and $T_{IC\text{-}C}$ is indicated by diamonds. Datapoints have been omitted where no clear indication of a structural change can be observed in the dielectric data.

$T_{o\text{-}m}$ for $La_{1-x}Ce_xTaO_4$, however, does not appear to follow the same trend as the other series of compounds. Although $T_{m\text{-}o}$ and $T_{IC\text{-}C}$ increase by a similar temperature with increasing x, the increase in $T_{o\text{-}m}$ is less pronounced as more Ce^{3+} is added and the thermal hysteresis of the monoclinic-orthorhombic transition widens. When the transition temperatures are plotted as function of average cation radius rather than dopant concentration (**figure 5.6**), it is evident that both Pr and Nd doping behave similarly, however the anomalous behaviour of $T_{m\text{-}o}$ and $T_{IC\text{-}C}$ in the $La_{1-x}Ce_xTaO_4$ series is immediately evident.

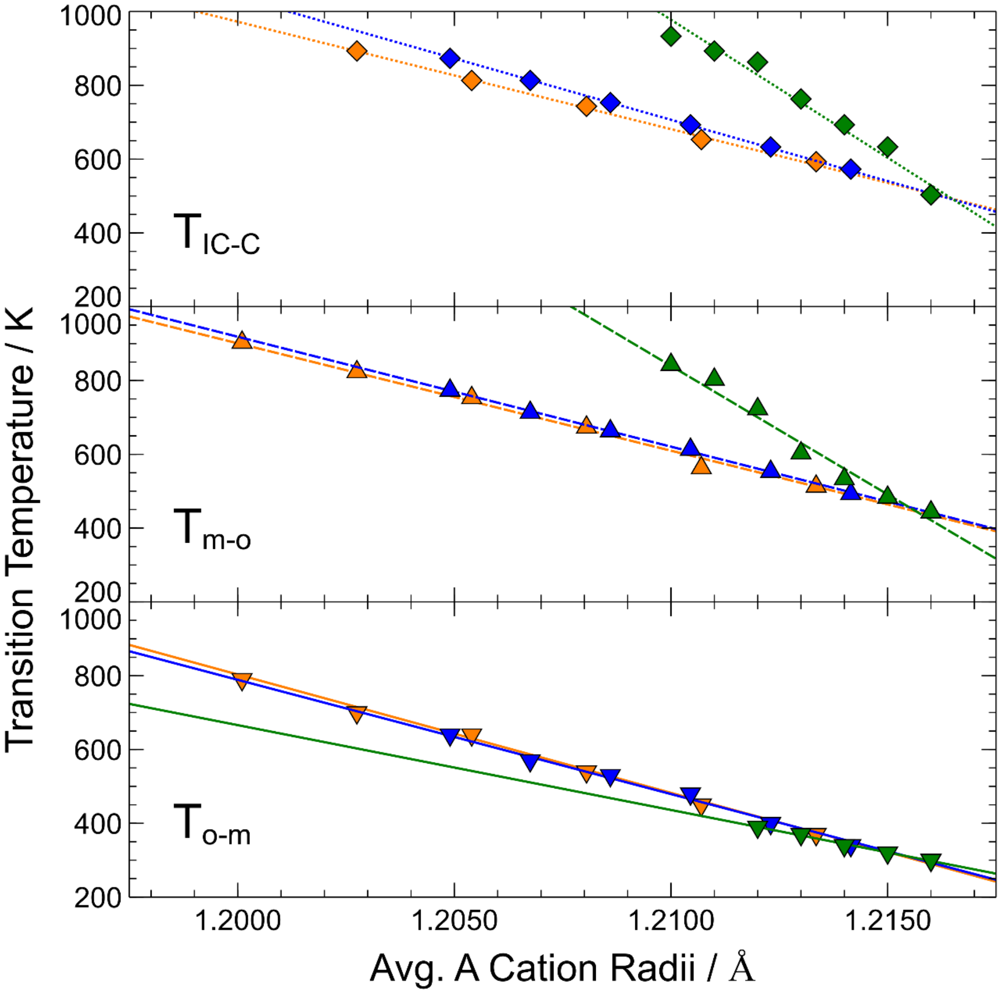

Figure 5.6: Transition temperatures in $La_{1-x}Ln_xTaO_4$ (Ln = Ce^{3+}, Pr^{3+}, Nd^{3+}) as a function of the average radius of the A-cation (green, blue, orange, respectively). Decreasing average cation radius corresponds to an increase in dopant concentration. The $T_{m\text{-}o}$ and $T_{IC\text{-}C}$ gradients for the Nd^{3+} and Pr^{3+} doped samples follow a similar trend but the Ce^{3+} doped samples show a much larger gradient.

If the stabilisation of the monoclinic and orthorhombic phases was purely induced by the size mismatch between the inter-octahedral site volume and the A-cation, each series of compounds would have a similar trend in **figure 5.6**. With the similarities between the Pr^{3+} and Nd^{3+} doped samples, it would be expected in these cases the relationship between doping and transition temperatures is only influenced by the average A-cation size. When the transition temperatures of this series are plotted as a function of average ionic radius, it is evident that for the Ce^{3+} doped structure, $T_{o\text{-}m}$ follows roughly the same trend as the other dopant series, and it is the $T_{m\text{-}o}$ and $T_{IC\text{-}C}$ trends which are anomalous. With increasing dopant concentration, the m-o and IC-C transitions are disproportionately (but equally) raised compared to the Pr^{3+} and Nd^{3+} samples; the Ce^{3+} series has a much steeper gradient for $T_{m\text{-}o}$ and $T_{IC\text{-}C}$, which does not align with the trend of an "average size"-driven effect. The result is an increase in the temperature range over which the monoclinic phase exists on heating and which the incommensurate phase exists on cooling. Ce^{3+} is the largest of the dopant cations and hence most similar in size to La^{3+}, yet appears to have the greatest effect on these transition temperatures. This suggests that there is another driving force which is influencing the m-o and IC-C transition temperatures in the $La_{1\text{-}x}Ce_xTaO_4$ series.

5.3.3 Variable Temperature PXRD

In order to further investigate the effect smaller cations in the A-sites may have on the structure of $LaTaO_4$, variable temperature PXRD data was collected for samples doped with 15% Ce^{3+}, Pr^{3+} and Nd^{3+}, and compared to the undoped m-$LaTaO_4$ data. In order to allow comparison of the orthorhombic and monoclinic phases, the monoclinic cell has been transformed to pseudo-orthorhombic as described in chapter 3; in this setting the octahedra layers lie in the *ac* plane and stack in *b*. The lattice parameters for $La_{0.85}Pr_{0.15}TaO_4$ are shown in **figure 5.7** (other samples are shown in **Appendix C**). In general, the lattice parameters for each doped sample exhibit similar behaviour to that of undoped $LaTaO_4$. For all phases, positive thermal expansion (PTE) is observed in the plane of the octahedral sheets (*ac* plane) with the *b* axis showing NTE only in when in the IC phase. However, when the lattice parameters at the IC transition are compared, it is obvious that the doped samples do not exhibit a clear discontinuity associated with a first order transition at T_{IC} as is observed in undoped $LaTaO_4$.

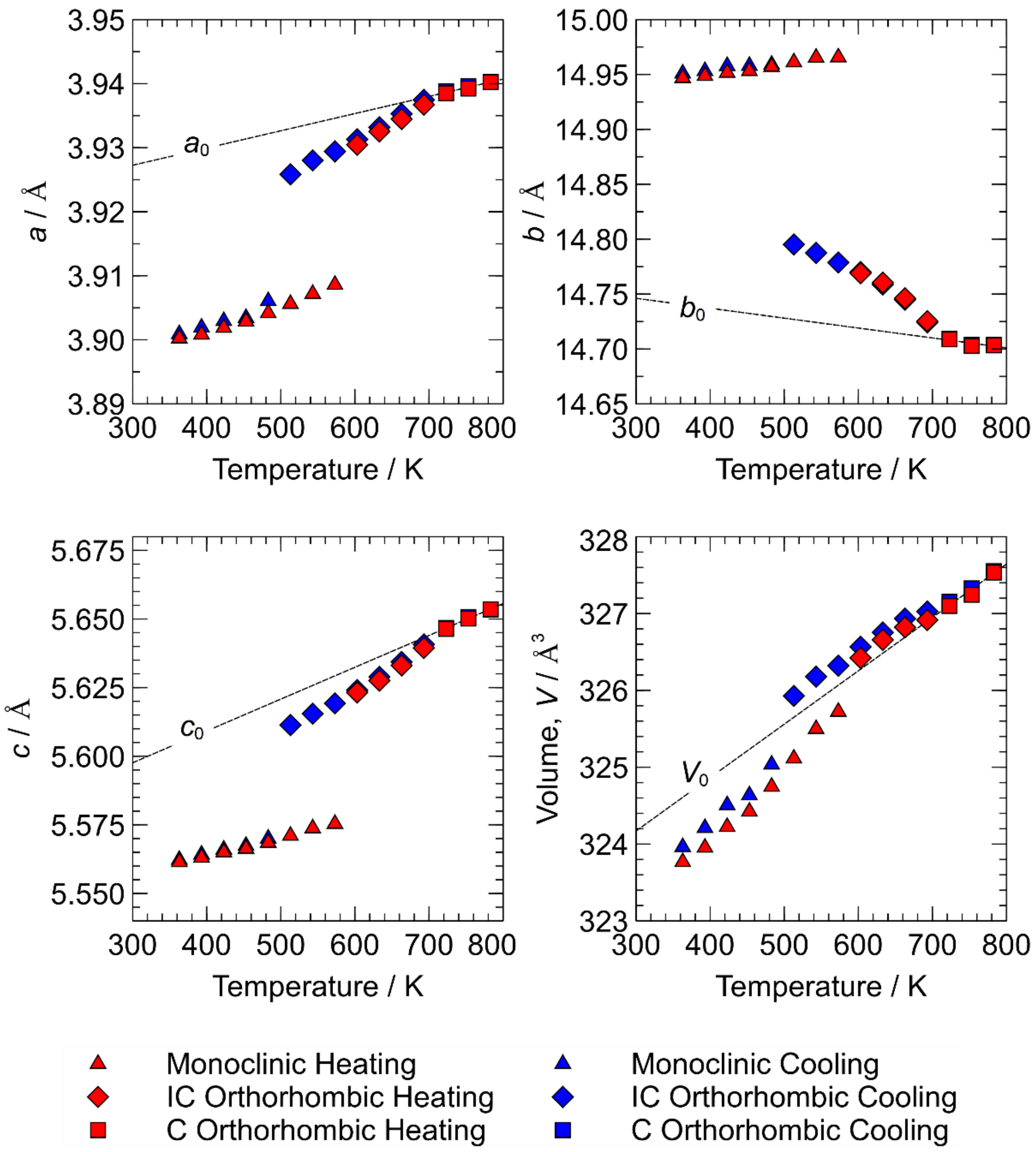

Figure 5.7: Lattice parameters of $La_{0.85}Pr_{0.15}TaO_4$ as a function of temperature . Monoclinic lattice parameters have been transformed into that of a pseudo-orthorhombic cell as in chapter 3. A line of best fit has been added to the commensurate orthorhombic parameters and extrapolated to lower temperatures for reference.

The only lattice parameter which showed any noticeable variation in behaviour between samples is the *b* axis (cooling data shown in **figure 5.8**). The lattice parameters have been normalised to T_{IC} by plotting as a function of $T_{IC\text{-}C}-T$ (temperature relative to the IC-C transition). $La_{0.85}Ce_{0.15}TaO_4$ is observed to have additional, abnormal hysteresis of parameters above 500 K (**Appendix C**) - the potential source of this behaviour is speculated later in the chapter following a brief discussion of XPS data.

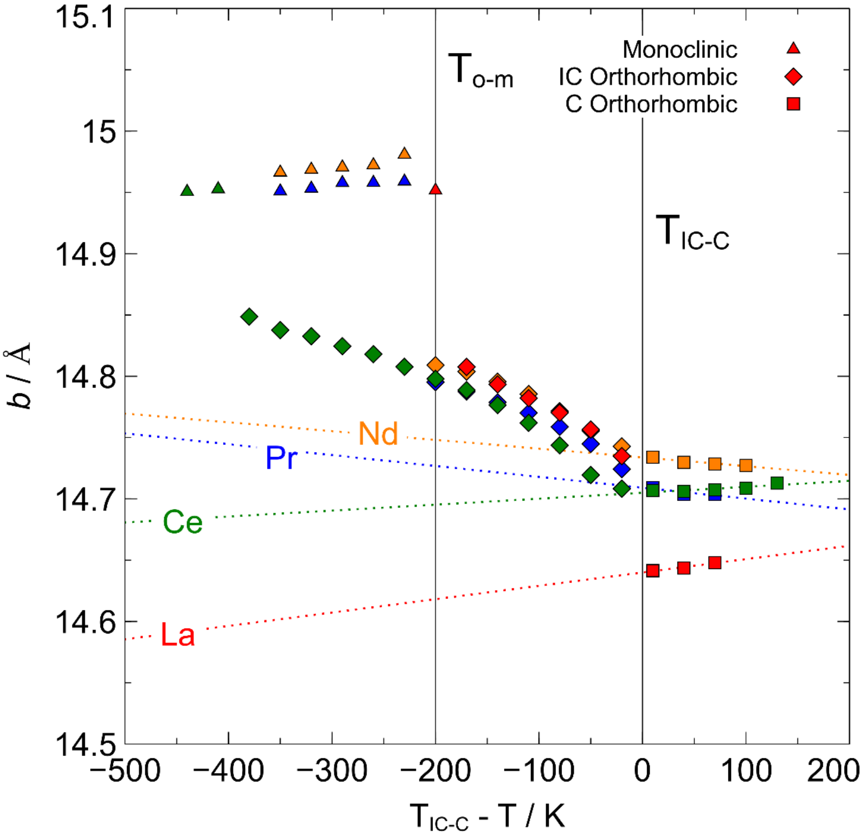

Figure 5.8: *b* parameter of m-La$_{0.85}$Ln$_{0.15}$TaO4 (Ln = Ce, Pr, Nd) as a function of temperature (on cooling). Parameters labelled 'monoclinic' are transformed into the pseudo-orthorhombic cell for comparative purposes, as outlined in chapter 3.

The uniaxial NTE of the stacking axis has been a common area of interest in this investigation and for this material in general. As discussed in previous chapters the NTE in the *b* axis (in the ortho phase) is inherently linked to the IC orthorhombic phase and as LaTaO$_4$ transitions to the high temperature commensurate phase, normal PTE behaviour resumes. From **figure 5.8** it would appear that both 15% Pr^{3+} and Nd^{3+} doped samples do not behave in this way, and that their commensurate orthorhombic phase also maintains uniaxial NTE in *b* over the temperature range measured. However, when comparing this data with that collected for 10% Nd^{3+} doped m-LaTaO$_4$ by Cordrey et al., the latter showed 10% Nd^{3+} doped samples display PTE on further heating above the temperature now known to be T_{IC-C}.[1] It is most likely that this is the case for all doped samples, regardless of dopant concentration or size – the plots for 15% Pr^{3+} and Nd^{3+} shown in **figure 5.8** would inflect upward on further heating. There does appear to be a relationship between A-cation size and the sharpness of transition to PTE, the dynamics of which are not entirely clear at the moment.

As mentioned earlier, it is evident from the lattice parameters that the first order nature of the IC-C transition is seemingly lost in all of the doped samples. This becomes more apparent when the spontaneous lattice strains below the T_{IC} transition are plotted as a function of temperature (**figure 5.9**).

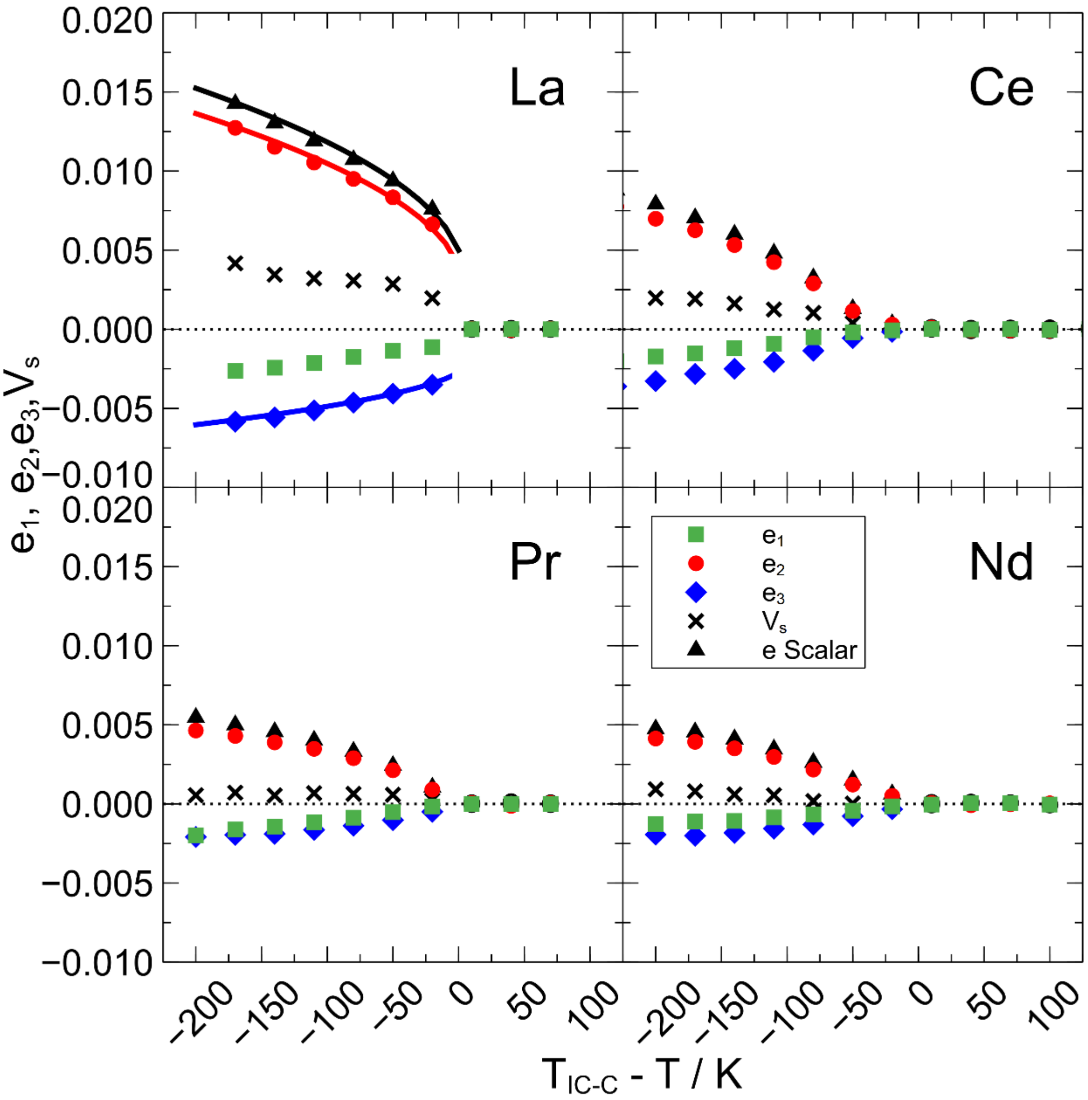

Figure 5.9: Strain values for m-$La_{0.85}Ln_{0.15}TaO4$ (Ln = Ce, Pr, Nd) as a function of temperature (on cooling) at the IC-C transition. The first order nature of the transition in undoped $LaTaO_4$ is shown by fitting data according to equation 1 (also in in chapter 3). Doped samples cannot be fitted using this equation and exhibit no discontinuity in lattice parameters at $T_{IC\text{-}C}$, suggesting a more continuous transition.

As shown in chapter 3, the IC-C transition for $LaTaO_4$ is 1st order in nature and the lattice parameter strain can be fit to the equation:

$$q^2 = \frac{2}{3} q_o^2 \left\{ 1 + \left[1 - \frac{3}{4} \left(\frac{T - T_c}{T_{tr} - T_c} \right) \right]^{1/2} \right\} \qquad 5.1$$

This is derived from a 246 Landau expansion and pertains to a 1st order transition with discontinuous strain - the fit imposed onto the undoped data is produced from this equation with similar coefficients to that given in chapter 3. From the doped sample data, it is obvious that a similar fit would not sufficiently describe the strain behaviour, as these samples seem to lack the discontinuity of strain at the transition and have become seemingly continuous (2nd order). The downward inflection observed in the undoped data also persists in the doped samples but now plateaus at $e = 0$ as the transition is approached. Regardless of cation size, each doped sample seems to exhibit a continuous IC-C transition. It is shown from Raman data that this transition is tricritical, or ‘almost continuous’ so there may be some driving force which has been introduced which directs the phase transition towards exhibiting more 2nd order behaviour – but the driving force for this is, as yet, unclear.

However, it is possible that the apparent 2nd order nature of the IC-C transition in doped samples is not correct, but rather the consequence of the poor resolution of two similar orthorhombic phases coexisting. As discussed in chapter 3, the 1st order nature of the IC-C transition in undoped $LaTaO_4$ was not detected in the initial x-ray data due to the difficulty in resolving two such similar phases, as diffraction peaks were broad and almost entirely overlapping. The region of phase coexistence in $LaTaO_4$ is fairly narrow and was only an issue when looking at the IC-C transition in greater detail (2 K temperature increments). When looking at the transition sequence more generally (30 K increments) this narrow region of phase coexistence is entirely missed (**figure 5.9**).

It may be possible that the addition of smaller A-cations has increased the temperature range of phase coexistence and refinement of the PXRD data shows a volume-weighted combination of lattice parameters as shown in chapter 3; this could also explain the observed delay in return to PTE for the *b* parameter. However, reviewing the PXRD data at this region of suspected phase coexistence shows no evident peak broadening which would support this theory and attempts to perform a two-phase refinement with distinct $Cmc2_1$ parameters did not yield reasonable results. The continuous plateau towards $e = 0$ may still be indicative of residual strain in the sample and this hypothesis of an increased range of phase coexistence may still be valid, although more sensitive structural characterisation would be required.

5.3.4 Preliminary X-Ray Photoelectron Spectroscopy Results

Of all the dopants investigated in this chapter, Ce is most likely to exist in a mixture of oxidation states and so preliminary XPS data was collected for 30% Ce doped m-$LaTaO_4$. Observation of a mixture of Ce^{3+}/Ce^{4+} within the structure may shed some light on the unusual behaviour of the $La_{1-x}Ce_xTaO_4$ when compared to other dopant series. In general, determining the oxidation state of Ce is not trivial [7–11]; this is due to final state electronic configurations having similar energies (La has a similar effect, but not as pronounced as Ce). XPS spectra for $LaTaO_4$ and $La_{0.7}Ce_{0.3}TaO_4$ are shown in **figure 5.10**. In practical terms, Ce^0 shows as a doublet, Ce^{3+} as a doublet of doublets (4 peaks) and Ce^{4+} as a triplet of doublets (six peaks). Usually, Ce^{4+} is recognisable by the presence of a peak at *ca.* 917 eV. The apparent absence of such a feature seems to rule out Ce^{4+}, however, the shapes of the remaining peaks seem to indicate a substantial amount of it. One model[10] predicts a Ce^{4+}:Ce^{3+} ratio of ~ 3:1 whereas another predicts ~1:1.[11] As Ce^{3+} is expected as the majority oxidation state, sources of errors could be: the poor signal-to-noise ratio (this could be improved in different ways, but generally speaking would require very long acquisition times); the granularity (fine particles can produce peak broadening); the insulating character of the samples; and/or the superposition of a La Auger peak with the Ce 3d region. Although these results are far from quantitative, it acts as sufficient evidence of mixed Ce oxidation states and therefore it would be logical to explore this as the root cause of the anomalous behaviour.

A mixture of Ce oxidation states in monoclinic $LaTaO_4$-like structures has been previously reported by Negas *et al.*, with $CeTaO_4$ being stable in air above 1538 K.[5] Below this temperature a mixture of Ce^{3+} / Ce^{4+} oxidation states occur and additional oxide ions are incorporated into the system as compensation for Ce^{4+}. This system is described by the formula:

$$\mathrm{CeTaO_4} + \frac{1}{2}\mathrm{O_2} \leftrightarrow \mathrm{Ce^{3+}_{1-2y}Ce^{4+}_{2y}TaO_{4+y}} \tag{5.2}$$

where *y* is temperature dependent. The value of *y* is reported as ~0.25 between 623 - 873 K, which would result in a 1:1 Ce^{3+} / Ce^{4+} mixture, mirroring that suggested by the second XPS model. Depending on annealing conditions, temperatures below this range may have only Ce^{3+} present – but this may only be true for $CeTaO_4$ and different values of *y* maybe be obtained in Ce-doped $LaTaO_4$.[5] It is noted that the difference in ionic radii of 9-coordinate Ce^{3+} and Ce^{4+} ions is not substantial, and the intercalation of additional oxygens would have a much stronger structural influence.

The temperature dependence and reversibility of this system could also clarify some other unusual behaviours in $La_{1-x}Ce_xTaO_4$ - such as the hysteresis in lattice parameters observed by VT-PXRD (**Appendix C**). At the moment this is only speculation and more sensitive diffraction techniques (or thermogravimetric analysis) would be needed to link the uptake of interstitial oxygens to the observed hysteresis in lattice parameters. The temperature at which the value of *y* is reported to change (873 K) does not directly coincide with the observed hysteresis, although, the equilibrium (diffusion) rates of the $La_{1-x}Ce_xTaO_4$ system may be somewhat different from $CeTaO_4$.

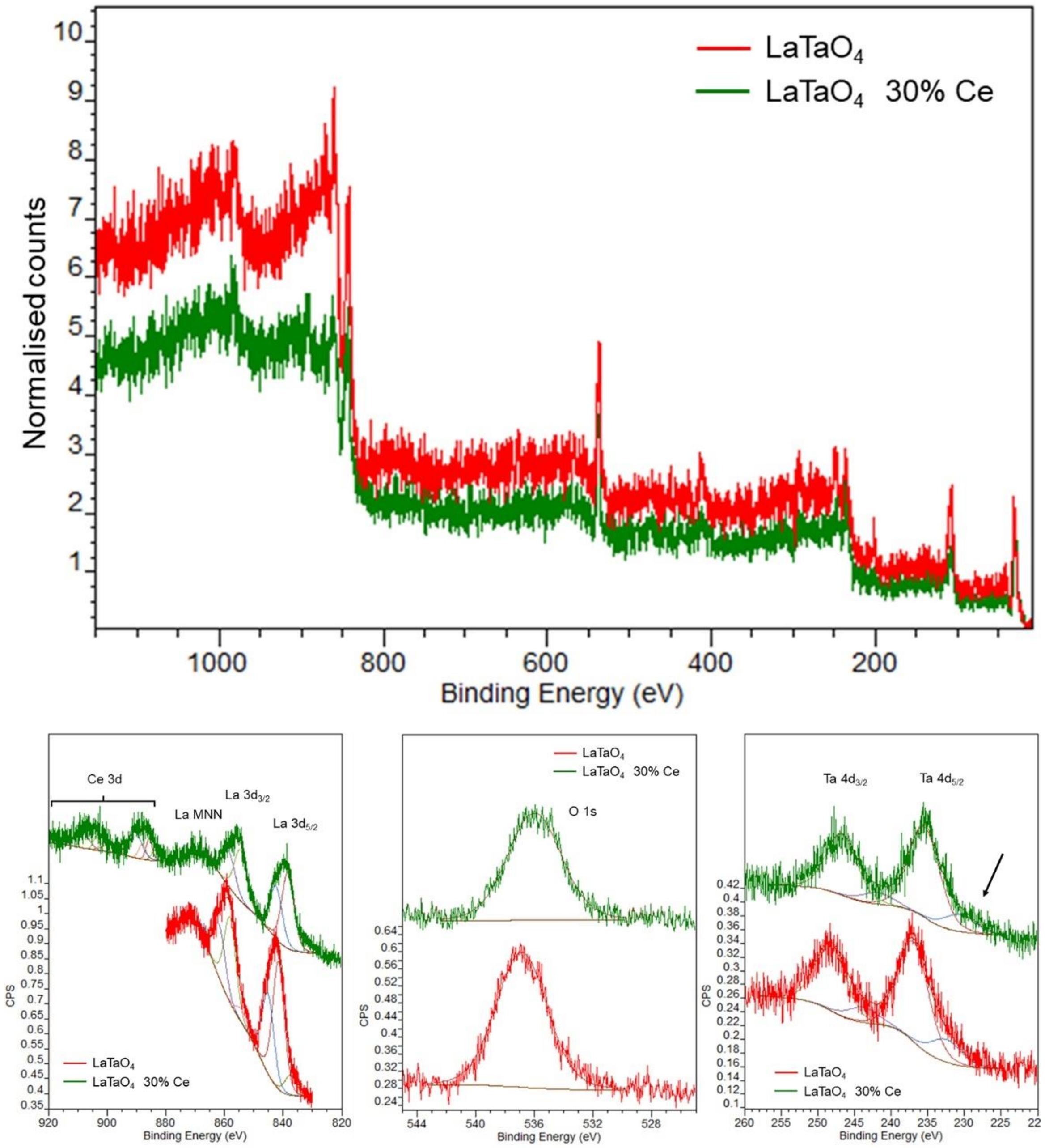

Figure 5.10: (a) XPS survey spectra of LaTaO$_4$ (red) and La$_{0.7}$Ce$_{0.3}$TaO$_4$ (green). Detailed scans of (b) Ce 3d/La 3d (c) O 1s and (d) Ta 4d. The arrow in Ta 4d exemplifies the tail introduced by the use of charge compensation. All XPS data collection and analysis was conducted by Dr. Federico Grillo at the University of St Andrews.

The effect the additional oxygens have on the $P2_1/c$ structure has also been studied in the past. Following on from the work of Negas *et al.*[5], the structural study of the $CeTaO_{4+y}$ system by Thompson *et al.* indicated that the additional oxygens are coordinated to four interstitial Ce cations.[12] This introduces a new interstitial oxygen site and this could also assumed to be the case for $La_{1-x}Ce_xTaO_4$. These oxygen positions, however, could not be identified by the PXRD techniques utilised in this current study, and the changes to the cation positions within the structure are reported to be so minor that they alone could not conclusively determine the presence of interstitial oxygens.[12] Given the similarity between these structures and the observation of Ce^{4+} in $La_{0.7}Ce_{0.3}TaO_4$, it is most likely that interstitial oxygens are being introduced in a structurally very similar way to that observed in $CeTaO_{4+y}$. Re-examining the PXRD data gathered for $La_{0.85}Ce_{0.15}TaO_4$, the observed additional hysteresis in parameters observed above 500 K may be a consequence of the reversible oxidation of Ce^{3+} and the incorporation of interstitial oxygens into the structure.

With the assumption that the $CeTaO_{4+y}$. and $La_{1-x}Ce_xTaO_4$ systems are somewhat similar, we can revisit the dielectric data and rationalise some of the unusual behaviour of the transition temperatures observed as a function of Ce doping $LaTaO_4$. As discussed above, the lowest temperature transition, $T_{\text{o-m}}$, in this system followed the same general pattern of behaviour displayed by the Pr^{3+} and Nd^{3+} doped systems – suggesting the alteration of this transition temperature was a size effect. The onset of oxidation in the $CeTaO_4$ samples is reported to start at ~623 K which is higher than any observed $T_{\text{o-m}}$. This would be consistent with oxidation of $La_{1-x}Ce_xTaO_4$ as the driving force of the anomalous trend in the higher transition temperatures, which occur above 623 K. This encapsulates all values of $T_{\text{IC-C}}$ and most of $T_{\text{m-o}}$ – it could be argued that the first three or four data points for $T_{\text{m-o}}$ exhibit size-driven behaviour and then inflect upwards at ~623 K. From this it could be suggested that the interstitial oxygens influence the stability of the these phases, but this clearly needs further investigation.

5.4 Summary and Conclusion

Samples of $La_{1-x}Ln_xTaO_4$ (Ln = Ce^{3+}, Pr^{3+}, Nd^{3+} with $0 \leq x \leq 0.3$) were successfully synthesised in the monoclinic polymorph with each dopant being introduced into the structure as evidenced by adherence to Vegards law (all parameters contracted linearly as a function of decreasing average ionic radius). As expected, the introduction of smaller A-cations stabilised the monoclinic and IC orthorhombic phases, and hence increased $T_{\text{o-m}}$, $T_{\text{m-o}}$ and $T_{\text{IC-C}}$ to higher temperatures. Dielectric spectroscopy allowed the phase transitions to be plotted as a function of the dopant concentration and average ionic radius; this shows that although Pr^{3+} and Nd^{3+} doped samples follow the same linear relationship, the transition temperatures are much more strongly affected by Ce doping. In the case of Pr^{3+} and Nd^{3+} doping the stabilisation of these phases appears to be purely a size effect: the monoclinic / IC orthorhombic phase is more favourable when there is a greater size mismatch between the A-cations and A-site volume as a result of increased octahedral tilting. The abnormal effect of Ce doping is speculated to be due to the introduction of interstitial oxygens caused by a mixture of Ce^{3+} / Ce^{4+} cations within the structure – this is indicated by preliminary XPS data. The oxidation of Ce^{3+} and subsequent uptake of interstitial oxygens is observed in $CeTaO_4$; this is reversible process and the ratio of Ce^{3+} / Ce^{4+} is temperature dependent. This is also expected to be the case for Ce doped $LaTaO_4$ and may be the cause of a small hysteresis in lattice parameters observed from VT-PXRD (the other dopant cations exhibit similar behaviours in their lattice parameters as in undoped m-$LaTaO_4$). The presence of interstitial oxygens in the structure has not been directly observed but they are expected to be the cause of the abnormal transition temperature behaviour in the $La_{1-x}Ce_xTaO_4$ due to the temperature dependence of Ce^{3+} oxidation, but more detailed analysis is needed to confirm this hypothesis.

5.5 References

1. Cordrey, K. J. *et al.* Structural and Dielectric Studies of the Phase Behaviour of the Topological Ferroelectric $La_{1-x}Nd_xTaO_4$. *Dalt. Trans.* **44**, 10673–10680 (2015).

2. Abreu, Y. G., Siqueira, K. P. F., Matinaga, F. M., Moreira, R. L. & Dias, A. High-Temperature Antiferroelectric and Ferroelectric Phase Transitions in Phase Pure $LaTaO_4$. *Ceram. Int.* **43**, 1543–1551 (2017).

3. Hartenbach, I. *et al.* Über Oxotantalate der Lanthanide des Formeltyps $MTaO_4$ (M = La - Nd, Sm - Lu). *Zeitschrift fur Anorg. und Allg. Chemie* **631**, 2377–2382 (2005).

4. Vullum, F., Nitsche, F., Selbach, S. M. & Grande, T. Solid Solubility and Phase Transitions in the System $LaNb_{1-x}Ta_xO_4$. *J. Solid State Chem.* **181**, 2580–2585 (2008).

5. Negas, T., Roth, R. S., McDaniel, C. L., Parker, H. S. & Olson, C. D. Oxidation-Reduction Reactions of $CeMO_{4+x}$ (M = Ta or Nb) phases. *Mater. Res. Bull.* **12**, 1161–1171 (1977).

6. N. Fairley et al, Applied Surface Science Advances (2021), https://doi.org/10.1016/j.apsadv.2021.100112.

7. Moulder, J. F., Stickle, W. F., Sobol, P. E. & Bomben, K. D. *Handbook of X-ray Photoelectron Spectroscopy: a Reference Book of Standard Spectra for Identification and Interpretation of XPS Data*. *Surface and Interface Analysis* (1992).

8. X-ray Photoelectron Spectroscopy Database Version 4.1, National Institute of Standards and Technology, Gaithersburg (2012) (Accessed July 2021); http://srdata.nist.gov/xps/.

9. Burroughs, P., Hamnett, A., Orchard, A. F. & Thornton, G. Satellite Structure in the X-ray Photoelectron Spectra of some Binary and Mixed Oxides of Lanthanum and Cerium. *J. Chem. Soc., Dalt. Trans.* 1686–1698 (1976).

10. Holgado, J. P., Munuera, G., Espinós, J. P. & González-Elipe, A. R. XPS Study of Oxidation Processes of CeO_x Defective Layers. *Appl. Surf. Sci.* **158**, 164–171 (2000).

11. Truffault, L. *et al.* On the Curve-fitting of XPS Ce(3d) Spectra of Cerium Oxides by E. Paparazzo, Materials Research Bulletin 46 (2011) 323-326. *Materials Research Bulletin* **47**, (2012).

12. Thompson, J. G., Rae, A. D., Bliznyuk, N. & Withers, R. L. Ordering of CeIII/CeIVand Interstitial Oxygens in $CeTaO_{4+x}$($x\approx0.17$) Superstructure. *J. Solid State Chem.* **144**, 240–246 (1999).

6 Chapter 6: Summary, Conclusions and Further Work

6.1 Summary and Conclusions

The structural phase transition sequence of $LaTaO_4$ has been re-examined in-depth by a variety of diffraction and spectroscopic techniques to reveal that an intermediate incommensurately modulated phase exists between the low temperature monoclinic phase and the high temperature (unmodulated) orthorhombic phase. The unassigned dielectric anomaly reported in previous studies[1,2] has been shown to coincide with the IC-C transition between the two orthorhombic phases.

Previous studies have noted the influence of processing conditions on the monoclinic-orthorhombic transition, $T_{\text{m-o}}$, and subsequently the stability of each polymorph under ambient conditions. The work undertaken in this thesis has built on the findings of each study to produce a reliable method for producing o-$LaTaO_4$ and m-$LaTaO_4$ samples without the need for A-site doping. Ball milling powder precursors, hand pressing pellets and annealing at lower temperatures is found to produce relatively phase pure orthorhombic samples, similarly to the method employed by Cordrey *et al.*.[1] Pressing those same pellets with 30,000 psi of isostatic pressure and annealing at higher temperatures produce phase pure monoclinic samples, following the findings of Vullum *et al.*.[3]

PXRD data collected for $LaTaO_4$ shows a clear step-change in lattice parameters at ~503 K coinciding with the dielectric anomaly, and there are noticeable changes in thermal expansion behaviour (PTE of the *ac* plane becomes less substantial and the NTE observed in the *b* axis becomes positive). There is no clear change in the symmetry of the orthorhombic phase across the transition and no other structural differences can be detected by x-rays at the transition.

Detailed inspection of PND data reveals clear additional reflections which cannot be accounted for by the basic (commensurate, C) $Cmc2_1$ phase or any additional secondary phase. These were found to be satellite reflections, generated from an incommensurately (IC) modulated structure, which exist in the orthorhombic phase up to ~503 K before disappearing. The diffraction patterns collected in the range of the IC-C transition (~480 – 520 K) shows clear coexistence of two distinct $Cmc2_1$ phases with individual lattice parameters. This indicates a 1st order phase transition and hints at some structural differences between the modulated and basic structures.

Several methods have been employed to characterize the nature of the newly discovered IC-C transition. Strain analysis was carried out using the lattice parameters discerned from PND data and a Landau expansion and this confirmed a non-linear variation of lattice strain which abruptly disappears at $T_{\text{IC-C}}$ - this is typical of a 1st order transition. RUS data further confirms classical 1st order behaviour at the IC-C transition but also highlights some differences in elastic behaviour between o-$LaTaO_4$ and m-$LaTaO_4$ samples. For example, the elastic softening in m-$LaTaO_4$ (~80%) on cooling to the IC-C transition is much larger than that for o-$LaTaO_4$ (~20%), despite the strain behaviour being almost identical between the two. Strong acoustic loss is observed below $T_{\text{m-o}}$ which is likely due to the presence of ferroelastic twin walls in the monoclinic phase. Raman spectroscopy results were also consistent with a 1st order transition, as evident from the discontinuous mode frequencies at the transition temperatures. Not all predicted Raman modes are observed but this is expected to be a consequence of accidental degeneracy of band frequency or undetectably low mode intensity, and is still consistent with proposed phase transition sequence, and is not evidence of a transition to the *Cmcm* phase, as proposed by Abreu *et al.*.[2] The Raman lines observed in the monoclinic phase are more numerous than expected and may indicate the presence of a superstructure which also exists below $T_{\text{m-o}}$.

Electron diffraction of the IC $Cmc2_1$ phase shows the satellite reflections appear only along the reciprocal *a* axis which bears similarity to other modulated Carpy-Galy phases such as $Sr_2Nb_2O_7$.[4] Using this $n = 4$ oxide as a guide, the PND data was refined to a incommensurately modulated model with the $Cmc2_1(\alpha00)0s0$ superspace group and a modulation wavevector of $q = (0.456\ 0\ 0)$ at 483 K, however q varies as a function of T, decreasing as $T_{\text{IC-C}}$ is approached. The modulation is speculated to arise as a means of improving the overall bonding environment of the A-cation by shifting the La^{3+} diagonally in and out of the octahedral sheets and is accompanied by a tilting of the octahedra. Bond valence calculations for La^{3+} as a function of the modulation wave, indicates an overall improvement in the bonding environment compared to the unmodulated $Cmc2_1$ model. The deviation from the unmodulated structure is evident in the lattice parameters, as the corrugation of the octahedral sheets leads to a contraction of the *ac* plane and poorer packing of the octahedral layers increases the *b* parameter. The unusual thermal expansion behaviour is then speculated to be purely a consequence of the modulated structure. The PTE in the *ac* plane can then be attributed to the ‘straightening’ of the puckered sheets with increasing *T* and consequently a more efficient stacking in *b*, which manifests as NTE in this axis.

Electron microscopy was utilised to reveal that the local origin of the modulation is not a simple continuous deviation of atomic positions but rather a partial ordering of smaller sub-units which gives rise to an incommensurate repeating distance. A model has been proposed which combines the local structure and the macroscopic observations for the IC phase. The structural model devised from PND data can be split into sub-units, M and N, which are 3× and 2.5× expansions of the original $Cmc2_1$ cell in a, respectively, and these units can be used to account for the repeating distances observed by HRTEM. The most common arrangement of these units is proposed to be 2N + 2M which generates an average modulation wavevector of $11a$, which is approximately equal to the $q = 0.456a^*$ observed by PND. The M and N sub-units are determined by the tilting pattern which they exhibit and as a consequence of this, the manner in which they stack is dictated by some simple rules: M units may stack freely along *a* and those adjacent to N units are shifted by a half unit cell in *b*. Only like units may stack in *b* and *c*, and as such, no modulation is observed in these axes.

The influence of A-cation doping on transition temperatures, first demonstrated by Cordrey *et al.*[1], is explored in the synthesis of the series $La_{1-x}Ln_xTaO_4$ (Ln = Ce^{3+}, Pr^{3+}, Nd^{3+} with $0 \leq x \leq 0.3$). Substitution of isovalent cations into the A-site demonstrates that the stabilisation of low temperature phases up to higher temperatures is purely a size-driven effect, induced by the mismatch of smaller cation radii and the bonding environment. Plots of the lattice parameters versus the average cation radii shows a linear trend, suggesting that the smaller dopants are being successfully incorporated into the A-site and the parameters are subsequently contracting. The anisotropy of the contraction in the parameters with increasing x is speculated to be a consequence of the layered structure.

Plotting the transition temperatures of monoclinic samples versus the average radii of the A-cations yields a linear increase in all phase transitions with decreasing ionic radii. Nd^{3+} and Pr^{3+} doped samples follow a very similar trend, where all transitions are shifted in temperature by roughly equal amounts relative to average cation size, which confirms that the stabilisation of the low temperature phases is purely a steric effect. Ce^{3+} doped samples were found to not exhibit the proportional behaviour. The deviation of these materials from the trend followed by Pr^{3+} and Nd^{3+} compounds is thought to be a consequence of a reversible oxidation of Ce^{3+}, and subsequent uptake of interstitial oxygens, that occurs as the samples are heated. Preliminary XPS data indicates that there is likely a mixture of Ce^{3+} and Ce^{4+} present at room temperature.

Initial structural analysis of $LaTaO_4$ by PXRD was somewhat useful in showing a step change in lattice parameters that coincided with the dielectric anomaly but failed to reveal the more important details of the modulated phase, such as the satellite reflections or the 1st order nature of the transition. X-rays are typically sensitive enough to determine the position of heavier elements such as La, but in this case the variability of the A-cation position could not be concluded from the x-ray data alone. This highlights the usefulness of high resolution neutron diffraction in the determination of structures whose translational symmetry is broken by relatively subtle structural differences. This is especially true for materials such as the layered perovskites, where it is often found that a large component of the modulation is a distortion of the octahedral framework, and hence the accurate mapping of oxygen positions is critically important in revealing the nature of these phases.

The application of complementary analytical techniques has been found to be a key factor for the characterisation of $LaTaO_4$ in this study. RUS and Raman data have been consistent in their determination of the nature of all phase transitions, but electron microscopy and PND data gave initially incompatible models. The seemingly continuous modulation of the structure determined from PND and the disordered structural unit model observed by electron microscopy seemed contradictory, but considering elements of each model allows for a more accurate picture of the modulated structure to be constructed. Although the macroscopic model determined by neutron diffraction is a spatial average, structural elements could be identified which were used to account for the local observations. Searching for compatible information within each approach allowed for a more realistic representation of the modulated phase to be constructed and serves as an example of synergies between two seemingly conflicting models.

The wealth of structural information which has been revealed by this work shows the great potential for further discoveries pertaining to the Carpy-Galy materials. Despite the general similarities between $LaTaO_4$ and other Carpy-Galy phases, the modulated phase has only now been identified despite its presence in materials such as $Sr_2Nb_2O_7$ and $BaMnF_4$ being well documented since the 1970's. With the possibility of a monoclinic structure and the dynamics of Ce doped samples left as open ended questions, there seems to be a lot more characterization left to conduct regarding the structure and tunability of $LaTaO_4$.

6.2 Further Work

The detailed structural characterisation in this work has been primarily focussed on the elucidation of the modulated incommensurate orthorhombic phase but evidence of a monoclinic superstructure has been revealed by Raman spectroscopy data. Although neutron diffraction data has been presented for the $P2_1/c$ phase, no satellite reflections are observed which would indicate that this is the case. Given how subtle the satellite reflections for the orthorhombic superstructure are it should not be a case for ruling out the existence of a modulated monoclinic structure. Other Carpy-Galy phases, such as $BaMnF_4$, occupy modulated $P2_1/c$ phases at low temperatures[5] and it would seem logical that the possibility of it also being the case for $LaTaO_4$ should be explored by other techniques which are sensitive to such subtle structural variations. The success of SAED in identifying the satellite reflections and approximate modulation wavevector of the IC orthorhombic phase would suggest that this would be a constructive approach to identifying a similar feature in the monoclinic structure.

One key feature of incommensurate $BaMnF_4$ that went unnoticed for years is it's 'devil's staircase' temperature dependence of q, where the modulation wave vector was confirmed to change in a step-wise fashion.[6–8] The plot of the wavevector a^* component, σ_1, versus T presented in chapter 3 shows a seemingly continuous relationship between the magnitude of the modulation wave and temperature, but it is not uncommon for features such as devil's staircases to be hidden by poor sample quality[9] or perhaps sparsity of datapoints. In order to explore the possibility of a devil's staircase existing in the IC orthorhombic phase of $LaTaO_4$, further variable temperature PND data could be collected, with datapoints attained over much smaller temperature intervals. The explication of the modulation wavevector relies heavily on the definition of the satellite reflections, and with the incredibly small positional variation they exhibit across the temperature range of interest, longer collection times would of course be beneficial. It is noted that sample quality is somewhat more limited than that for previous $BaMnF_4$ studies, which were performed on single crystals, and revealing such a feature in a ceramic sample may be severely impeded. Variable temperature electron microscopy would be suitable to track changes in modulation vector with T but given the local disorder it would be difficult to quantify a macroscopic wavevector, in the same way that has been achieved by PND.

The work by Cordrey *et al.* first exhibited the relationship between the stability of the low temperature phases of $LaTaO_4$ and doping the A-site with smaller isovalent cations.[1] This work has expanded on this by showing that this is a purely size-driven effect and shows a clear negative linear relationship between the average A-cation size and all transition temperatures. However, the effect of doping smaller cations into the A-site has on the modulated structure has yet to be established. It would be interesting to characterize the modulated structure of doped samples in a similar manner to what has been presented here, observing the effect that it has on the extent of the structural variations, the sub-units which are formed and the manner in which they order *i.e.* determining their average periodicity in the form of a macroscopic modulation wavevector. The inability to observe any evidence of the modulation in PXRD data or properly quantify the overall modulation vector from electron microscopy on its own would mean a comparable study of doped samples would be reliant on the collection of further PND data at central facilities. This is, however, not limited to A-site doping, as successful manipulation of transition temperatures has already shown by Vullum *et al.*[3] and the effect that this also has on the modulation would be an interesting complement to this work.

The linear relationship between A-cation size and the transition temperatures in $LaTaO_4$ samples is seemingly broken by the series $La_{1-x}Ce_xTaO_4$, where a steeper correlation between the two parameters is observed. Preliminary XPS results suggest that there is a mixture of Ce^{3+} and Ce^{4+} present in samples at room temperature, however quantifying the ratio of these cations is difficult for a variety of practical and analytical reasons. Additional collection times for samples may be one route to alleviate this issue but was out with the time constraints of this work. The mechanism which drives the greater shift in $T_{m\text{-}o}$ and $T_{IC\text{-}C}$ in these samples is still unconfirmed but at the moment a reversible oxidation reaction and intercalation of oxygen above ~600 K is speculated to be the cause. Current PXRD data shows a hysteresis in lattice parameters, but this only suggests that there is some reversible structural change. More precise variable temperature structural analysis by PND or electron microscopy may reveal subtle structural changes induced by the uptake of additional interstitial oxygens, and may be beneficial in determining the root cause of the abnormal change in $T_{m\text{-}o}$ and $T_{IC\text{-}C}$.

6.3 References

1. Cordrey, K. J. *et al.* Structural and Dielectric Studies of the Phase Behaviour of the Topological Ferroelectric $La_{1-x}Nd_xTaO_4$. *Dalt. Trans.* **44**, 10673–10680 (2015).

2. Abreu, Y. G., Siqueira, K. P. F., Matinaga, F. M., Moreira, R. L. & Dias, A. High-Temperature Antiferroelectric and Ferroelectric Phase Transitions in Phase Pure LaTaO4. *Ceram. Int.* **43**, 1543–1551 (2017).

3. Vullum, F., Nitsche, F., Selbach, S. M. & Grande, T. Solid Solubility and Phase Transitions in the Ssystem $LaNb_{1-x}Ta_xO_4$. *J. Solid State Chem.* **181**, 2580–2585 (2008).

4. Daniels, P. *et al.* The Incommensurate Modulation of the Structure of $Sr_2Nb_2O_7$. *Acta Crystallogr. Sect. B Struct. Sci.* **58**, 970–976 (2002).

5. Sciau, P., Lapasset, J., Grebille, D. & Berar, J. F. Incommensurate Modulated Structure of $BaMnF_4$ with Monoclinic Symmetry at 100 and 210 K. *Acta Crystallogr. Sect. B Struct. Sci.* **44**, 108–116 (1988).

6. Hidaka, M., Scott, J. F. & Storey, J. S. Energy Dispersive X-ray Diffraction Study of Structural Phase Transitions in $BaMnF_4$. *Phys. B+C* **123**, 291–299 (1984).

7. Scott, J. F., Habbal, F. & Hidaka, M. Phase Transitions in $BaMnF_4$: Specific Heat. *Phys. Rev. B* **25**, 1805–1812 (1982).

8. Hidaka, M., Nakayama, T., Scott, J. F. & Storey, J. S. Piezoelectric Resonance Study of Structural Anomalies in $BaMnF_4$. *Phys. B+C* **133**, 1–9 (1985).

9. St-Gregoire, P. *et al.* On the Incommensurate Phase in $BaMnF_4$: A Neutron Scattering Study. Effect of the pressure. *Ferroelectrics* **53**, 307–310 (1984).

Appendix A: Chapter 3 Refinement Details

Table A.1: Refinement details of diffraction profiles shown in chapter 3. IC Orthorhombic phases where *q* = N/A indicate that the refinement does not consider a modulated structure and the average structure is considered. This is not expected to have any significant impact on lattice parameters.

Data	Sample	T / K	Phase	a / Å	b / Å	c / Å	β	Cell Vol. / Å3	q	X2	wRp%	Rp%	Figure
XRD	o-LaTaO4	RT	Cmc21 (IC)	3.9279(1)	14.7749(2)	5.6217(1)	90	326.25(1)	N/A	7.19	15.56%	11.41%	**3.1**
	m-LaTaO4	RT	P21/c	7.6294(1)	5.5787(1)	7.8215(1)	101.535(1)	325.24(14)	1	1.94	8.16%	6.20%	**3.2**
		499	Cmc21 (IC)	3.9412(1)	14.7153(4)	5.6435(2)	90	327.31(2)	N/A	3.17	11.29%	8.57%	**3.12 / 3.13**
		505	Cmc21 (IC)	3.9410(1)	14.7126(3)	5.6441(1)	90	327.26(1)	N/A	2.76	9.89%	7.74%	
			Cmc21 (C)	3.9442(1)	14.6393(4)	5.6600(2)	90	326.80(1)	N/A				
		513	Cmc21 (C)	3.9441(1)	14.6404(4)	5.6594(2)	90	326.79(1)	N/A	3.40	12.16%	9.20%	
PND	o-LaTaO4	323	Cmc21 (IC)	3.9330(1)	14.8051(2)	5.6217(1)	90	327.35(1)	0.460	2.18	3.96%	3.51%	**3.7**
		483	Cmc21 (IC)	3.9427(3)	14.7365(11)	5.6450(5)	90	327.15(3)	0.456	2.57	5.60%	5.21%	**3.9**
		503	Cmc21 (IC)	3.9427(1)	14.7187(2)	5.6468(1)	90	327.71(1)	N/A	3.78	5.85%	5.02%	
			Cmc21 (C)	3.9459(1)	14.6383(2)	5.6641(1)	90	327.17(1)	N/A				
		523	Cmc21 (C)	3.9435(1)	14.6411(1)	5.6651(1)	90	327.34(1)	1	2.98	3.74%	3.30%	
	m-LaTaO4	323	P21/c	7.6329(1)	5.5821(1)	7.8258(1)	101.551(1)	326.69(1)	1	6.65	4.68%	4.35%	**3.8**

Appendix B: Pseudo-Orthorhombic Setting

In order to make fair comparisons between the changes in lattice parameters at the transition between the monoclinic and orthorhombic phases, the monoclinic parameters have been transformed into a pseudo-orthorhombic setting according to the following equations:

$$a_{\mathrm{PO}} = 0.5c_{\mathrm{m}}$$

$$b_{\mathrm{PO}} = 2a_{\mathrm{m}} * \sin\left(\frac{\pi\beta_{\mathrm{m}}}{180}\right)$$

$$c_{\mathrm{PO}} = b_{\mathrm{m}}$$

$$\beta_{\mathrm{PO}} = \frac{180}{\pi}\cos\left(\frac{2a_{\mathrm{m}}{}^{2} + b_{\mathrm{m}}{}^{2} + 0.5c_{\mathrm{m}}{}^{2}}{2b_{\mathrm{m}} * 0.5c_{\mathrm{m}}}\right)$$

Where values denoted with subscript m and PO are observed monoclinic and calculated pseudo-orthorhombic, respectively.

Appendix C: Variable Temperature PXRD Figures

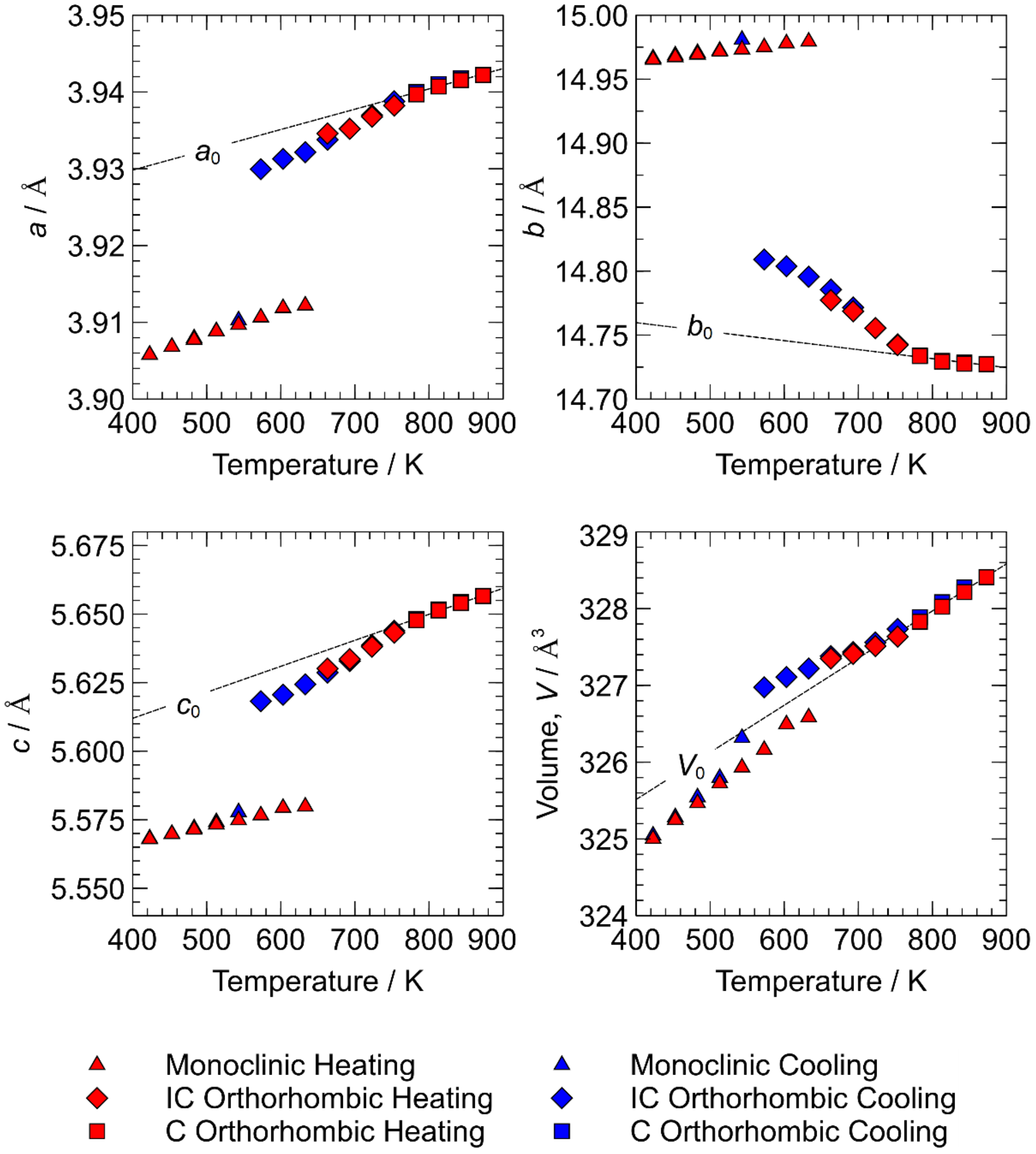

Figure C1.1: Lattice parameters of $La_{0.85}Nd_{0.15}TaO_4$ as a function of temperature. Monoclinic lattice parameters have been transformed into that of a pseudo-orthorhombic cell as in chapter 3. A line of best fit has been added to the commensurate orthorhombic parameters and extrapolated to lower temperatures for reference.

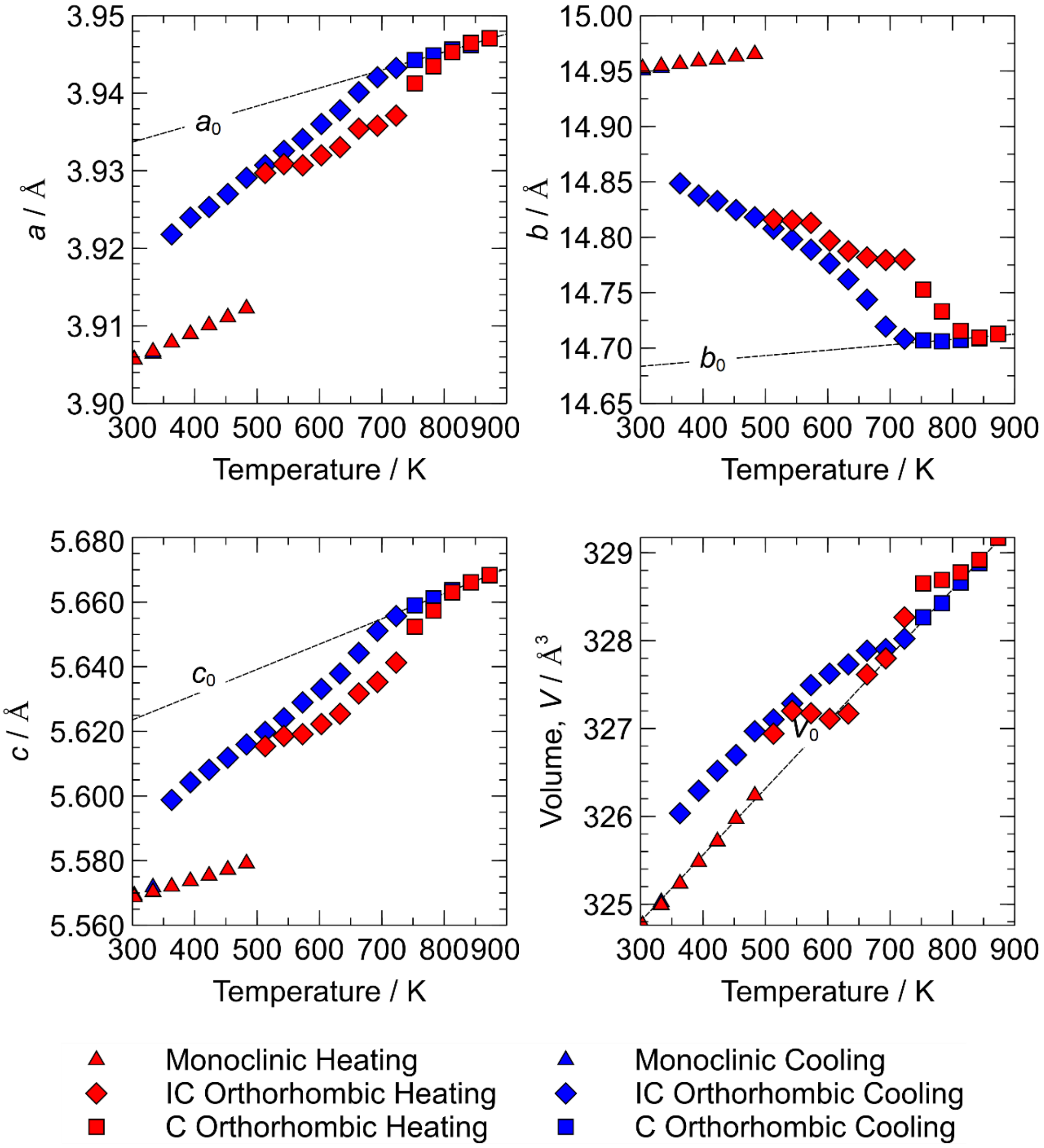

Figure C1.2: Lattice parameters of $La_{0.85}Ce_{0.15}TaO_4$ as a function of temperature. Monoclinic lattice parameters have been transformed into that of a pseudo-orthorhombic cell as in chapter 3. A line of best fit has been added to the commensurate orthorhombic parameters and extrapolated to lower temperatures for reference.